Algorithms for Continuum and Atomistic Modeling of Blood Platelet Phenomena

by

Igor V. Pivkin

Sc.M., Computer Science, Brown University, 2006
Sc.M., Applied Mathematics, Brown University, 2003
Sc.M., Mathematics, Novosibirsk State University, Russia, 1999
B.S., Mathematics, Novosibirsk State University, Russia, 1997

Thesis

Submitted in partial fulfillment of the requirements for
the Degree of Doctor of Philosophy
in the Division of Applied Mathematics at Brown University

May 2006

This dissertation by Igor V. Pivkin is accepted in its present form by
the Division of Applied Mathematics as satisfying the
dissertation requirement for the degree of
Doctor of Philosophy

Date ....
George Em Karniadakis, Director

Recommended to the Graduate Council

Date ....
Martin R. Maxey, Reader

Date ....
Aleksander S. Popel, Reader

Date ....
Peter D. Richardson, Reader

Approved by the Graduate Council

Date ....
Sheila Bonde
Dean of the Graduate School

The Vita of Igor V. Pivkin

Education

- Sc.M. (Computer Science), Brown University, 2006
- Sc.M. (Applied Mathematics), Brown University, 2003
- Sc.M. (Mathematics), Novosibirsk State University, Russia, 1999
- Sc.B. (Mathematics), Novosibirsk State University, Russia, 1997

Publications

Articles in Refereed Journals:

1. I.V. Pivkin, P.D. Richardson and G.E. Karniadakis, "Blood flow velocity effects and role of activation delay time on growth and form of platelet thrombi", Proceedings of National Academy of Sciences of the United States of America, under review, 2006.

2. I.V. Pivkin and G.E. Karniadakis, "Controlling density fluctuations in wall-bounded DPD systems", Physical Review Letters, to appear, 2006.

3. I.V. Pivkin and G.E. Karniadakis, "Coarse-graining limits in open and wall-bounded DPD systems", Journal of Chemical Physics, vol. 124, p.184101, 2006.

4. E.E. Keaveny, I.V. Pivkin, M. Maxey and G.E. Karniadakis, "A comparative study between dissipative particle dynamics and molecular dynamics for simple- and complex-geometry flows", Journal of Chemical Physics, vol. 123, p. 104107, 2005.

5. I.V. Pivkin and G.E. Karniadakis, "A new method to impose no-slip boundary conditions in dissipative particle dynamics", Journal of Computational Physics, vol. 207, pp. 114-128, 2005.

6. I.V. Pivkin, P.D. Richardson, D.H. Laidlaw, and G.E. Karniadakis, "Combined effects of pulsatile flow and dynamic curvature on wall shear stress in a coronary artery bifurcation model", Journal of Biomechanics, vol. 38, pp. 1283-1290, 2005.

7. J.S. Sobel, A.S. Forsberg, D.H. Laidlaw, R.C. Zeleznik, D.F. Keefe, I. Pivkin, G.E. Karniadakis, P. Richardson, and S. Swartz, "Particle flurries - Synoptic 3D pulsatile flow visualization", IEEE Computer Graphics and Applications, vol. 24, pp. 76-85, 2004.

Articles in Proceedings(refereed papers or extended abstracts were refereed):

1. P.D. Richardson, I.V. Pivkin, G.E. Karniadakis and D.H. Laidlaw, "Blood flow at arterial branches: complexities to resolve for the angioplasty suite", International Conference on Computer Science (3), vol. 3993, pp. 538-545, 2006.

2. I.V. Pivkin, E. Hueso, R. Weinstein, D.H. Laidlaw, S. Swartz, and G.E. Karniadakis, "Simulation and visualization of air flow around bat wings during flight", International Conference on Computer Science (2), vol. 3515, pp. 689-694, 2005.

3. I.V. Pivkin, P.D. Richardson and G.E. Karniadakis, "Simulation of mural platelet aggregation", In BMES 2004 Annual Fall Meeting, Philadelphia, PA, October 2004

4. E. Hueso, I. Pivkin, S. Swartz, D.H. Laidlaw, G. Karniadakis, and K. Breuer, "Visualization of vortices in simulated airflow around bat wings during flight", IEEE Visualization, 2004

5. I.V. Pivkin, D.H. Laidlaw, P.D. Richardson and G.E. Karniadakis, "Moving meshes and flow simulations in coronary arteries", In Proceedings of the 8th International Conference on Numerical Grid Generation in Computational Field Simulations, pp. 467-475, Honolulu, Hawaii, 2002.

6. J. Sobel, A. Forsberg, P. Richardson, D.H. Laidlaw, D. Keefe, I. Pivkin, and G. Karniadakis, "Arterial flows seen in virtual reality", In J. Vossoughi, editor, Proceedings of the 21st Southern Biomedical Engineering Conference, p. 349, 2002.

7. I. Pivkin, R.M. Kirby and G.E. Karniadakis, "High-order discontinuous galerkin methods: simulation of COIL flows", Proceedings of the Third AFOSR International Conference, Arlington, TX, August 5-9, 2001

8. G.N. Markelov, I.V. Pivkin and M.S. Ivanov, "Impulsive wedge rotation effects on the transition from regular to Mach reflection", In Proceedings of 22nd International Symposium on Shock Waves, pp. 1243-1248, London, UK, July 1999.

Conference Abstracts, Posters:

1. I.V. Pivkin and G.E. Karniadakis, "Dissipative particle dynamics simulations of colloidal suspensions", In 58th Annual APS Division of Fluid Dynamics Meeting, Chicago, IL, November 2005.

2. I.V. Pivkin and G.E. Karniadakis, "Slip and no-slip boundary conditions in DPD", In 13th International Conference on the Discrete Simulation of Fluid Dynamics Cambridge, MA, USA, August 2004

3. E.E. Keaveny, M.R. Maxey, I.V. Pivkin, G.E. Karniadakis, "A comparison of MD and DPD in simple and complex geometries", In 13th International Conference on the Discrete Simulation of Fluid Dynamics Cambridge, MA, USA, August 2004

4. S. Swartz, K. Bishop, I. Pivkin, G. Karniadakis, D.H. Laidlaw, E. Vote and D. Keefe, "3D kinematics of flying bats: challenges of complex multidimensional comparison", In Seventh International Congress on Vertebrate Morphology, Boca Raton, Florida, 2004.

5. I.V. Pivkin, N. Yang, P.D. Richardson, G.E. Karniadakis and D.H. Laidlaw, "Visualization of blood platelets in a virtual environment", In SIGGRAPH 2004 Posters

6. R. Weinstein, E. Hueso, I.V. Pivkin, S. Swartz, D.H. Laidlaw, G. Karniadakis, K. Breuer, "Simulation and visualization of flow around bat wings during flight", In SIGGRAPH 2004 Posters

7. I.V. Pivkin and G.E. Karniadakis, "Spectral element mesh generation using Gridgen for bioflows", In Gridgen User Group Meeting, 2004

8. I.V. Pivkin, P.D. Richardson and G.E. Karniadakis, "Simulation of platelets in arterioles and venules", In 56th Annual APS Division of Fluid Dynamics Meeting, Meadowlands NJ, 2003.

9. A. Forsberg, P. Richardson, J.A. Sobel, D.H. Laidlaw, D.F. Keefe, I. Pivkin and G.E. Karniadakis, "Arterial motions and flows seen in virtual reality", In Proceedings World Congress on Medical Physics and Biomedical Engineering, Sydney Australia, August 2003.

10. I.V. Pivkin, P.D. Richardson, D.H. Laidlaw and G.E. Karniadakis, "The combined effect of pulsatile inflow and unsteady geometry on flow in coronary arteries", In Proceedings of International Symposium on Modeling Of Physiological Flows, 2003.

11. I.V. Pivkin, P.D. Richardson, D.H. Laidlaw and G.E. Karniadakis, "The effect of unsteady geometry on flow in coronary arteries", In 55th Annual APS Division of Fluid Dynamics Meeting, Dallas TX, November 2002.

Abstract of "Algorithms for Continuum and Atomistic Modeling of Blood Platelet Phenomena," by Igor V. Pivkin, Ph.D., Brown University, May 2006

Mural thrombi develop under a blood flow and are predominantly composed of platelets. Thrombus growth rates are affected by the velocity of the blood flow but do not simply increase with it. They exhibit a rise and subsequent fall with blood flow velocity. While this indicates an interaction of biochemical and physical processes, previous studies only concentrate on understanding the biochemical processes. Here we show the results of simulations of thrombus formation in 3-D flows by accounting for the movements of individual platelets.

In the first part of this thesis, we study platelet aggregation in small blood vessels using the Force Coupling Method (FCM). We demonstrate that the concept of platelet activation delay time can be integrated into a computer model which incorporates a small number of physical parameters. The results of the simulations demonstrate the dependence of thrombus growth rate on blood velocity as found experimentally.

In the second part of the thesis, we turn to the Dissipative Particle Dynamics (DPD) method. We identify some of the difficulties of modeling the no-slip condition at a solid-fluid interface, and subsequently propose a new method to impose boundary conditions based on an equivalent force between wall- and DPD-particles. We then develop an adaptive model for wall-particle interactions that allows one to target desired density profiles close to the solid walls. We propose a process of choosing the DPD parameters and determining the DPD length and time scales for different levels of coarse-graining. We analyze some of the fundamental modeling ideas of DPD and identify three factors that limit the application of the DPD method at high coarse-graining levels: inter-particle force magnitude, compressibility, and geometric confinement. We conclude by applying the DPD method to the problem of platelet aggregation to test its ability to reproduce characteristic features of the aggregation process that were previously obtained by means of FCM computations.

Acknowledgments

My thesis is dedicated to my parents Nadejda Nikolaevna and Valentin Yakovlevich and to my sister Inna.

I would like to express my deepest gratitude to my advisor, Professor George Karniadakis for the knowledge, guidance and patience he provided me through my studies at Brown.

I would like to thank my co-advisors, Professor Peter Richardson and Professor David Laidlaw for their constant support and advice.

I am grateful to the members of the dissertation committee, Professor Martin Maxey, Professor Aleksander Popel and Professor Peter Richardson for their help and useful suggestions about my thesis.

My gratitude is extended to all faculty members of the Division of Applied Mathematics. I would also like to thank the staff of the Division and, particularly, Madeline Brewster.

I can not thank Olga Yoshizumi enough for her understanding and constant support. I hope that we will always be such good friends through the rest of our lives. I am very grateful to Eric Keaveny for having many interesting discussions and proof reading my dissertation. I hope that we will keep interacting and collaborating in the future. I would like to thank past and present CRUNCH group members and all my friends.

Chapter three would be impossible without help and guidance of Professor Peter Richardson. This chapter is based on the paper entitled "Blood flow velocity effects and role of activation delay time on growth and form of platelet thrombi" by I.V. Pivkin, P.D. Richardson and G.E. Karnidadakis.

It was a great pleasure to work with Eric Keaveny on the coarse-graining procedure in Dissipative Particle Dynamics method. Chapter six is based on the paper "A comparative study between dissipative particle dynamics and molecular dynamics for simple- and complex-geometry flows" by E.E. Keaveny, I.V. Pivkin, M. Maxey and G.E. Karniadakis.

This work was funded under the following grants:

- NSF ITR: CNS-0427374
- NSF CTS: CTS-0326702
- NSF ITR: EIA-0218142
- NSF ITR: CCR-0086065
- DOE: DE-FG02-99ER25372
- AFOSR: F49620-00-1-0269

Contents

List of Tables

List of Figures

Chapter 1

Introduction

Blood is composed of a liquid component, plasma, and cellular components. The cellular components are red blood cells (erythrocytes), white blood cells (leukocytes), and platelets (thrombocytes). Platelets are often considered as the smallest blood cells in the peripheral circulation. Human platelets are 2 to 4 microns in diameter with a normal concentration in blood of around 150000 to 350000 cells per cubic millimeter and a volume concentration of less than 1% [26]. The size and concentration of platelets vary significantly between different animals. Hamsters are of practical interest for experimentation, primarily because of their cheek pouch; when eviscerated and stretched out it offers facilities for visualizing microcirculation. The platelet size of (golden) hamster is $0.5 - 2\ \mu m$ in diameter, with the concentration of about 430000 platelets per mm^3 [5]. The mice platelet concentration is very high compared to the human, as the total count frequently exceeds $1000000/mm^3$, while cells are about $1\mu m$ in diameter [59].

Platelets normally present in circulating blood are in the passive state. They have no tendency to adhere to each other or vessel walls. When passive platelets interact with an injured walls or certain chemicals they become activated. The activation process consists of a sequence of physical and biological events [26]. The surface membrane acquires the ability to bind fibrinogen and the platelets become "sticky" and capable of adhering to vessel walls and other platelets. Platelets undergo a shape change to a deformable globular form with extrusion of long thin spikes called pseu-

dopodia. Chemicals, which can trigger activation of other platelets, are discharged from the platelet granules into surrounding fluid. A time interval required for a passive platelet to go through the activation process and develop its ability to adhere is called an activation delay time [57].

Platelet aggregation is important for closing the minute ruptures in small blood vessels that occur hundreds of times daily, but may also lead to arterial occlusion in the setting of atherosclerosis and trigger disease such as myocardial infarction [26]. A significant factor in controlling the rate of platelet aggregation is an interaction of the fluid flow with growing platelet thrombi. Experiments showed that the rate of growth of platelet aggregate depends markedly on blood flow velocity [5, 52]. This is an effect of the activation delay time; at higher flow rates, more of the activated platelets escape capture into the primary thrombus. At the same time, the flow is adapting to the local obstruction presented by the thrombus and makes its way around it. Due to the complex, constantly changing flow patterns and small scales involved in the process, experimental studies of platelet aggregation require careful setup. Therefore, numerical simulations taking into account the interaction between the flow and the structure formed by the thrombus may become a valuable tool in studying blood platelet phenomenon.

The standard approach to solving the equations of fluid dynamics is to compute fluid quantities on a fixed structured or unstructured mesh. For the problems involving spatial changes of fluid domain, mesh adaptivity is an essential ingredient of simulations. The adaptive algorithms often require significant programming efforts and can extend the computational time.

One alternative to these methods is the Force Coupling Method (FCM) [40, 44] in which the volume occupied by the platelets or other objects is assumed to be part of the fluid domain. The no-slip boundary condition on each cell is approximated by specifying the force in the flow at the position of the cell. Similar to standard methods, the FCM requires a computational mesh. The high efficiency of the method comes from the fact that no mesh adaptivity is required during the simulations.

Another alternative is to remove the mesh completely and represent the fluid

and solid objects as a collection of interacting points, each representing a group of atoms or molecules. This is an idea behind the Dissipative Particle Dynamics (DPD) method [15, 31]. The DPD is an inherently adaptive method and potentially very effective in simulating mesoscale hydrodynamics.

In chapter 2 the Force Coupling Method is introduced and several benchmark problems are considered. The method is applied to the problem of platelet aggregation in small blood vessels in chapter 3. Chapter 4 describes the basics of the Dissipative Particle Dynamics method. In chapter 5 we discuss the implementation of the no-slip boundary conditions in DPD. The particle based boundary conditions are proposed and evaluated. The DPD scales and units are defined in chapter 6, which is followed by the discussion of the limitations of the DPD method (chapter 7). In chapter 8 we return to the problem of boundary conditions. We develop a method for controlling density fluctuations in the vicinity of the solid objects while preserving the no-slip conditions at the interface. The modeling aspect of flows with spherical particles are discussed in chapter 9. This is followed by the simulations of platelet aggregation using DPD (chapter 10). We conclude in chapter 11 by summarizing what was accomplished in this work.

Chapter 2

Force Coupling Method (FCM)

2.1 Mathematical Formulation

In the Force Coupling Method [40, 44] the volume occupied by the particles is assumed to be part of the fluid domain. The no-slip boundary condition on each particle is approximated by specifying the force in the flow at the position of the particle. The force is added as a source term in the equation of motion,

$$\rho\frac{D\vec{u}}{Dt} = -\nabla p + \mu\nabla^2\vec{u} + \vec{F} \tag{2.1}$$

$$\nabla\vec{u} = 0, \tag{2.2}$$

$$\vec{F} = \sum_{n=1}^{N} \vec{F}^n \triangle(\vec{x} - \vec{Y}^n), \tag{2.3}$$

where the coupled force associated with the n-th particle at the first level of approximation (force monopole) is distributed around its center-point $\vec{Y}_n$ as

$$\triangle(\vec{x} - \vec{Y}^n) = (2\pi\sigma^2)^{-3/2} e^{-\frac{(\vec{x}-\vec{Y}^n)^2}{2\sigma^2}},\ \sigma = \frac{A}{\sqrt{\pi}}, \tag{2.4}$$

A being the particle radius, with the force vector

$$\vec{F}^n = \vec{F}_{\text{ext}} - \frac{4}{3}\pi A^3(\rho_p - \rho)\frac{d\vec{V}^n}{dt} + \vec{F}_{\text{contact}}. \tag{2.5}$$

The first term in equation (2.5) is an external force acting on the particles. The second term allows for the difference between the density of particles in comparison to an equivalent volume of the suspending fluid. The third term represents the force exerted between the n-th particle and other particles or solid surfaces.

The individual particle velocity is obtained from a local, volume-averaged fluid velocity as

$$\vec{V}^n = \frac{d\vec{Y}^n}{dt} = \int \vec{u} \triangle (\vec{x} - \vec{Y}^n) d\vec{x}. \tag{2.6}$$

2.2 Benchmark problems

In this section four problems of sedimentation of spherical particles between two walls in Stokes flow are considered. These problems were studied extensively by Dance [13] and are used here as a benchmark tests. In all problems the radius of the spherical particles is $A = 1$. The flow domain is a rectangular channel with dimensions $0 \leq x \leq 30$, $-5 \leq y \leq 5$, and $-15 \leq z \leq 15$. Periodic boundary conditions are used in x and z directions, while the no-slip conditions are applied on the boundaries of the domain in y direction. The fluid density, ρ, and viscosity, μ, are set to 1. In all problems, an external force $F_{\text{ext}} = 6\pi A\mu = 18.84955592$ is applied to the particles. For an isolated spherical particle settling in an unbounded domain due to external force $F_{\text{ext}} = 6\pi A\mu$, the Stokes terminal velocity is $V_s = 1$. The values of velocity components reported in this section are normalized by $V_s = 1$. The governing flow equations are solved using spectral/hp element solver NEKTAR [35]. The domain was discretized using commercially available mesh generator Gridgen from Pointwise [77]. To ensure convergence of computational results the simulations were repeated on three different non-uniform meshes with 1920, 6720 and 11520 spectral hexahedra elements with polynomial expansion order of up to 5. All meshes were refined in the regions where spherical particles were placed. The results presented below are obtained using 11520 element mesh with the third order polynomial expansion in each element.

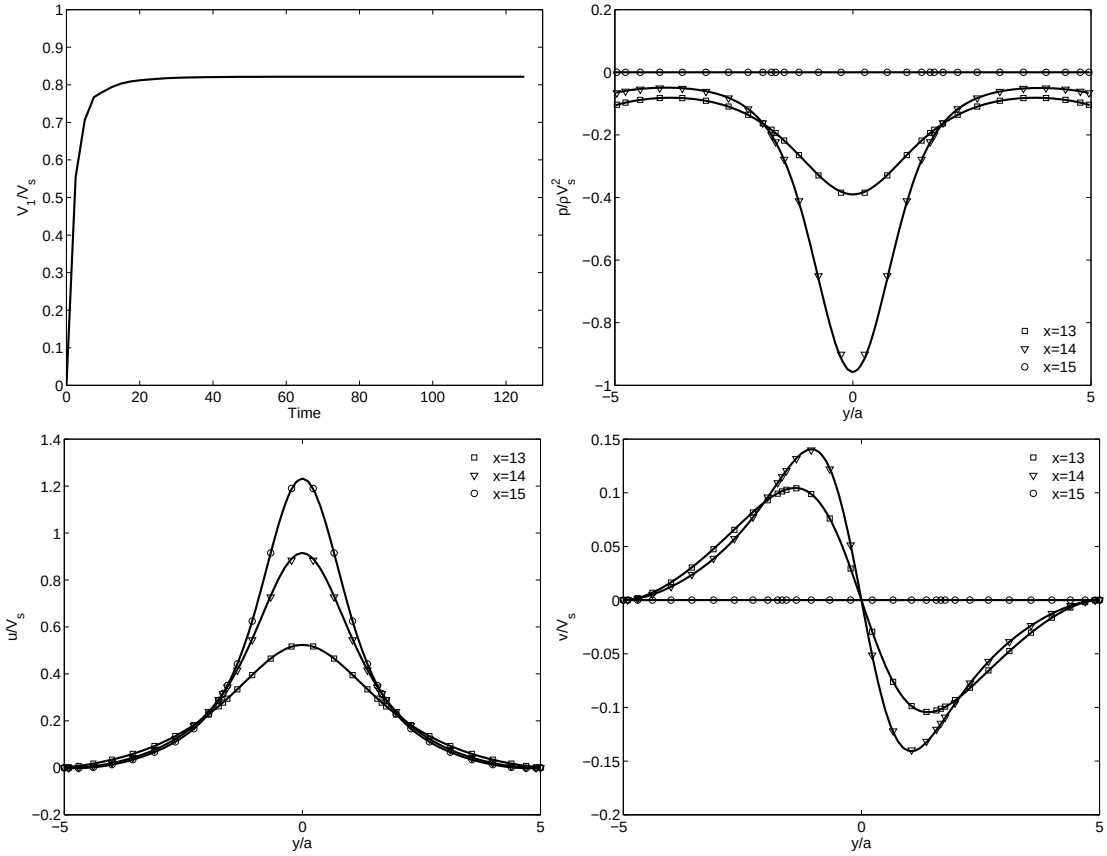

Figure 2.1: Single particle settling in the middle of two walls. (a) Variation of particle settling velocity as a function of time. (b,c,d) Pressure, streamwise and normal fluid velocity profiles extracted along the lines across the channel. Results of current study (solid lines) are plotted against results obtained by Dance [13] (symbols).

2.2.1 Single Particle Settling in the Middle of Two Walls

A single spherical particle is placed with its center at $x = 15$, $y = 0$ and $z = 0$. The external force $F_{\text{ext}} = 6\pi A\mu$ is applied to the particle in x direction. In figure 2.1(a) we plot the variation of particle velocity as a function of time. The computed terminal velocity of the particle is equal to $V_1 = 0.821500$. This is in excellent agreement with the value of 0.8214949019 reported in [13]. Next, the pressure and fluid velocity profiles are extracted along three lines inside the computational domain. The lines are located in $z = 0$ plane and are parallel to the y axis. The x coordinates of the lines are $x = 13$, $x = 14$ and $x = 15$. In figure 2.1(b)-(d) the extracted profiles are compared with those obtained by Dance [13]. The computational results are in good

agreement.

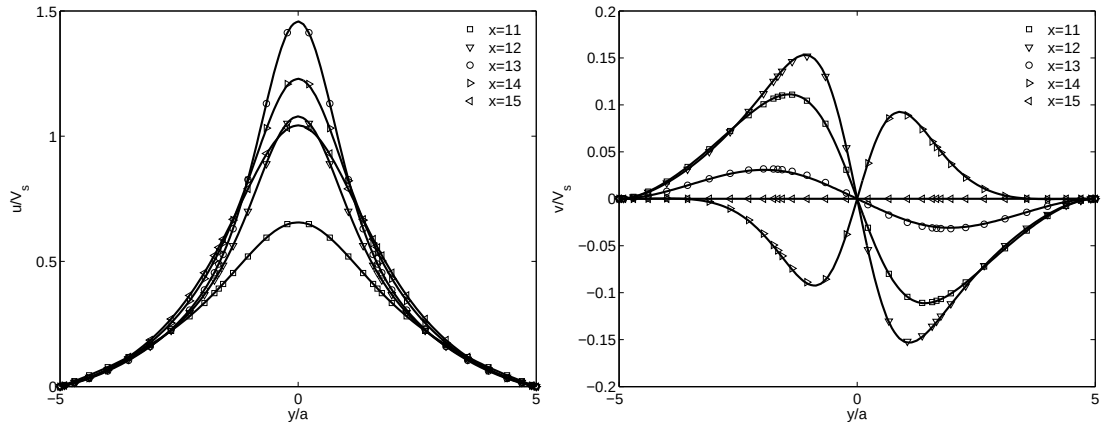

Figure 2.2: Two particles settling in the middle of two walls. Steamwise and normal velocity profiles along selected lines inside the channel. Solid lines are from current study, symbols are from [13].

2.2.2 Two Particles Settling in the Middle of Two Walls

Two spherical particles are placed inside the domain at $x = 13$, $y = 0$, $z = 0$ and $x = 17$, $y = 0$, $z = 0$. The external force $F_{\text{ext}} = 6\pi A\mu$ in x direction is applied to each particle. The computed terminal velocity of the particles is $V_1 = 1.039113$, while Dance obtained 1.039110858. Again, the velocity profiles are in good agreement, see figure 2.2.

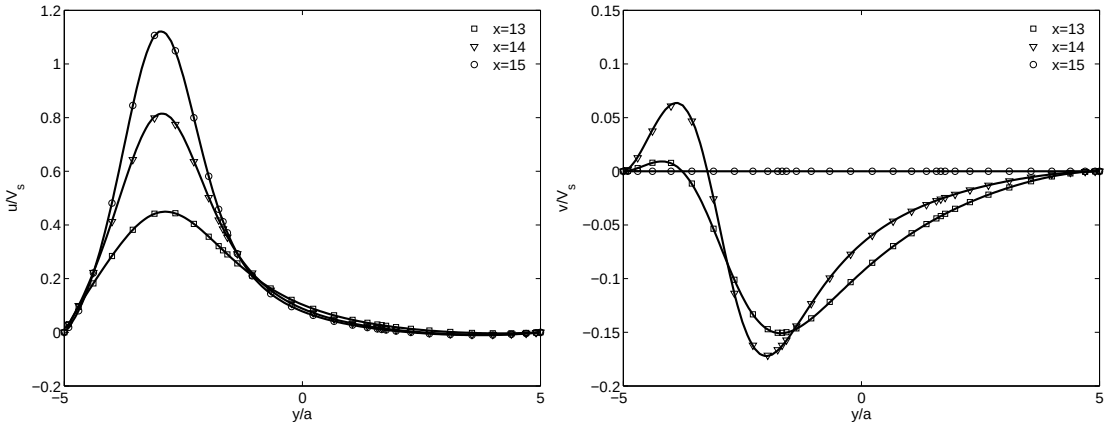

Figure 2.3: Single particle settling parallel to two walls. u and v velocity profiles (solid lines). Symbols are from Dance.

2.2.3 Single Particle Settling Parallel to Two Walls

A single particle is placed inside the domain at $x = 15$, $y = -3$ and $z = 0$. The external force $F_{\text{ext}} = 6\pi A\mu$ is applied to the particle in x direction. The particle terminal velocity is found to be $V_1 = 0.714908$; Dance reported the value of 0.714826952. Figure 2.3 shows the comparison of streamwise and normal velocity profiles inside the domain with those obtained in [13].

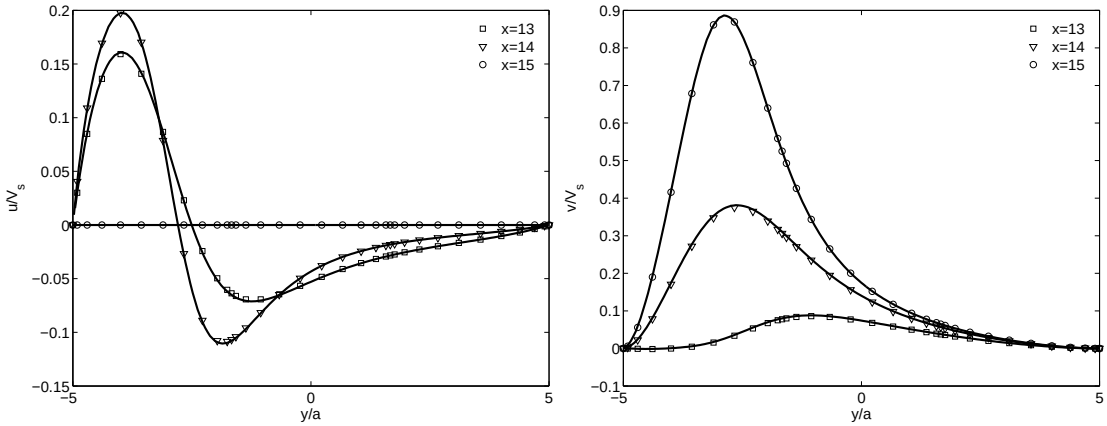

Figure 2.4: Single particle settling normal to two walls. The streamwise and normal fluid velocity profiles (solid lines) are compared to results reported by Dance (symbols).

2.2.4 Single Particle Settling Normal to Two Walls

A single particle is placed at $x = 15$, $y = -3$ and $z = 0$. The external force $F_{\text{ext}} = 6\pi A\mu$ is applied to the particle in y direction. The computed particle terminal velocity $V_1 = 0.492043$ is in good agreement with the value of 0.4906803882 reported in [13]. The streamwise and normal velocity profiles are shown in figure 2.4. The profiles agree well with results obtained by Dance.

2.3 Summary

In this chapter we considered the Force Coupling Method for Stokes flows. Four benchmark problems were studied. The simulations results were compared with re-

sults obtained by Dance [13]. In the following chapter we will consider an application of the FCM to the simulation of the platelet aggregation in small blood vessels.

Chapter 3

Simulation of Platelet Aggregation in a Small Blood Vessels using FCM

3.1 Introduction

Acute thrombogenesis in a flowing bloodstream can occur on damaged tissues in the normal circulation [5]. It has been observed also in blood flow over vascular prostheses [28] and in artificial internal organs, such as prosthetic heart valves [1]. The thrombi are composed predominantly of platelets, and they can develop even in the presence of systemic anticoagulants such as heparin [30] unless very high doses are given, for example, in extracorporeal circulation with a membrane oxygenator.

Blood flow velocity effects were investigated systematically in vivo by Begent & Born [5], who obtained quantitative data on thrombus growth rates for a range of blood flow rates. This study remains the clearest time-resolved in vivo study of the effect of blood flow rates on thrombus formation. Richardson [57] subsequently proposed that Begent & Born's observations were consistent with a shear-flow aggregation process [65, 68] in which an activation delay time of the platelets is allowed for, a delay time between each platelet's close encounter with the thrombus and its

development of ability to adhere to the thrombus, and which was estimated then to be the order of 0.1 - 0.2s. A predicted consequence of this was that the height-to-length ratio for thrombi would be lower in blood flows, where a significant fraction of the activated platelets escaped the primary thrombus before their activation delay time had elapsed; this was demonstrated later by Born & Richardson [9].

More recently, Petrishchev & Mikhailova [52] applied laser injury to mesenteric venular walls of rats and found in vivo that the mean growth rate of thrombi starting at the injury site rose with blood flow rate up to about $1mm/s$, and then fell off somewhat as the flow rate was increased in steps up to about $4.2mm/s$. Later van Gestel et al [72] returned to the mechanical injury model (puncture with a glass pipette) applied to rabbit mesenteric arterioles ($20 - 40\mu m$ diameter), but with fluorescence imaging for time-resolved platelet cytosolic free calcium response; they observed that thrombosis occurred in two contiguous parts, a tightly-packed plug in the puncture site and a trailing, looser-packed thrombus (which they called embolus, due to its frequent detachment.) Their time-resolved quantification of individual platelet response showed more than 80% of platelets adhering to either compact thrombus or looser embolus exhibited a rapid increase in cytosolic free calcium concentration that started within $0.5s$. Their figure 3 illustrates a very rapid climb in cytosolic free calcium in a majority of platelets adhering to the (future) embolus component, and they suggested that this profile was typical of platelets exposed to relatively weak agonists like ADP or thromboxane A_2. While they did not make the specific comparison, the electron micrograph of the so-called embolic portion of a thrombus in their figure 4 is very similar to the ADP-induced thrombus in figure 3 of Begent & Born. This leads to recognition that the thrombi measured by Begent & Born were of homogenous form, lacking indeed the densely-packed plug found at a vessel puncture, and overall a more attractive type of thrombus to model.

At the time of Begent & Born's studies there were two handicaps to carrying the implications further, one biological and the other computational. The biological handicap was the lack of specific knowledge of cell membrane channels and receptors, and therefore of cell mechanics by which an activation delay time could be mediated

(and varied). The computational handicap was that computing capability then available was inadequate to consider the movements of, say, $50,000$ individual platelets in a blood flow where thrombus growth is initiated at one location on a wall. This latter handicap now has diminished, and this chapter describes what is found in running simulations of the Begent & Born flow situations, and what can be predicted about thrombus formation in pulsatile flows. The latter is a circumstance important to clinical conditions such as thrombo-embolic stroke and myocardial infarction involving thrombus formation on fissured atherosclerotic plaques in carotid and coronary arteries.

3.2 Numerical Simulations

Simulations representing three-dimensional blood flow were performed for a $50\mu m$ diameter straight tube, with $500\mu m$ length at several different steady blood flow rates. Platelets are considered uniformly distributed in the inflow, with the latter having a parabolic velocity profile at entry. The mean velocity distribution alters downstream, over time, as a thrombus forms on the wall and acts as an obstacle to the flow; there is an interaction between the flow and the structure formed by the thrombus. The time-dependent computations continuously update the geometry of the thrombus with regard both to size and shape. This procedure was followed for blood flow rates both below and above the rate, which is expected to provide the maximum relative rate of growth. This provided simulation results, which can be compared with the experimental data of Begent & Born [5].

Simulations were extended to investigate the effect of pulsatility of blood flow. The inflow was prescribed to have a steady component and a simple harmonic component, the amplitude of the fluctuating component being ε times the steady component, with values of ε ranging from 0.1 to 0.7. The frequency ω of the fluctuating component was $1Hz$. The product of the activation delay time τ and the frequency ω is a dimensionless parameter. Both might be modified pharmacologically and largely independently, so behaviour of thrombus growth at other values of the product are

prospectively interesting, to determine if there are zones of behaviour worth targeting, and whether there are reasons for possible differences in thrombus growth between small animal (higher ω) and large animal (lower ω) observations, while τ differs less between the relevant species.

3.3 Biological Model

In the experiments of Begent & Born, thrombus formation was initiated and sustained by iontophoretic delivery of ADP from the tip of a fine hollow needle placed in the connective tissue layer outside the blood vessel and in which the blood vessel is supported. With this mode of supply, one can expect that there is a period of time in which the concentration of ADP builds up parallel to the axis of the blood vessel, and therefore the axial location at which the ADP concentration due to the iontophoresis is large enough to initiate activation of platelets advances upstream for a while. The footprint of ADP concentration around the outside of the vessels Begent & Born used was likely to have an elliptic form progressively "wrapping around" the side of the vessel close to the iontophoresis needle tip, and changing in its axial- and circumferential-direction spans for some time. In the experiments, the size of this footprint likely increased progressively with time.

In the simulation approach, it has been important to explore a selection of rules applied for every platelet regarding the inter-platelet and platelet-wall interactions. Thrombi, except those plugging a vessel wall puncture, have a degree of loose-packing compared with, say, sedimentary behaviour of solid grains packing with solid-surface contact. Fibrinogen and fibrin strands have a part of this, and were recognized early as essential co-factors in aggregation; platelet "stickiness" develops when the platelet membrane acquires the ability to bind fibrinogen [78].

Falati et al [17] used confocal and wide field microscopy to image thrombus formation with platelets, fibrin and tissue factor in real time, using mice cremaster arterioles. Vessel wall injury was induced by a pulsed nitrogen dye laser (non-puncture injury). Platelets were visible in attachment by 4 seconds after injury. Polanowska-

Grabowska and Gear [53] had previously shown that platelets can adhere very rapidly to collagen exposed on a surface. Falati et al [17] found co-localization of the platelets and the fibrin in the thrombus, although the fibrin had a lag time of incorporation of about 15 seconds. Tissue factor was localized on the upstream edge of the thrombus and along the vessel-wall interface. Falati et al [17] did not provide an electron micrograph of any thrombi. Falati et al [18] later provided additional information on tissue factor accumulation in developing thrombi. Plasma fibronectin is also known to have a role in thrombus growth and stability [48].

Activation of platelets initiated by ADP can occur at a finite distance of separation from a growing thrombus for platelets approaching it, because of diffusion of ADP from the thrombus (or, in the Begent & Born experiment, also from the extravascular iontophoretic source.) These aspects of platelet interaction invoke use of two length scales. Another issue for incorporation in an interaction model is that of a repulsive force function in the event of close-approach. Energy landscapes have been described for single molecular bonds [16], which can be studied under ingeniously designed and carefully controlled laboratory conditions that assure single bonds only are involved. Thrombi develop in vivo with multiple bonds, and so a more generalized form of energy landscape is applied for the calculations reported here. The links used in the model here incorporate the effects of many individual bonds.

One extra choice available is that for the adhesive footprint of the thrombus on the wall to which it attaches: given a seeded location (where a few platelets are adherent, a computational-model replacement of the use of iontophoretic application of ADP to initiate thrombosis), should any activated platelet be allowed to attach anywhere it comes sufficiently close to the wall surface downstream? Or should a geometrically-defined patch on the wall limit the extent where that may happen? Our simulations reported here cover these two. Other adhesion site rules could apply, such as that adherable sites may occur randomly distributed spatially over a surface, with mutual distances typical of the sites found as platelet-prepared sites by in vitro experiments for blood flow over non-biological substrates that have been coated with specific proteins, such as collagen, fibrinogen or fibronectin [6]. Such a range of choice

of footprint rules for the computation may be needed to represent adequately typical different causes of thrombus formation, such as highly-localized vascular injury, or fissures at atherosclerotic plaque caps, or flow over manufactured surfaces as in needles or over artificial-organ components. Even within one footprint type, there can be an effect of the relative locations of the small number of seed platelets present at the beginning, and this too has been explored somewhat.

3.4 Mathematical Model

For our simulation, we assumed platelets in concentration of $300,000$ per mm^3, $3\mu m$ equivalent diameter, a vessel diameter of $50\mu m$, parabolic velocity profile at the inlet and mean blood flow velocities of $100 - 800\mu m/s$, overlapping the major range of Begent & Born's experimental conditions. Applying the Force Coupling Method [44] the system is described by equations (2.1)-(2.6), where the non-linear term in momentum equation is neglected (Stokes flow).

The contact force term $\vec{F}_{\text{contact}}$ in equation (2.5) includes, for any platelet, a repulsive portion when the platelet is approaching and has come within a specific distance of another platelet or wall surface. If both the n-th platelet and another (or the location on the wall) it encounters are in the active state the link is created between them. No more than one link can be created between each pair of activated platelets (or the activated platelet and the wall). For activated platelets with links in addition to the repulsive force, there is also an attractive force, shown at the larger distances of separation; this is zero at smaller, finite distances to permit loose packing of mutually adhering platelets. The looseness of packing is significant for a thrombus because it provides a space through which the suspending fluid can seep. It also recognizes the linking role of fibrinogen without attempting to model it in detail. We note that Guy and Fogelson [25] have made computational estimations regarding the role of fibrinogen, based on the collision of two spherical particles with fibrinogen available in the suspending fluid, one particle being already activated, and consider bond completion and bond rupture; because of the many platelets considered in our

model, a simpler form of relation which does not assess aspects of fibrinogen concentration is used here. In our model (see figure 3.1), each platelet carries with it an activation-distance corona. Before a platelet is triggered it is tested at each step in time to determine whether an activated platelet has its centre within twice the activation-distance corona of its own centre; if so, the platelet is coded as having its activation triggered, and within a time span (freshly) randomly chosen between two time interval limits it becomes activated. (These are larger than the time-step used in the flow computations.) The finite extent of the activating corona beyond the perimeter of the platelet allows in this model for diffusion of activators such as ADP without attempting a more exact determination of the convective field involved. If an activated platelet has not adhered within a finite recovery time it returns to its initial passive state. Throughout these conditional aspects the model is intended to make practical allowances for physico-physiological aspects in ways that avoid requirement of concurrent solutions for e.g. time-dependent ADP transport to be generated as these would considerably increase the already long computation times. Much detailed biochemistry is condensed, and only the associated major changes in physical forces are modelled here. The model is chosen to allow computations to march forward in time, without iteration. Each time a computation is performed with constant values of parameters and the same flow rate, there is some variation from the results of otherwise similar runs when the random-number generator for determining individual platelet activation delay times is freshly seeded. Thus, replication runs are made to explore the corresponding variability of thrombus growth.

The governing flow equations are solved using the spectral/hp element solver NEKTAR [35] marching forward in time steps, the position vectors for all the platelets being updated (and all associated near-neighbour conditions being checked) for each time step. The Force Coupling Method seems more reliable when the average particle density is modest, and so the suspension of red cells is treated as a continuum. The few other cells typical of whole blood such as the leukocytes are omitted from the model as being too low in number-density to have a significant dynamic effect.

At the beginning of the computation, the fluid in the vessel is empty of platelets

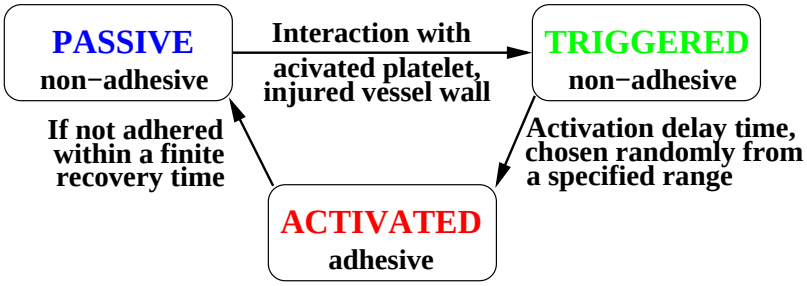

Figure 3.1: In our model, platelets can be in three different biological states: passive, triggered and activated. In passive state, platelets are not adhesive; this is a normal state of the platelets in blood. If a passive platelet interacts with an injured wall or an activated platelet it becomes triggered and after an activation delay time it becomes activated and adhesive. The activation delay time is chosen uniformly at random from a specified range. If after a finite recovery time an activated platelet does not adhere to anything it returns back to a passive state.

but the entering flow has them approximately uniformly distributed in it. However, by the time there are platelets sufficiently close to the seed platelets on the vessel wall to be activated, there is full priming of the flow at smaller radii with platelet-laden blood. To initiate thrombus growth at a known location, typically three activated platelets were placed close together on the vessel wall at the initiation of flow. (In pulsatile flows of large amplitude, these were observed to oscillate somewhat back and forth in the flow direction, a natural consequence of the model and sometimes seen in actual flows.) Approaching platelets, which come close enough to these become triggered; while a few triggered platelets escape downstream, many become activated while still close enough to adhere, and through continuous repetition of this process the platelets aggregate as a mural thrombus. Representing the platelet radius as A, values that need to be chosen to run computations are the activation-distance corona $R_A A$, with $R_A \geq 1$; the outer limit of the repulsion radius $R_R A$, with $R_R \geq 1$; and the minimum distance of the longer-range attraction $R_L A$, with $R_L \geq R_R$. From that point, the attraction force increases with increasing distance linearly to a maximum at $R_M A$ ($R_M > R_L$), following which it diminishes to zero at $R_B A$ ($R_B > R_M$), and remains zero for all greater distances. Other parameters, which need to be prescribed, include the repulsive force relation, the long-range attraction relation (the maximum tensile load carried per cell-cell bond is likely to affect embolization), and the activation

delay time. The latter is assumed randomly uniformly distributed over the range t_{a1} to t_{a2}, with $t_{a2} \geq t_{a1}$, selected for each platelet once, but differently in otherwise replicate runs.

In our computations the repulsive force acting on the platelet approaching the wall was

$$\vec{F}_1^n = \alpha_1 \frac{R_R A - d}{R_R A} H\left(R_R A - d\right) \vec{n}, \tag{3.1}$$

$H(x)$ is the Heaviside function, d is a distance from the centre of the platelet to the wall, and $\vec{n}$ is a unit normal to the wall pointing into the domain. When platelets overlapped, a repulsive force was added,

$$\vec{F}_2^n = -\alpha_2 \frac{2R_R A - d_{mn}}{2R_R A} H\left(2R_R A - d_{mn}\right) \frac{\vec{d}_{mn}}{d_{mn}}, \tag{3.2}$$

where $\vec{d}_{mn} = \vec{Y}^m - \vec{Y}^n$ is a vector connecting the centres of platelets m and n, and $d_{mn} = \left|\left|\vec{d}_{mn}\right|\right|$. The constants α_1 and α_2 were set to $8 \times 10^{-9} N$. The attraction force between the activated platelet and the location $\vec{x}_w$ at the wall was

$$\vec{F}_3^n = \alpha_3 \frac{d_w - R_L A}{R_L A} H\left(d_w - R_L A\right) \frac{\vec{d}_w}{d_w}, \tag{3.3}$$

where $\vec{d}_w = \vec{x}_w - \vec{Y}^n$ and $d_w = \left|\left|\vec{d}_w\right|\right|$. For a pair of an activated platelets we had

$$\vec{F}_4^n = \begin{cases} 0 & \text{if} \quad d_{mn} \leq R_L A, \\ \alpha_4 \frac{d_{mn} - R_L A}{R_L A} \frac{\vec{d}_{mn}}{d_{mn}} & \text{if} \quad R_L A \leq d_{mn} \leq R_M A, \\ \alpha_4 \frac{R_M - R_L}{R_L} \frac{R_B A - d_{mn}}{R_B A - R_M A} \frac{\vec{d}_{mn}}{d_{mn}} & \text{if} \quad R_M A \leq d_{mn} \leq R_B A, \\ 0 & \text{if} \quad d_{mn} > R_B A. \end{cases} \tag{3.4}$$

The constants α_3 and α_4 were equal to $4 \times 10^{-9} N$. The values of R_R, R_L, R_M and R_B were set to 1, 1.5, 2.5 and 3.5, respectively. The extent of the activation-distance corona was defined by $R_A = 1.5$. The range of activation delay time was specified by $t_{a1} = 0.1s$ and $t_{a2} = 0.3s$. The platelet recovery time was set to $5s$.

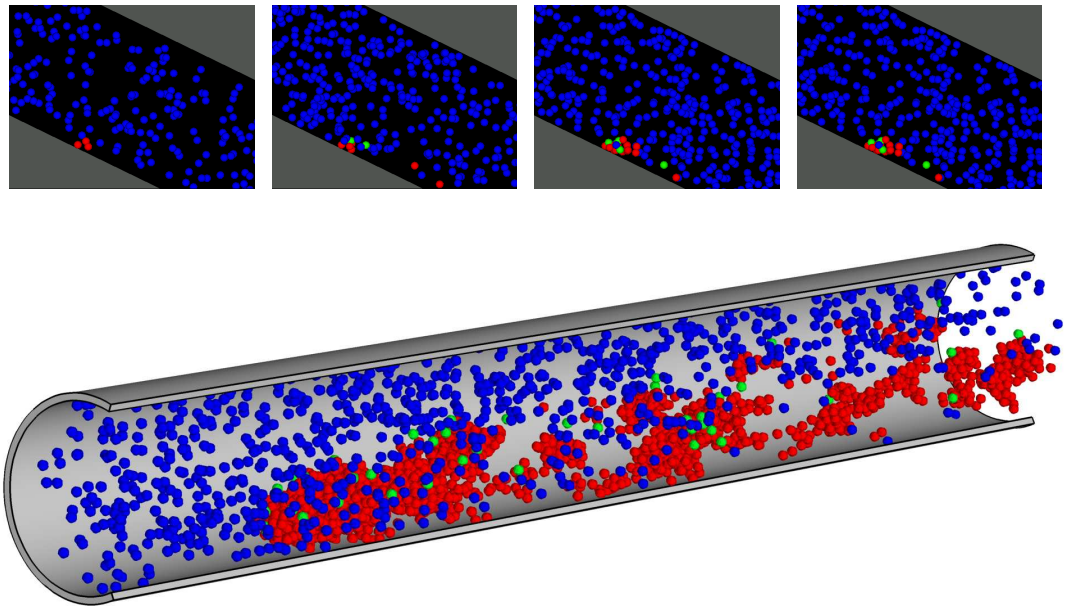

Figure 3.2: (a) Thrombus growing on a blood vessel wall; blue - inactivated platelets, green - triggered platelets, converting after a characteristic time delay to activated - red. (b) Late stage in a similar computation, where adhesion of activated platelets is allowed at all locations downstream.

3.5 Results

Steady Inflow Results: (1) The simulation predicts thrombi growth with shapes and patterns similar to those observed experimentally. Figure 3.2(a) shows a sequence of frames from a simulation of such a thrombus growth. There is an early, brief (up to about 3 seconds) phase of rapid growth, which would not have been detected in Begent & Born's experiments because of the difficulty of seeing distinctly a mural grouping of so few platelets, followed by a slower yet exponential rate of growth.

(2) Thrombi initiated under the same flow conditions may have a varied small-growth time, but have major growth at an exponential rate which has no set relation to variation in the small-growth time; and embolization of part of a thrombus can readily resolved in the computation even for thrombi as small as 10 platelets.

The number of platelets accumulated in a thrombus for replicate computing runs at one flow velocity is shown in figure 3.3(a). The lines correlating each run in the exponential-growth phase have closely similar slopes, and the time taken to that phase

from the initiation of flow varies somewhat. This result is similar to that reported by Begent & Born, except that they had no way for observing the variation of the short initial phase because the number of platelets adhering to the wall then was too small, being below the resolving power of their microscope, nor did they run a number of replicate runs at each flow rate to determine statistics of the variability of the growth-rate factor as a function of blood flow rate. The slope of the exponential growth for the model was calculated as a mean and standard variation from the replicate runs.

(3) The model used provides for flow-structure interaction, as illustrated in figure 3.3(b). This figure displays, in 3-D at one instant in time, some flow lines computed at locations lying closely over a thrombus in an early stage of its growth. The streamlines - of which a small number are displayed - have clearly adapted to the local obstruction to flow presented by the thrombus, and make their way around it. This continues as more and more platelets aggregate into the thrombus.

(4) Thrombi initiated at other flow rates also have their major phase of growth exponential in time, and the growth-rate coefficient has a maximum as a function of flow rate. We note that the growth-rate coefficient, which can be deduced from using a natural-logarithm scale for the vertical axis in the right-hand graph in figure 7 of Ref. [5], does not fall within the range of those listed in figure 5 of the same paper but is somewhat below the lowest value in that figure 5, and we surmise there is a scaling-factor error in the vertical axis of the latter but we lack the original data to be able to determine that definitively.

Investigation of thrombus growth was repeated for a number of different flow rates in the vessel. Qualitatively similar results were obtained. Values of the slope of the exponential growth are shown as a function of the vessel flow rate in figure 3.4(a). Broadly similar to Begent & Born, it was found the exponential growth rate initially rose with flow rate, but there was a peak and for higher blood flow rates the growth rate fell. This is an effect of the activation delay time; at higher flow rates, more of the activated platelets escape capture into the primary thrombus. Some runs were computed at a flow rate above $500 \mu m/s$ with zero activation time to check this and to verify that lower growth rates were not simply due to accumulation of effects of

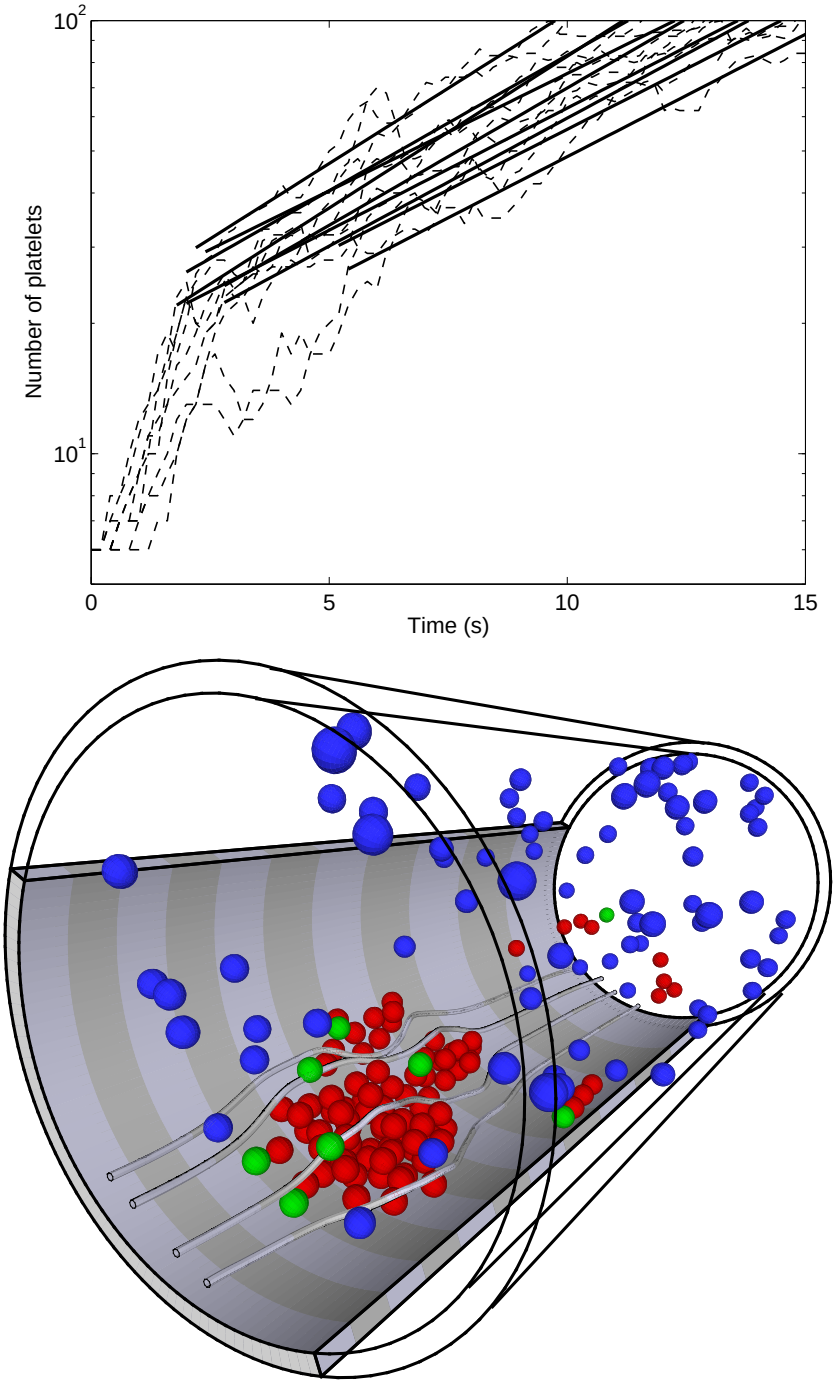

Figure 3.3: (a) Accumulation of platelets in a thrombus, conditions of figure 3.2(b,c) with flow rate of $100\mu m/s$. Solid lines used to correlate exponential growth phase; slopes plotted on figure 3.4(a). (b) Flow structure interaction illustrated by flow(stream) lines close to developing thrombus, flow going from left front to right rear, perspective view. For clarity most inactivated platelets omitted.

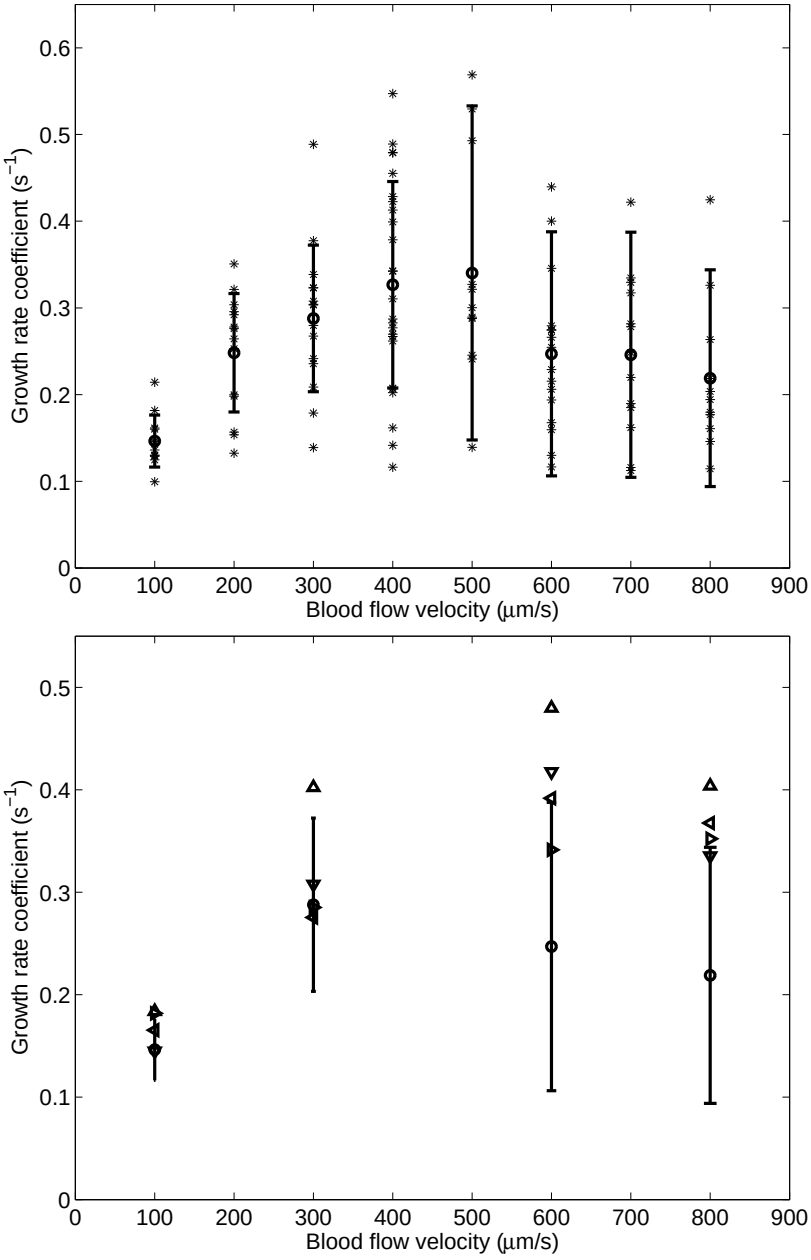

Figure 3.4: (a) Exponential thrombus growth rate coefficients as a function of flow rate in small vessel $50\mu m$ diameter; mean values shown as circles, individual values from replicate computer simulations shown with asterisks, the trend of the mean growth rate coefficients as a function of flow rate matching qualitatively the rend from Begent & Born. (b), For four flow rates, the effect of sinusoidal flow pulsations (mean of replicate computer simulations) shown for various relative amplitudes ε of pulsation compared with steady-flow means ($\circ$) and standard deviations (vertical bars). $\triangle$ is for $\varepsilon = 0.1$, $\triangleright$ is for $\varepsilon = 0.3$, $\triangledown$ is for $\varepsilon = 0.5$, $\triangleleft$ is for $\varepsilon = 0.7$.

repeated embolization of portions of the growing thrombus. If the wall downstream is readily adhesive to activated platelets, one typically sees a secondary thrombus develop there (see figure 3.2(b)). Indeed, after some growth, secondary thrombi can grow with a higher capture effectiveness there than at the leading thrombus.

(5) Porosity of thrombus is significant to good capture efficiency of approaching platelets.

The sensitivity of the results to the assumed values for various parameters was investigated. When the minimum distance of the longer-range attraction was halved (making a more compact thrombus), the thrombus growth rate was stunted, with more platelets being deflected in the flow over the thrombus than being caught by it. (This possibility was anticipated in figure 1 in Ref. [9], and is borne out by the simulations.) It appears that the opportunity for enough plasma to filter through the thrombus is significant in maintaining a high platelet capture efficiency.

However, when the minimum distance of the longer-ranged attractive force is increased far enough, e.g. for a 50% increase of that distance at a flow rate of $300\mu m/s$, the steady flow may (according to some computational results) push the thrombus into more of a "carpet" form lying close to the wall at early growth times, because the equivalent mutual tether length is too long to require the linked platelets to form a pile; and the carpet may not require many platelets that have become added to it to adhere also to the wall to hold the thrombus until embolization.

(6) The number and mutual positioning of "seed" platelets have an effect on the small-time growth period.

While it might seem optimum in some sense to use just one adherent platelet as the initial seed, this extends considerably the computing time required to reach a thrombus of N platelets, $N \gg 1$, because with basically exponential growth it takes as the same order of time interval to go from 1 to 2 platelets as it does to go from 100 to 200 in a thrombus, so starting with more than one fixed "seed" platelet to initiate a thrombus saves considerable computing time. However, there is then an effect from the spacing and configuration of the seed set of platelets. If one seed platelet was close enough to streamlines that had passed over a proximal seed platelet the early

capture rate seemed higher.

(7) The limitation of thrombus surface-attachment opportunity in the downstream direction, when applied as a boundary condition in our computations - with a fixed location of the downstream boundary - leads to thrombi which can overhang the distal end of the attachment zone, but the part of the thrombus that overhangs distally has compliant behaviour and can be flattened in contact with the wall or can peel up. When in the up-position, the growth rate of the thrombus slows considerably. However, after some time in the up-position it can make a relatively rapid transition to the down-position again and the thrombus resumes a growth rate typical of a thrombus without a raised tailpiece.

(8) For a given blood flow rate, there is a range of net thrombus growth rates that likely contribute to the variability of observed "bleeding times" – these times running until leakage at a standard cut (skin) or through a puncture (tube) effectively stops. For flow rates above $400\mu m/min$, running a dozen or so computations with replicate initial conditions gave an even larger variation in time taken to reach the larger thrombi sizes, likely to be needed to achieve thrombotic occlusion of a distal vessel puncture, over the range of two-to-one or more found at lower flow rates. Figure 3.5 illustrates these times for thrombi of 70 platelets.

The effect of pulsatility was investigated by imposing a sinusoidal variation of velocity to the inflow,

$$\vec{u}_{\text{inflow}} = \vec{u}_{\text{mean}}(1 + \varepsilon \sin(\omega t)), \tag{3.5}$$

with ε being the amplitude of pulsatility relative to the mean flow. The period of oscillation was 1 second. A shorter period was not considered, to keep the pulsatility period distinct from the activation delay time. Thrombus formation was computed for a range of values of mean flow, and with $\varepsilon = 0.1$, 0.3, 0.5 and 0.7. Again, exponential growth was observed, and for this flow geometry the mean values of the exponentional coefficients (five replications for each set of conditions) lies within the 95% error range of the results for purely steady flow except for $\varepsilon = 0.1$, for which the growth rates were

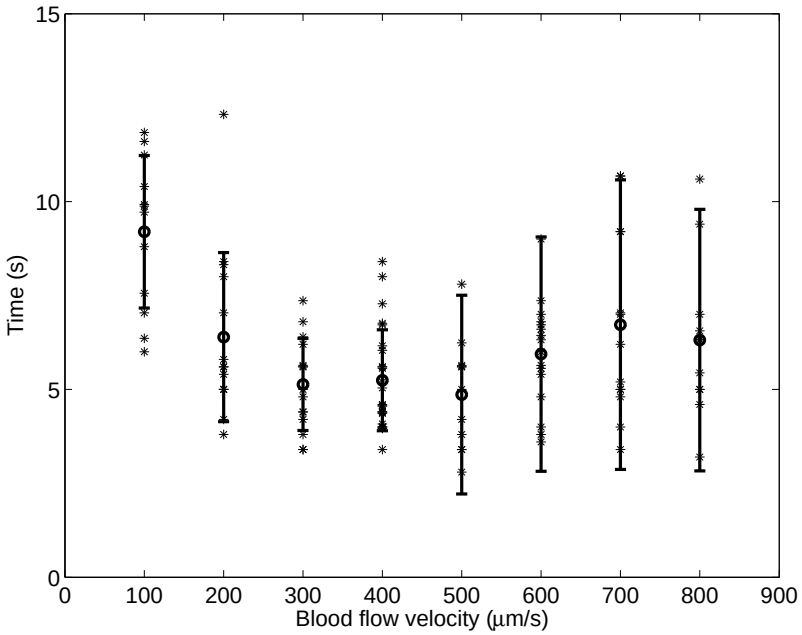

Figure 3.5: Ranges of bleeding time (as assessed by time to form a thrombus of 70 platelets) as a function of the blood flow velocity in the tube. At all velocities the range is at least a factor of 2.

higher. Upon examining the time-resolved thrombus size in detail, it was seen that with large-enough ε it appears possible that a small embolus can be peeled away from the thrombus cyclically in a way not found with steady flow or with $\varepsilon = 0.1$, and thus the cumulations with time at the higher ε have a noticeable saw-tooth appearance, with the temporarily higher thrombus growth rate partly offset in the mean due to the loss of the emboli.

Thus, to first order in a straight flow geometry and with conditions precluding recirculation, the effect of sinusoidal pulsations at a typical human heart rate is to cause thrombi to develop at a rate closely related to that for steady flow at the corresponding mean flow conditions, and highest relative to that at $\varepsilon = 0.1$.

3.6 Discussion

It must be noted that the thrombus-formation modelling described here was for an initially uniform flow passage with parallel streamlines. Here we demonstrate that

the concept of platelet activation delay time can be integrated into a computer model of mural thrombus formation, which accounts for motions of all platelets individually involved, and which incorporates a small number of physical parameters and functions to represent physico-chemical factors such as cell adhesion molecule behaviour, fibrinogen, and so forth for the scale represented in the model. It may be discovered in vivo that the activation delay time is affected by the vascular location in which thrombi grow, and by the ability of the endothelium to produce NO and other agents. There may be some effect of vascular location on the energy landscape relevant to adhesion and aggregation that typically occurs there; the observation of Poole et al [54] that in a large vessel, such as the aorta, platelets tend to form monolayers on damaged areas of the wall without aggregating into mural thrombi may reflect that the typical inter-platelet linkage distance is greater there so that a flat form of thrombus occurs. Obviously there are difficulties in obtaining measurements of inter-platelet distances in thrombi, especially in vivo, but some effort on this to distinguish possible variations depending on vascular location and blood velocity would be worthwhile for improving details of the model for application in such circumstances. The later phenomenon of clot retraction implies the prior existence of non-zero distances between the platelets that comprise it, and which possess contractile components in the cytoskeleton, and no attempt is made here to model that.

Reviews have frequently updated listing of pro- and anti-thrombotic factors, with details of their actions and interactions, such as by Jackson et al [33] and Oude Egbrink et al [50]. Although effects of blood flow rate on platelet adhesion and aggregation, and on thrombus growth, have been known for decades, in many experimental studies the flow conditions are not recorded or controlled for, nor are electron micrographs of thrombi routinely reported. Such incompleteness of experimental information makes it difficult to improve representational details applied in computer modeling. It has been noted that in use of light-dye methods for thrombus initiation the vessel-wall injury varies with the intensity of the light applied, $120 J/cm^2$ leading to macromolecular leakage and platelet activation but a dose six times as strong caused endothelial and smooth muscle cell swelling and ruptures, gap formation and

leukocyte accumulation [46]; reports of light intensity used, and of the extent of primary vascular injury, are often missing. There are, of course, some representational details used in the model that may be robust, in the sense that modifications of values of some parameters may make modifications of outcome that are too small to distinguish by presently-available methodology in experiments (the standard deviations in the thrombus growth rates as a function of blood velocity measured by Petrishchev & Mikhailova are comparable with variations that arise in our computational model, but also imply that such experiments may be limited for comparing with small refinements of the model.) For example, in modeling the interplatelet attractive forces it seems sufficient for the present to use one fixed force-distance relation for a fixed finite time, although in practice it must vary over time (likely connected in part to the variations of platelet cytosolic free calcium with time [72]) and be associated with a mix of engaged cell-surface receptors and composition of linking molecules. In modeling platelet-platelet repulsive forces, modifications to the platelet membrane stiffness (as by alpha-tocopherol) may require a corresponding adjustment, but potentially also to the attractive force because alpha-tocoperol also down-regulates GPIIb promoter activity [10]. If a negative feedback regulation associated with platelet-borne MMP-9 [64] is confirmed to play a role, it could be necessary to include its effect in the activation aspects of the model used here. If there are sub-populations with different reactivies, as implied by van Gestel et al [72], this too can be incorporated by adaptation of the model.

In a study to assess thromboembolism associated with pulsatile flow, Sukavaneshvar et al [66] observed in an ex vivo model that flow pulsatility induced increases in both thrombosis and embolism.

The model may lead to improvements in assessing the impact of various platelet-active drugs, observed and measured in specific flow conditions, in altering thrombus formation in a variety of other flow conditions. Hopefully, our model will spur new experiments to determine some of the parameters of thrombi previously overlooked, and lead to models more sophisticated in representation of biochemical and physical processes that matter most.

Chapter 4

Dissipative Particle Dynamics (DPD)

4.1 Introduction

Despite the teraflop speeds of current parallel computer systems, molecular modeling of liquid-state systems based on atomistic simulations is still computationally prohibitive for mesoscopic spatial domains and integration times. To this end, many interesting new methods have been proposed in the last few years focusing on coarse-graining approaches that yield low-dimensional systems amenable to fast computations in simulation studies of simple and even complex, e.g. biomolecular, liquid systems. Typical coarse-graining approaches include the elimination of fast degrees of freedom, clustering of individual atoms into larger single-interaction particles, and spatio-temporal averaging of effective interaction potentials [32]. Other recent coarse-graining approaches based on stochastic closures or approximate inertial manifold ideas that could potentially be used for liquid-state systems can be found in [36] and [67], respectively.

Dissipative particle dynamics (DPD) [31] is a coarse-graining method that employs both simplified potentials – that can be thought of as averaged effective potentials [20] – as well as grouping of atoms into a single particle, i.e., the DPD particle. The method describes interacting clusters of molecules moving together in a Lagrangian

fashion subject to soft repulsive-only potentials. Specifically, for simple fluids there are three types of forces acting on each dissipative particle:

- A purely repulsive conservative force,
- A dissipative force that reduces velocity differences between the particles, and
- A stochastic force directed along the line connecting the center of the particles.

The computational advantage of DPD compared to MD for mesoscopic systems stems from the use of soft potentials as well as the clustering of N_m atoms into a large DPD particle. Experience with DPD simulations and scaling arguments, see [23], shows that the combined computational speed-up, say for water simulation, is about $1000 \times N_m^{5/3}$, which for $N_m = 5$ and 10 gives the large factors of $73,000$ and $464,000$, respectively. Clearly, such accelerated simulations allow for laptop-based mesoscopic simulations of complex biomolecular systems where water is the main component.

4.2 Mathematical Formulation

Let us consider a system consisted of N particles having equal mass (for simplicity in the presentation) M, positions $\vec{r}_i$, and velocities $\vec{v}_i$. The aforementioned three types of forces exerted on a particle i by particle j are given by

$$\vec{F}_{ij}^C = F^C(r_{ij})\hat{r}_{ij}, \tag{4.1}$$

$$\vec{F}_{ij}^D = -\gamma w^D(r_{ij})(\hat{r}_{ij} \cdot \vec{v}_{ij})\hat{r}_{ij}, \tag{4.2}$$

$$\vec{F}_{ij}^R = \sigma_R w^R(r_{ij})\theta_{ij}\hat{r}_{ij}, \tag{4.3}$$

where $\vec{r}_{ij} = \vec{r}_i - \vec{r}_j$, $r_{ij} = |\vec{r}_{ij}|$, $\hat{r}_{ij} = \vec{r}_{ij}/r_{ij}$ and $\vec{v}_{ij} = \vec{v}_i - \vec{v}_j$. The variables γ and σ_R determine the strength of the dissipative and random forces, respectively. Also, ξ_{ij} are symmetric Gaussian random variables with zero mean and unit variance, and are

independent for different pairs of particles and at different times; $\xi_{ij} = \xi_{ji}$ is enforced in order to satisfy momentum conservation. Finally, ω^D and ω^R are weight functions.

All forces are acting within a sphere of interaction radius R_c, which is the length scale of the system. The conservative force is given by a soft potential (see [24]):

$$\vec{F}_{ij}^C = \begin{cases} a(1 - r_{ij}/R_c)\hat{r}_{ij}, & r_{ij} < R_c \\ 0 & r_{ij} \geq R_c \end{cases}, \tag{4.4}$$

$a_{ij} = \sqrt{a_i a_j}$, where a_i and a_j are conservative force coefficients for particle i and particle j. The requirement of canonical distribution sets two conditions on the weight functions and the amplitudes of the dissipative and random forces, see [15]. Specifically, we have that

$$\omega^D(r_{ij}) = \left[\omega^R(r_{ij})\right]^2, \tag{4.5}$$

and

$$\sigma^2 = 2\gamma k_B T, \tag{4.6}$$

where T is the system temperature and k_B the Boltzmann constant. The weight function takes the form

$$\omega^R(r_{ij}) = \begin{cases} 1 - r_{ij}/R_c & \text{for } r_{ij} \leq R_c, \\ 0 & \text{for } r_{ij} > R_c. \end{cases}$$

The time evolution of DPD particles is described by Newton's law

$$d\vec{r}_i = \vec{v}_i dt, \tag{4.7}$$

$$d\vec{v}_i = \frac{1}{M}\left(\vec{F}_i^C dt + \vec{F}_i^D dt + \vec{F}_i^R \sqrt{dt}\right). \tag{4.8}$$

Here $\vec{F}_i^C = \sum_{i \neq j} \vec{F}_{ij}^C$ is the total conservative force acting on particle i; $\vec{F}_i^D$ and $\vec{F}_i^R$ are defined similarly.

Chapter 5

Particle Boundary Conditions in DPD

Dissipative particle dynamics (DPD) is a potentially very effective approach in simulating mesoscale hydrodynamics. However, because of the soft potentials employed, the simple no-slip boundary conditions are difficult to impose. In this chapter, we first identify some of these difficulties and subsequently we propose a new method, based on an equivalent force between wall- and DPD-particles, to impose boundary conditions. We demonstrate the validity of this approach for steady problems (Poiseuille flow, lid-driven cavity) as well as for the unsteady oscillating flow over a flat plate.

5.1 Introduction

One of the main issues for DPD simulations in confined geometries is the imposition of boundary conditions, specifically at solid boundaries. To this end, the boundary conditions that have been used in DPD are based on general ideas implemented both in lattice Boltzmann method (LBM) and molecular dynamics (MD) formulations. However, unlike the MD method, the soft repulsion between DPD particles cannot prevent fluid particles from penetrating solid boundaries, and thus extra effort is required to impose accurately the no-slip (or partial slip) wall boundary condition. To the best of our knowledge, although good progress has been made, there is no yet

consensus as to what type of boundary conditions performs best, especially in the presence of conservative forces as well as in complex-geometry flows.

A broad classification of the three main approaches to impose boundary conditions in DPD was provided in [55] as follows:

1. The Lees-Edwards method described further in section 5.2 to impose planar shear, also used in LBM [74], which is essentially a way to avoid modeling directly the physical boundary [7, 8, 38]. The periodic Poiseuille flow method [3] considered later in chapter 7 also falls into this category.

2. Freezing regions of the fluid to create a rigid wall or a rigid body, e.g. in particulate flows, see [8, 31].

3. Combine different types of particle-layers with proper reflections, namely specular reflection, bounce-back reflection, or Maxwellian reflection [19, 56, 76].

The third category is indeed quite broad, and the technical details in the various implementations published so far are quite different. Since the method proposed in this chapter also employs particle-layers as well as reflections, we review in some more detail the most representative works published so far that fall under category (3).

In [56] a particle-layer is stuck on the solid boundary and effective dissipative and random forces are obtained analytically on the DPD fluid particles by assuming a continuum limit. However, reflections were found necessary to reflect particles back into the fluid when they cross the wall since the effective computed forces are not sufficient to prevent wall penetration. In [55] the effect of specular, Maxwellian and bounce-back reflections was also investigated. In specular reflections the velocity component tangential to the wall does not change while the normal component is reversed. In the bounce-back reflection both components are reversed. A Maxwellian reflection involves particles that are introduced back into the flow with a velocity following a Maxwellian distribution centered around the wall velocity. In [55], a key non-dimensional parameter was identified that affects the wall slip velocity. Specifically, there are five governing parameters in the DPD fluid system: M (the mass of

particles); γ (the friction coefficient); R_c (the cut-off radius); k_BT (temperature); and $\lambda_d = \rho^{-1/d}$ (the average distance between particles, where d is the space dimension and ρ is the number density). We can define the dimensionless friction coefficient

$$\tilde{\gamma} \equiv \frac{\gamma\lambda}{dv_T}$$

where $v_T = \sqrt{k_BT/M}$ is the thermal velocity scale. Large values of $\tilde{\gamma}$ mean that the particles move very little in the time scale associated with the velocity decaying due to thermal fluctuations. In [55] the plane Couette flow was considered in order to evaluate the above boundary conditions. The Lees-Edwards boundary conditions work well for this model but the objective is to see what type of reflections are appropriate with their particle-layer approach. It was shown in [55] that for large values of $\tilde{\gamma}$ all three reflections result in a no-slip condition. However, for small values of $\tilde{\gamma}$, the specular and Maxwellian reflections produce an excessive slip velocity at the wall while the bounce-back approach still satisfies the no-slip condition. An anomaly, however, was observed in the temperature profile very close to the wall at small values of $\tilde{\gamma}$ even with the bounce-back boundary conditions. Another problem with the approach of [55] is that the computation of forces is analytic and cannot be easily extended to non-planar walls. In addition, the more difficult case where conservative forces are present was not considered. As we shall see below, this is an important case as it induces large density fluctuations at the wall.

In [76] an extra particle-layer is included outside of the domain with the objective of constructing a correct velocity profile that continues *beyond* the wall boundary. The position and velocities of particles inside that layer are determined from the layer of DPD particles adjacent to the boundary and within a distance R_c (the interaction radius). For example, to impose zero velocity at a solid boundary, points in the particle-layer outside the domain have tangential and normal velocity components opposite from the original. When a DPD particle hits the boundary, a bounce-back reflection is imposed. This approach works very well in the absence of conservative forces but when conservative forces are present density oscillations occur. In this case,

a second layer of DPD particles was introduced by [76] between R_c and $2R_c$ in order to compute the repulsive interaction. This approach seems to reduce but not totally eliminate the density fluctuations at the walls. Overall, the method of [76] is quite effective but it may not be easily implemented in complex-geometry flows, e.g. flow around a cube, as it is not clear how to construct such "ghost" particle-layers in such situations.

Finally, in the third category above we have also included another implementation reported in [19]. In this implementation, frozen particles are used to represent the wall but there is an extra thin layer of DPD particles inside the domain and adjacent to the solid boundary where the no-slip boundary condition holds. Specifically, a random velocity distribution with zero mean is enforced in this layer with corresponding particle velocity

$$\vec{v}_i = \vec{v}_R + \vec{n}(\sqrt{(\vec{n}\cdot\vec{v}_R)^2} - \vec{n}\cdot\vec{v}_R),$$

where $\vec{v}_R$ is the random vector and $\vec{n}$ is the unit vector towards the flow domain. The thickness of the layer in channel flows is selected as the minimum of 0.5% of the channel width and $R_c/2$; this thin layer is necessary to prevent the frozen wall cooling down the DPD fluid. Nevertheless, some temperature drop at the wall boundaries is present in the simulation results reported in [19], which is undesirable.

The objective of this chapter is to produce a systematic way of imposing the no-slip boundary condition. The method we propose is under the general category (3) of the aforementioned list and can be easily implemented for simple- and complex-geometry flows. The main idea is to provide a systematic procedure to compute the repulsion force exerted by the wall particles on the fluid in combination with bounce-back reflections, across a wide range of densities for liquids. The new method is verified for Poiseuille flow, Stokes flow over an oscillating plate, and for the lid-driven cavity, using both analytical solutions and corresponding high-order accurate Navier-Stokes solutions.

5.2 Lees-Edwards Boundary Conditions

We will use the Lees-Edwards method later in the text, so here we provide its brief description. Consider a system of particles in a periodic box and assume that the upper wall is moving with velocity $U_x/2$ and lower wall with $-U_x/2$. Lees and Edwards [38] suggested a method to simulate this shear flow by applying modified periodic boundary conditions. A particle crossing the upper boundary of the box at time t is re-introduced through the lower boundary with its x-coordinate shifted by $-U_x t$ and the x-velocity decreased by U_x. For a particle crossing the lower boundary of the box the x-coordinate shift is $U_x t$ and the x-velocity is increased by U_x. In addition, in computing the force between particle i interacting with particle j through the upper (lower) boundary, $-U_x$ ($+U_x$) should be added to the relative velocity $\vec{v}_{ij}$.

5.3 Diagnostic DPD Simulations

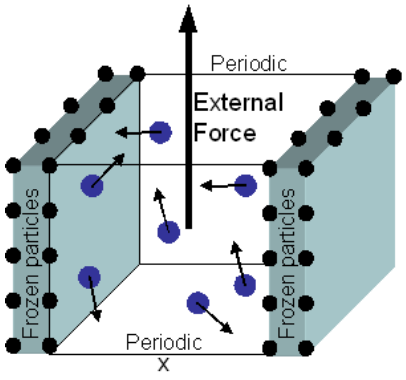

Figure 5.1: Sketch of the cubic domain for simulating Poiseuille flow. Periodic boundary conditions are imposed in two directions. The walls are simulated by freezing DPD particles.

In order to appreciate the degree of difficulty in imposing no-slip boundary conditions with the DPD method as well as to identify the most influential parameters, we first perform some diagnostic DPD simulations for Poiseuille flow in a channel. The flow domain is a cube with size 10, and periodic boundary conditions are imposed

along two directions, see figure 5.1. In order to sustain the flow, an external body force equal to 0.02 (DPD units) is imposed. The density of the DPD fluid is $\rho_f = 3$ and the temperature is $k_B T = 1$. The random and dissipative forces are defined by the parameters $\sigma_R = 3$ and $\gamma = 4.5$, respectively, while the conservative force parameter is set to $a_f = 25$. We simulate the solid walls by freezing the DPD particles in the wall regions. The wall particles interact with fluid particles, however we do not allow them to move. In some cases we will also use bounce-back boundary conditions. In order to investigate the effect of the wall density, we will use different values for the number density of the walls, ρ_w. In addition, we will vary the conservative (also called repulsive) force coefficient for the wall particles, a_w. The results we will present below are obtained by subdividing the domain into 100 bins across the channel, while the simulations were run for 200,000 time steps and the results were averaged over the last 40,000 time steps.

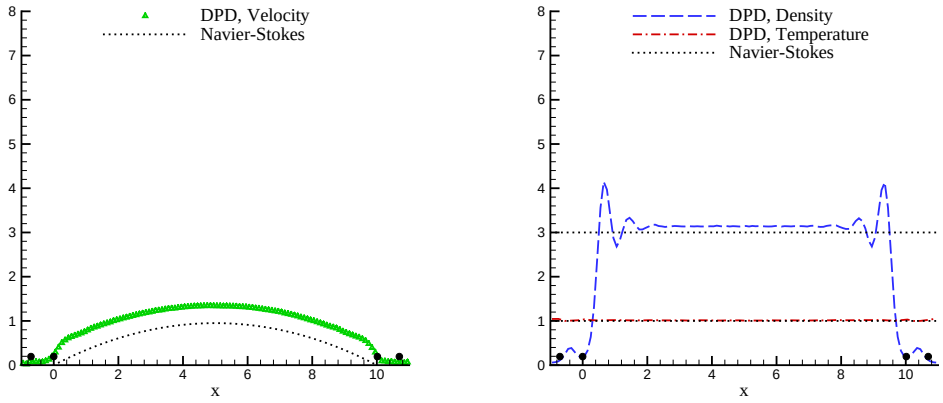

Figure 5.2: Left: Velocity profile. Right: Density and temperature profiles. The walls are simulated by freezing DPD particles. ($\rho_w = \rho_f; a_w = a_f$).

First, we simulate the case with the walls modeled by freezing the DPD particles in two layers inside each wall region. The walls have the same density as the fluid, i.e. $\rho_w = \rho_f$, and the conservative force of the wall DPD particles, a_w, is the same as of the fluid particles, a_f. The results of the simulations are shown in figure 5.2. The dashed line is density, the dash-dotted line is partial temperature along the periodic

cross-flow direction and triangles is the velocity profile across the channel. The dotted lines are the Navier-Stokes solutions corresponding to no-slip boundary conditions. The main finding here is that the fluid particles can penetrate wall regions, as it can be seen from the non-zero density of the fluid particles inside the walls. This is the result of the soft repulsive forces employed in the DPD formulation. In order to prevent the fluid particle from penetrating the walls we can increase the wall density or the repulsion (conservative) force of the wall particles.

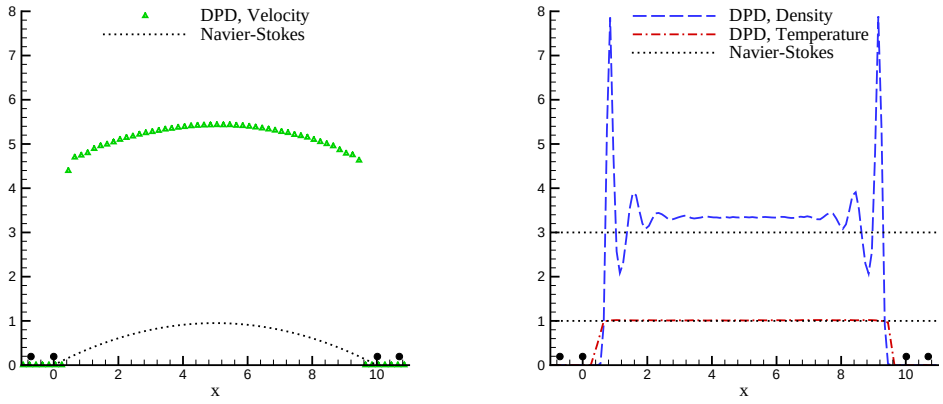

Figure 5.3: Left: Velocity profile. Right: Density and temperature profiles. ($\rho_w = 4\rho_f; a_w = a_f$). The walls are simulated by freezing DPD particles.

Next we increase the wall density to be four times higher than fluid density. The results from these DPD simulations are shown in figure 5.3. There is no fluid penetration into the wall regions, however, large density fluctuations appear across the channel. The density level of the fluid in the middle of the channel is elevated and there are almost no particles close to the walls. The fluid is squeezed towards the middle of the channel by the wall particles leading to a large velocity slip.

If we increase the repulsion force of the wall particles, keeping the wall density the same as fluid density, we obtain similar results as before as shown in figure 5.4. Again, density fluctuations and large slip are observed. From these results we conclude, that to prevent fluid particles from penetrating the walls increasing the wall density of wall particles or the repulsion force may not be an effective solution.

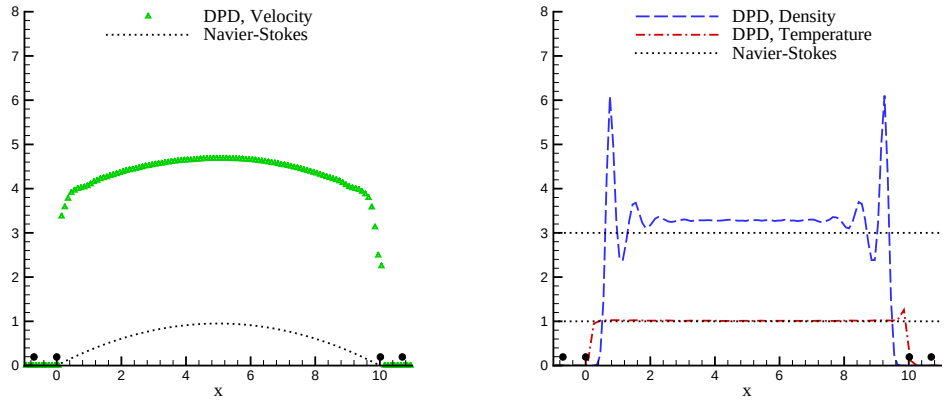

Figure 5.4: Left: Velocity profile. Right: Density and temperature profiles. ($\rho_w = \rho_f; a_w = 4a_f$). The walls are simulated by freezing DPD particles.

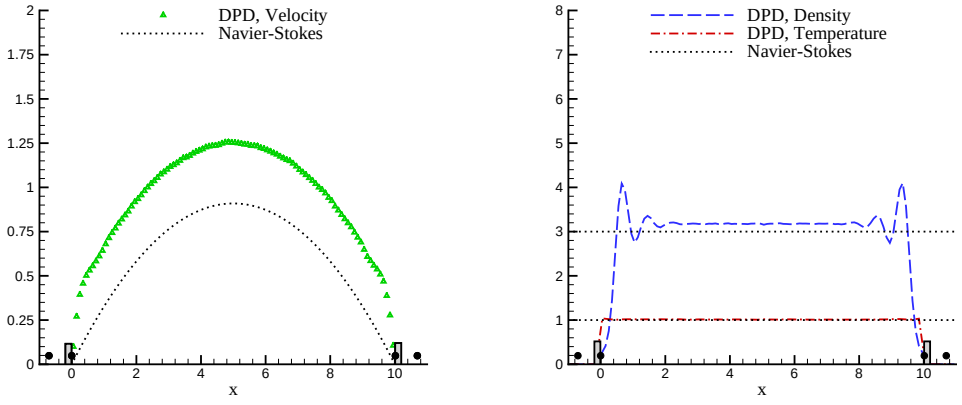

Figure 5.5: Left: Velocity profile. Right: Density and temperature profiles. ($\rho_w = \rho_f; a_w = a_f$). The walls are simulated by freezing DPD particles in combination with bounce-back boundary conditions (shown as shaded rectangles).

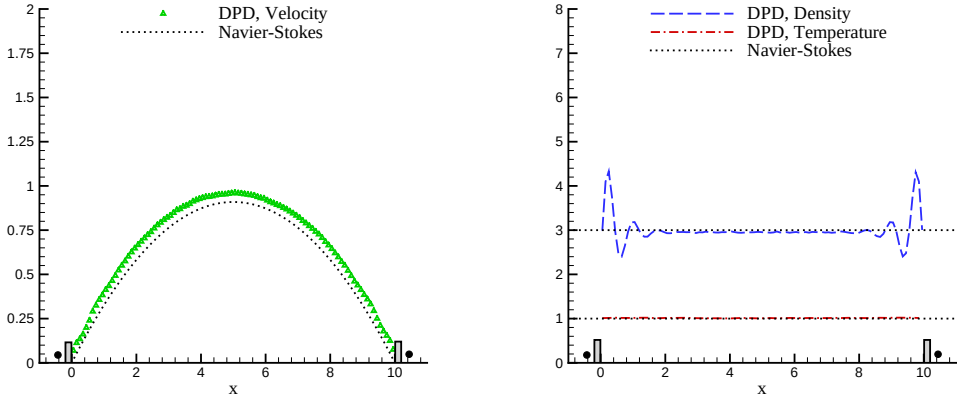

Figure 5.6: Left: Velocity profile. Right: Density and temperature profiles. ($\rho_w = \rho_f; a_w = a_f$). The walls are simulated by freezing DPD particles in combination with bounce-back boundary conditions. The wall particles are shifted by half inter-particle distance.

We now return to the first test case above and employ the bounce-back boundary condition on the surface of the walls, keeping the density and the conservative force of the wall particles the same as of fluid particles. From the results shown in figure 5.5, we can see that the fluid density is low close to the wall. This is due to the excessive repulsion of fluid particles away from the walls. One way to fix this problem is to shift the wall particles away from the fluid-solid interface. The question is how to choose the shift distance? A straightforward approach is to shift the wall particles by half inter-particle distance, which is $\frac{1}{2}\rho_f^{-1/3}$. The results from such simulations are shown in figure 5.6. The density fluctuations are less pronounced than in previous cases while the level of the density in the middle of the channel is close to the desired level. The velocity profile has improved, although some slip is still present. When we fix the density profile by shifting wall particles, we also reduce the dissipative force (or friction) between the fluid particles and the walls; the latter depends on the distance between particles. Bounce-back boundary conditions compensate for this effect, however, this correction may not always be sufficient and may lead to some small slip, as we can see from the results of figure 5.6.

5.4 Particle Boundary Conditions

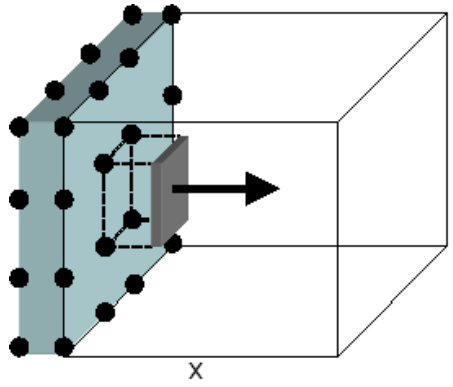

Figure 5.7: Sketch of an imaginary plane on which we compute the force exerted by the wall particles.

In this section we propose a procedure to apply no-slip boundary conditions building on what we presented in the previous section. Let us consider the wall, which is created by freezing layers of DPD particles, see figure 5.7. The particles are distributed on a regular lattice with distance $\rho_w^{-1/3}$. We know the structure of the wall and the conservative force, so we can calculate the force exerted by the wall particles. Specifically, to compute the average force per unit area due to wall particles we used $30 \times 30 = 900$ points. They were uniformly distributed over a square patch with size $\rho_w^{-1/3}$ that was placed within a specified distance from the wall. The average force was taken to be the arithmetic average of the force at these 900 points. The plot of this force per unit area against the distance from the wall is shown in figure 5.8.

We note here that this force is proportional to the effective wall-fluid particle conservative force parameter, $a_e = \sqrt{a_w a_f}$. Next, we compute the total force per unit area exerted by the wall particles for different values of the wall density; the total force is the area under the curve in figure 5.8. Subsequently, we fit a second-order polynomial using the computed values to obtain an analytic approximation for the total force in the range of densities from $\rho_w = 3$ to 25, and the results are shown in figure 5.9. We have set the coefficient a_e to 1.0 in these computations. The

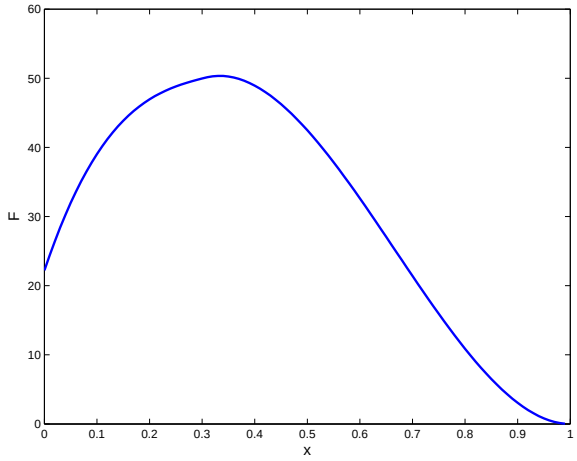

Figure 5.8: Force exerted by wall particles per unit area against the distance from the wall.

approximation we obtained for the total force is

$$F_w = a_e(0.0303\rho_w^2 + 0.5617\rho_w - 0.8536), \tag{5.1}$$

where ρ_w is the wall density. This approximation is valid only for wall density ρ_w variations between 3 and 25. For other values of the wall density or different wall structure (e.g., fcc lattice) we can employ a similar procedure to obtain the total force F_w.

We now consider the fluid in the cubic domain and ignore for the moment the presence of the walls. If we place an imaginary plane on the surface of the simulation domain the force exerted by fluid per unit area in this plane will be equal to the pressure of the fluid, which can be estimated by the expression, see [24],

$$P = \rho_f k_B T + 0.1 a_f \rho_f^2. \tag{5.2}$$

If we move this imaginary plane away from the wall, the force decreases and at one cut-off distance R_c from the wall it is zero. Our objective now is to adjust the wall particle repulsion force coefficient, a_w – and as a result the effective conservative force coefficient, a_e – in such a way, that if we place a particle within one cut-off distance

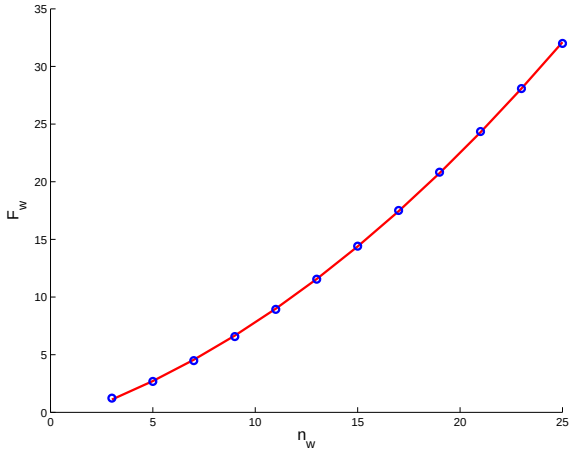

Figure 5.9: Computed total force from the wall - circles; second-order polynomial fit - solid line. The effective repulsive force coefficient a_e is set to 1.0 here.

from the wall, the average force acting from the wall will be equal to the force from the fluid. We can parameterize the total force per unit area from the fluid as $\alpha_w P$. A value of α_w that gives good results in simulations for DPD fluid densities considered in this chapter is 0.39. Specifically, for $\alpha_w = 0.39$, the computed fluid density level in the middle of the channel is within 1% from desired value. For fluid densities not considered in this chapter, α_w may be adjusted appropriately.

In summary, the final result is that we can estimate the value of the conservative force coefficient of wall particles from

$$a_w = \frac{a_e^2}{a_f}, \tag{5.3}$$

where

$$a_e = \frac{0.39(\rho_f k_B T + 0.1 a_f \rho_f^2)}{(0.0303\rho_w^2 + 0.5617\rho_w - 0.8536)}. \tag{5.4}$$

In the following, we will present several prototype flow examples in order to evaluate the proposed boundary conditions.

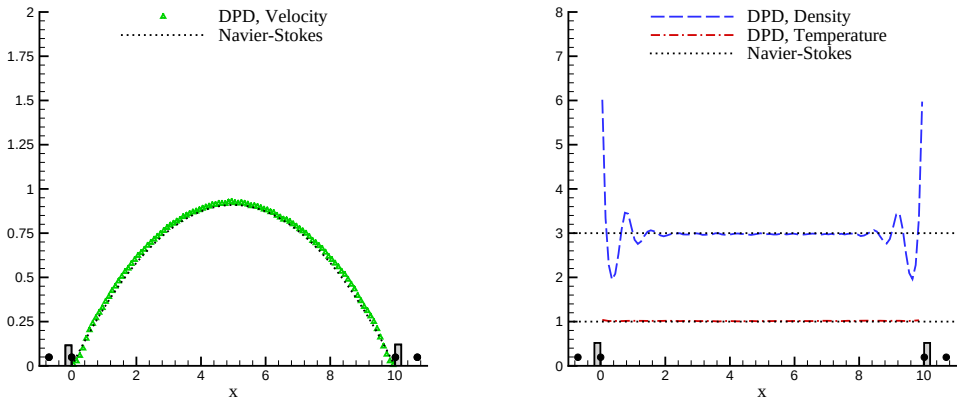

Figure 5.10: Left: Velocity profile. Right: Density and temperature profiles. The walls are simulated by freezing DPD particles in combination with bounce-back boundary conditions. The conservative force of the wall particles is computed as described in the text. ($\rho_w = \rho_f = 3; a_w = 3.2447$).

5.4.1 Poiseuille flow

The first test case is Poiseuille flow, as in the previous section, with the density of the fluid and the wall density equal to 3. We use bounce-back boundary conditions on the surface of the wall. The conservative force of the wall particles is adjusted as described above, see equation (5.3), and it is equal to $a_w = 3.2447$. As we can see in figure 5.10, we have some residual density variations at the ends of the channel, however in the middle of the channel the density has the desired level. In addition, we satisfy the no-slip conditions. Similar cases for density equal to 6 and 9 are shown in figure 5.11 and figure 5.12, where the wall particle conservative force coefficients are equal to 2.4320 and 2.4111, respectively.

We have also verified the DPD code by repeating case A (Poiseuille flow of simple DPD fluid) considered in [19]. The simulation parameters are the same as in the original paper except the implementation of no-slip boundary conditions. We use two layers of freezed DPD particles inside each wall region, in combination with bounce-back reflection. The conservative force coefficient for wall particles is computed as described above and is equal to 2.6588. The results of simulations are in a very good

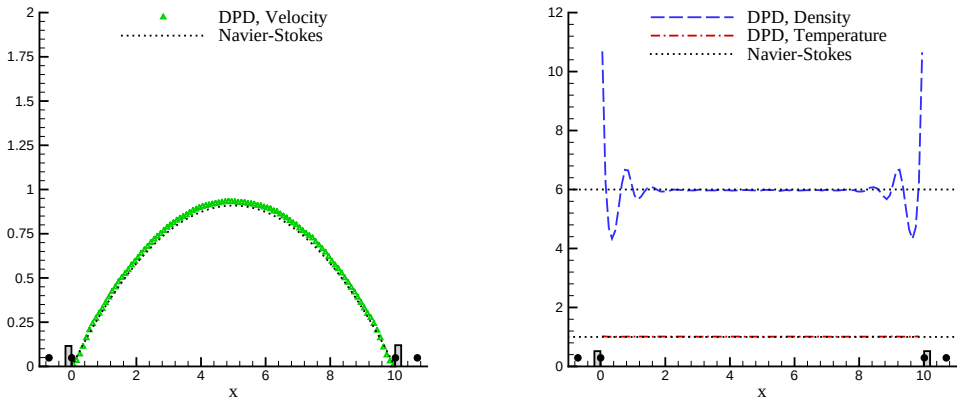

Figure 5.11: Poiseuille flow. Left: Velocity profile. Right: Density and temperature profiles. The walls are simulated by freezing DPD particles in combination with bounce-back boundary conditions. The conservative force of the wall particles is computed as described in the text. ($\rho_w = \rho_f = 6; a_w = 2.4320$).

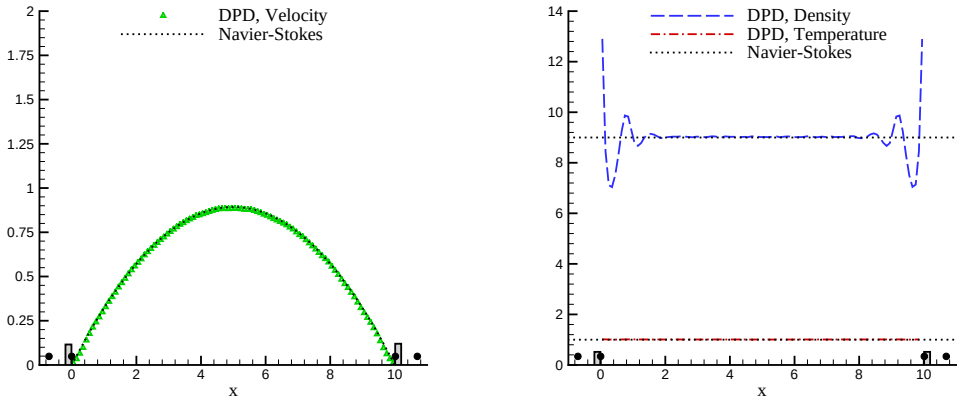

Figure 5.12: Poiseuille flow. Left: Velocity profile. Right: Density and temperature profiles. The walls are simulated by freezing DPD particles in combination with bounce-back boundary conditions. The conservative force of the wall particles is computed as described in the text. ($\rho_w = \rho_f = 9; a_w = 2.4111$).

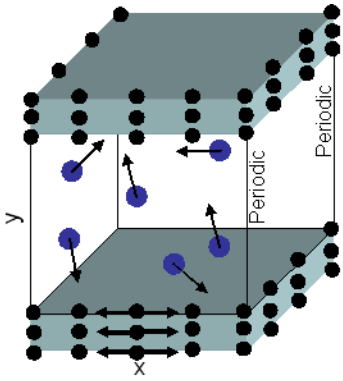

Figure 5.13: Stokes oscillating plate problem. The fluid domain is a cube, periodic in two directions. The walls are simulated by freezing DPD particles, in combination with bounce-back boundary conditions. The lower wall is oscillating.

agreement with [19]. In particular, the computed fluid velocity in the middle of the channel is 8.633 in comparison to the value 8.639 predicted in [19].

5.4.2 Unsteady Stokes flow

Next we consider an unsteady case, namely Stokes flow over an oscillating flat plate, for which an analytic solution exists, see [51]. The fluid domain is a cube with size 10, while periodicity is imposed along two directions, see figure 5.13. The lower wall is oscillating with velocity $U_x = \sin(\Omega_x t)$, where $\Omega_x = \pi/20$. The density of the DPD fluid is $\rho_f = 10$, and the temperature is set to $k_B T = 1/3$. The random and dissipative force coefficients, σ_R and γ, are 1.73205 and 4.5, respectively. The conservative force coefficient of fluid particles, a_f, is set to 3. The dynamic viscosity of the fluid was determined from the plane Couette flow simulations with Lees-Edwards boundary conditions and is equal to 2.19. The walls are modeled as *three layers* of DPD particles which move with prescribed velocity U_x, in combination with bounce-back boundary conditions. Specifically the bounce-back rule is now implemented in a reference frame where the wall is stationary. The conservative force for wall particles is computed as described earlier, see equation (5.3); we obtained $a_w = 0.9275$. The domain was subdivided into 20 bins in the $x-$ and $y-$directions, and data were

collected at 16 points during the periodic cycle by phase-averaging over the last 5 time steps over 50 periods. The fluid velocity profiles at 16 instances during one full

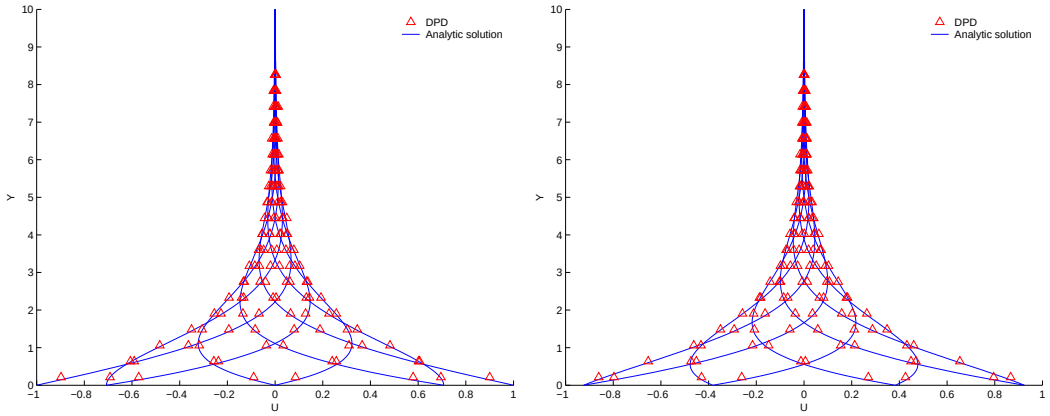

Figure 5.14: Unsteady Stokes flow. Shown are flow velocity profiles at 16 instances during the period. Left: Time $t = 2k\pi/8$, $k = 0, .., 7$. Right: $t = (2k + 1)\pi/8$, $k = 0, .., 7$. DPD simulations – triangles; exact solution – line.

period plotted against the normalized distance from the oscillating wall are shown in figure 5.14. The normalized distance is defined as $Y = y(\nu/\Omega_x)^{-1/2}$, where ν is kinematic viscosity of the fluid. The analytic solution is shown with solid line, while the DPD results are shown with triangles. The results of DPD simulations are in a good agreement with the analytic solution. We note here that the results are very sensitive to the boundary conditions. In the presence of slip at the oscillating wall, the lower points on the sides of the plot will not match the analytic solution.

5.4.3 Finite Reynolds number lid-driven cavity flow

Next we consider flow in a lid-driven cavity at finite values of Reynolds number and we compare results with high-order accurate Navier-Stokes solutions. The DPD simulation parameters are similar to the previously described case. Here, the lower wall is moving with a constant velocity, $U_x = 0.5475$, see figure 5.15, and the Reynolds number is 25. The simulation results are averaged over 200,000 time steps. We compare DPD results with spectral element simulation results based on the solver NEKTAR [35]. Specifically, the 2D spectral element simulations were performed in a

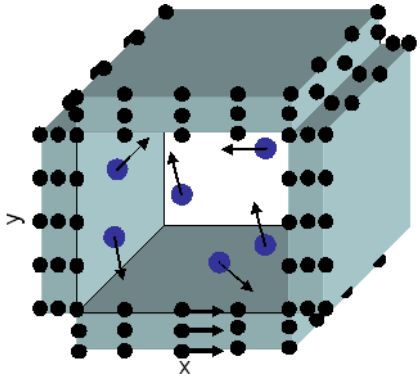

Figure 5.15: Lid-driven cavity flow. The fluid domain is a cube, periodic in one direction. The walls are simulated by freezing DPD particles in combination with bounce-back boundary conditions. The lower wall is moving with constant velocity.

square domain. The size of the domain is 1×1; it is discretized into 900 quadrilateral spectral elements with fourth-order polynomial expansion employed in each element. On one wall, a constant velocity is prescribed, $U_x = 1.0$ while no-slip boundary conditions are used on other walls. The Reynolds number is set to 25.

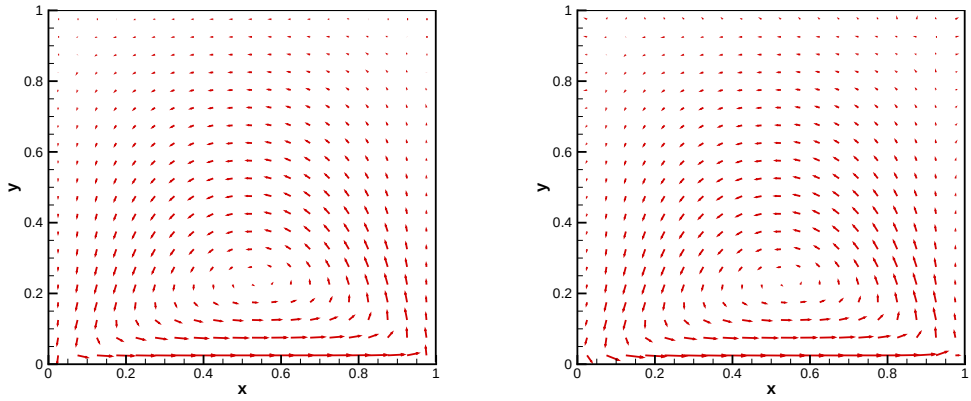

Figure 5.16: Lid-driven cavity flow. Velocity vector field comparison. On the left, results from spectral element simulations; on the right, results from DPD simulations. The coordinates are normalized by the domain size, velocity by U_x.

In figure 5.16, we present the computed velocity vector fields for spectral element and DPD simulations. We have good agreement between the two simulations. We

extract two velocity profiles, vertical and horizontal cuts through the center of the domain, and present a more detailed comparison of simulation results in figure 5.17. On the left, the velocity magnitudes along the vertical cut and on the right along the horizontal cut are shown. The spectral element simulation results are shown with lines, DPD results are shown with triangles. Again, we have very good agreement.

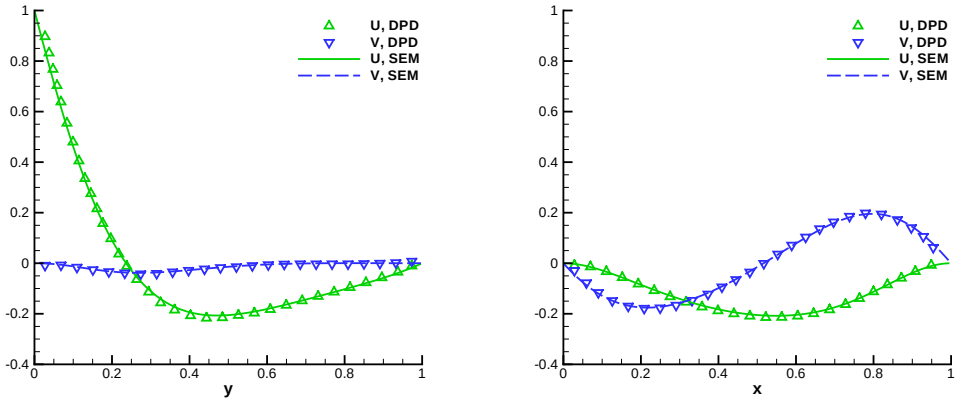

Figure 5.17: Lid-driven cavity flow. Velocity profiles extracted along the vertical and horizontal lines. The coordinates are normalized by the domain size, velocity by U_x.

5.5 Summary

In this chapter we have introduced a new approach to impose the no-slip boundary condition for simple- and complex-geometry flows. The main result is summarized in equations (5.3) and (5.4) that present formulae for the wall conservative parameter and the effective wall-fluid particle conservative parameter. The specific formulae given are for a fluid with density ρ_f in the range between 3 and 25, which covers values most often used in DPD simulations. For other densities a similar procedure, as the one we outlined here, can be developed to obtain an effective wall-particle interaction force. The presence of some density fluctuations in narrow regions very close to the boundaries is caused by the conservative forces. To the best of our knowledge, all previously published methods for imposing no-slip condition exhibit

some degree of density fluctuations, even the method of [76] where the velocity profile extends beyond the surface and into the wall solid boundary. In chapter 8 we will present another method which completely eliminates density fluctuations.

Chapter 6

Coarse-graining in DPD

6.1 Introduction

DPD is intrinsically a coarse-graining technique, and thus it is interesting to evaluate the accuracy of DPD simulation results as a function of the number of molecules per DPD particle. The number of molecules per DPD particle is known as the coarse-graining parameter and is denoted by N_m, see [24]. As such, the proper comparison of DPD results should involve a microscopic method, such as molecular dynamics (MD). The question then is what happens as we coarse-grain the DPD model, i.e., at values of $N_m > 1$, and what is an upper limit value for acceptable accuracy, for confined systems, i.e., flow systems with solid boundaries.

Unlike an MD simulation where the choice of potential is based on a theoretical model of the physical system to be simulated, a DPD simulation involves potentials of a form independent of the physical system. The DPD potentials do, however, include parameters that need to be properly chosen to provide an accurate approximation of the system. Also, an MD simulation contains a set of units intimately related to the theoretical model. Since, with DPD, the potentials are not given by a physical model, the relation of natural DPD length and time scales to physical units needs to be established.

In the present chapter, we propose a process of choosing the DPD parameters and determining the DPD length and time scales for different values of N_m such that the

DPD simulations correspond to an MD simulation of a Lennard-Jones (LJ) liquid. The link between the molecular (MD) and mesoscale approach (DPD) is established by determining a thermodynamic property, here the *compressibility modulus*, from MD simulations and adjusting the parameters in the DPD model accordingly. This approach for linking molecular with mesoscopic scales has been proposed by many researchers, e.g. see [49]. After determining the correct parameters and scales, we evaluate the accuracy of the DPD method based on results obtained from MD simulations and Navier-Stokes solutions. The influence of solid boundaries is typically very strong in DPD simulations, and, to this end, we employ both exact boundary conditions, e.g. the Lees-Edwards boundary conditions [38], as well as boundary conditions developed in chapter 5. The two prototype cases we consider are the plane Poiseuille flow and flow around a periodic array of square cylinders. For the former we also use the analytical Navier-Stokes solution for comparison while for the latter we employ spectral/hp element discretizations [35] to obtain highly accurate numerical solutions.

In the next section, we provide a brief overview of the basic MD formulation establishing notation and corresponding units. We then present equilibrium and non-equilibrium simulations to obtain the shear viscosity, which we use in MD and DPD simulations of simple- and complex-geometry domains.

6.2 MD Basics and Units

In our MD simulations, a system of N particles interact via the pairwise Lennard-Jones potential

$$u_{ij}(r_{ij}) = 4\epsilon\Big[\Big(\frac{\sigma}{r_{ij}}\Big)^{12} - \Big(\frac{\sigma}{r_{ij}}\Big)^{6}\Big]. \tag{6.1}$$

Therefore, the force on particle i is given by

$$\vec{F}_i = \sum_{j \neq i} \vec{\nabla}_{r_{ij}} u_{ij}(r_{ij}), \tag{6.2}$$

where r_{ij} is the distance between particle centers, and $\vec{r}_{ij} = \vec{r}_i - \vec{r}_j$.

Once the force on each particle has been determined, the motion of each particle is computed by integrating Newton's second law. In our case, either the fifth-order Gear predictor-corrector or the Verlet algorithm [2] performed the time integration. In most of our simulations, we use a modified Lennard-Jones potential

$$u_{ij}^{*} = \begin{cases} u_{ij}(r_{ij}) - u_{ij}(r_{cut}), & r_{ij} < r_{cut} \\ 0, & r_{ij} \geq r_{cut} \end{cases} \tag{6.3}$$

to reduce the computation time. The modified potential allows for the use of a linked list which further reduces the computational cost.

In the non-equilibrium simulations, it is important to control the temperature of the system as we do work on it. For this purpose, we chose to use the extended system Nosé-Hoover thermostat, see [21]. Essentially, this thermostat works by extending the Hamiltonian system to include another variable which moves in accordance with its own potential and scales the velocities of the particles to attain the specified temperature.

In a typical MD simulation of an LJ fluid, the variables and parameters are in terms of reduced units. This set of units is closely linked with the LJ potential, whereby σ is the unit of length, m is the unit of mass, and ϵ is unit of energy. From here, we can define the unit of time, $\tau = (m\sigma^2/\epsilon)^{\frac{1}{2}}$. Further combinations of these parameters provide the reduced units of other variables, see Appendix B of Ref. [2].

6.3 The Lennard-Jones Fluid for DPD Simulations

In the previous section we provided a brief introduction to the components of MD simulations. The LJ reduced units of mass, length, and time were presented. In this section, we provide a detailed description of our proposed strategy for determining the DPD parameters and length scale as they correspond to the simulation of a LJ fluid. This method also includes instructions on determining the DPD time scale, which we refer to as τ_{DPD}, and the mass of a DPD particle, M. With these relations, we can then simulate a LJ liquid using DPD with different levels of coarse-graining

N_m.

Our procedure is as follows:

a. Based on the definition of N_m, we determine

$$M = mN_m. \tag{6.4}$$

b. We relate R_c to σ by equating the mass density of the DPD system with that of the MD system.

c. To find the conservative force coefficient, a, we equate the isothermal compressibility of the DPD system with that of the MD system.

d. The values of γ and σ_R are chosen based on the temperature of the DPD system, simulation time step and integration scheme. In addition, γ and σ_R must also satisfy equation (4.6).

e. By insisting the DPD kinematic viscosity is equal to the MD kinematic viscosity, we extract the DPD time scale, τ_{DPD}.

The method outlined above ensures the mass density, viscosity, and the compressibility of the DPD simulation are the same as those of the MD system. Specifically, this means the *linear* responses of the pressure to density changes and shear stress to shear rate are the same for both systems. Therefore, this method is suitable for regimes where the flow remains Newtonian and is nearly incompressible. With the isothermal compressibility being both a function of density and temperature, the above method only provides the *local* DPD parameters and unit scales with respect to the point of interest on the phase diagram. Therefore, if one wishes to conduct simulations at two different phase points, the calibration must be performed twice.

Since the current DPD version performs only isothermal simulations, the temperature of the system, $[k_BT]_{\text{DPD}}$, is an input. Usually, $[k_BT]_{\text{DPD}} = 1$, but one is not limited to this choice. For example, thoughout this study, we choose $[k_BT]_{\text{DPD}} = 0.1$. The choice of DPD temperature manifests itself in the resulting DPD timescale.

6.3.1 The DPD Cut-off Radius

In addition to finding the working parameters for DPD, we need to relate the length scale of DPD, R_c, to σ. This is done by matching the mass densities of the two systems. We denote the dimensional MD number density as ρ_{MD} which has units of σ^{-3}. The DPD number density is denoted by ρ_{DPD} and has units of R_c^{-3}. Therefore, the MD and DPD mass densities are $m\rho_{\mathrm{MD}}$ and $M\rho_{\mathrm{DPD}}$ respectively. In order to equate the two, we must write the DPD expression for mass density in term of reduced units. Explicitly, the DPD mass density is $N_m m\rho^*_{\mathrm{DPD}}(\sigma/R_c)^3$ where ρ^*_{DPD} has the same numerical value as ρ_{DPD} but units of σ^{-3}. After equating the MD and DPD expressions, we obtain

$$R_c = \left(\frac{N_m \rho^*_{\mathrm{DPD}}}{\rho_{\mathrm{MD}}}\right)^{\frac{1}{3}} \sigma. \tag{6.5}$$

In all the cases considered $\rho_{\mathrm{MD}} = 0.8\sigma^{-3}$ and $\rho_{\mathrm{DPD}} = 3.0R_c^{-3}$. The choice of ρ_{DPD} is somewhat arbitrary provided $\rho_{\mathrm{DPD}} > 2.0R_c^{-3}$, see [24].

6.3.2 The Conservative Force Coefficient

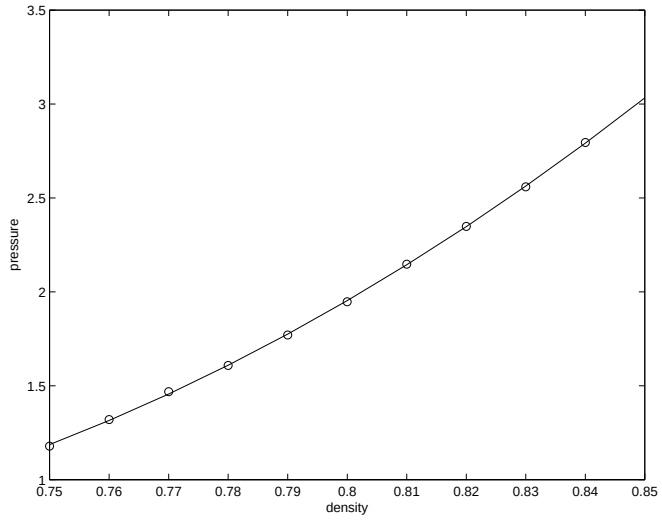

Figure 6.1: Pressure versus density obtained from MD simulations for different values of density in order to determine the compressibility of the LJ fluid at $T = 1.2\epsilon/k_B$. Here, we find for $\rho_{\mathrm{MD}} = 0.8\sigma^{-3}$, $\kappa^{-1} = 15.38$.

To find the value of $a = a_{ij}$ in equation 4.4, we follow the process laid out by

Groot & Warren [24] and Groot & Rabone [23], that is, we match the compressibility of the DPD system with that of the MD system. In [24], the authors, through a series of equilibrium simulations with different values of a and ρ_{DPD}, showed that for sufficiently large number densities, the DPD equation of state, to a good approximation, is given by

$$P = \rho_{\mathrm{DPD}} k_B T + \alpha a \rho_{\mathrm{DPD}}^2$$

where α was determined to be 0.101 ± 0.001. By definition, the isothermal compressibility is $\kappa^{-1} = 1/k_B T \left(\partial p/\partial n\right)_T$ where n is the number density of actual particles which, in units of R_c^{-3}, is $n = N_m \rho_{\mathrm{DPD}}$. Following [23], we find

$$\kappa^{-1} = \frac{1}{k_B T}\left(\frac{\partial p}{\partial \rho_{\mathrm{DPD}}}\right)_T \left(\frac{\partial \rho_{\mathrm{DPD}}}{\partial n}\right) = \frac{1}{N_m}\left(1 + 2\alpha \frac{a \rho_{\mathrm{DPD}}}{k_B T}\right).$$

The above equation provides the necessary relationship between the mesoscopic model parameter and the compressibility system. Therefore, with κ^{-1} determined by the MD system, the proper value of the conservative force coefficient can be found from

$$a = k_B T \frac{\kappa^{-1} N_m - 1}{2\alpha \rho_{DPD}}. \tag{6.6}$$

To obtain κ^{-1}, we conduct equilibrium isothermal MD simulations where the pressure is computed over a range of densities. The pressure can be found by one of two equivalent ways. First, it can be taken as the average of the three diagonal components of the stress tensor as given by (6.9). Second, the pressure can be computed via the internal virial

$$P = \left\langle \rho k_B T + \frac{1}{6} \sum_{i=1}^{N} \sum_{j=1, j\neq i}^{N} \vec{r}_{ij} \cdot \vec{f}_{ij} \right\rangle$$

In an MD simulation, the pressure is affected by the cut-off radius of the modified LJ potential. We can correct the pressure by using (see [21])

$$P_{cor} = P + \frac{16}{3}\pi\rho^2 \Big[\frac{2}{3}\Big(\frac{1}{r_{cut}}\Big)^9 - \Big(\frac{1}{r_{cut}}\Big)^3\Big].$$

	$N_m = 1$	$N_m = 2$	$N_m = 3$	$N_m = 4$	$N_m = 5$
a/k_BT	23.96	49.58	75.21	100.84	126.47

Table 6.1: Values of the conservative coefficient a in DPD units for different levels of the coarse-graining parameter N_m.

The value of κ^{-1} was found by running equilibrium simulations with $N = 2916$ and $r_{cut} = 2.5\sigma$ at $T = 1.2\epsilon/k_B$. The pressure was computed for $\rho_{\text{MD}} = 0.75\sigma^{-3}$ to $\rho_{\text{MD}} = 0.84\sigma^{-3}$. In each instance, the Verlet algorithm was used to advance each system to $t = 200\tau$ with $\Delta t = 0.005\tau$. The pressure of the system, was recorded every timestep after $t = 10\tau$ and averaged over the 190τ period. The plot of the determined pressure versus density is shown in figure 6.1. The data points are fitted with a quadratic function. By taking the derivative of this function and dividing by the temperature, we find $\kappa^{-1} = 15.38$ for $\rho_{\text{MD}} = 0.8\sigma^{-3}$. Table 6.1 lists the values of the conservative coefficient a given by (6.6) using this value of κ^{-1}.

6.3.3 The Random and Dissipative Force Coefficients

The random force coefficient, σ_R, and the dissipative force coefficient, γ, are chosen to yield an efficient and numerically stable DPD simulation that satisfies (4.6). As the random force increases, the speed at which the system reacts to temperature variations increases [24]. This leads to efficient temperature equilibration. There is, however, an upper limit to one's choice of σ_R. This upper limit is based on the time integration scheme, time step and temperature. In our DPD simulations, the time integration scheme was the modified velocity Verlet method with parameter $\lambda = 0.5$ [24], the time step was $\Delta t = 0.02\tau_{\text{DPD}}$ and the temperature was $[k_BT]_{\text{DPD}} = 0.1$. Figure 6.2 shows the normalized equilibrium temperature deviation as function of σ_R for these simulation parameters. The results show that temperature deviation grows rapidly if σ_R is greater than $4.4\sqrt{M\epsilon_{\text{DPD}}/\tau_{\text{DPD}}}$. For even higher values, the simulation is unstable. Therefore, to have an efficient and stable simulation, we choose $\sigma_R = 3.0\sqrt{M\epsilon_{\text{DPD}}/\tau_{\text{DPD}}}$. With this value of σ_R, we must have $\gamma = 45.0M/\tau_{\text{DPD}}$ to

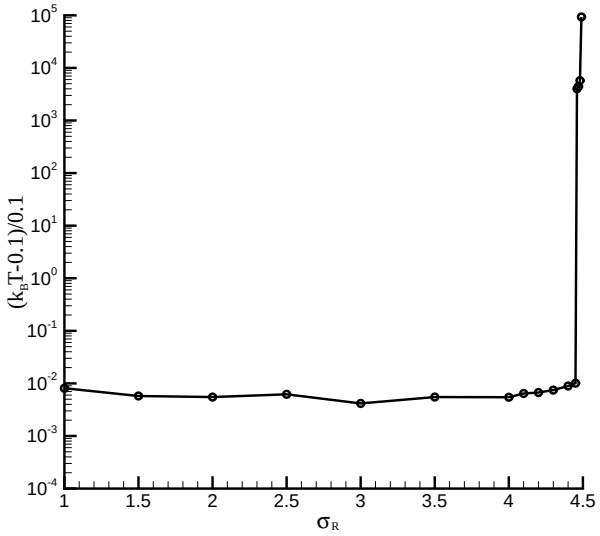

Figure 6.2: Temperature of DPD system as a function of the random force parameter σ_R. ($\Delta t = 0.02\tau_{DPD}; [k_BT]_{DPD} = 0.1$)

satisfy (4.6).

6.3.4 The DPD Time Scale

Just as in the case of the length scale, we must relate the time scale of DPD with that of MD. In this case, it is not so clear how the two are related. In [23] the authors use the diffusion constant of the DPD simulation and matched it to that of the molecule of interest to determine their time scale. They, however, were concerned with the diffusion of water through a membrane. In our cases where we apply shear to the fluid, our time scales are related through the diffusion of vorticity, i.e. the kinematic viscosities. As such, we determine our DPD time scale by matching the kinematic viscosities of our systems. We denote the MD kinematic viscosity as ν_{MD} which has units σ^2/τ. For DPD, the kinematic viscosity is written as ν_{DPD} and has units of $R_c^2/\tau_{\mathrm{DPD}}$. The DPD viscosity can be rewritten as $\nu^*_{\mathrm{DPD}} \left(R_c/\sigma\right)^2 \tau/\tau_{\mathrm{DPD}}$ where ν^*_{DPD} has the same numerical value as ν_{DPD}, but units of σ^2/τ. Then, by equating the viscosities, the DPD time scale is given by

	$N_m = 1$	$N_m = 2$	$N_m = 3$	$N_m = 4$	$N_m = 5$
R_c/σ	1.5536	1.9574	2.2407	2.4662	2.6566
$\tau_{\rm DPD}/\tau$	0.34	0.67	1.04	1.48	2.03

Table 6.2: Values of the DPD time scale $\tau_{\rm DPD}$ in terms of the MD time scale τ for different values of the coarse-graining parameter N_m. Here we take $[k_BT]_{\rm DPD} = 0.1$.

$$\tau_{\rm DPD} = \frac{\nu^*_{\rm DPD}}{\nu_{\rm MD}} \left(\frac{R_c}{\sigma}\right)^2 \tau. \tag{6.7}$$

The MD and DPD viscosities are determined by conducting equilibrium and nonequilibrium simulations. The details and results of these simulations are given in the next section. Equation (6.7) yields the values that are listed in Table 6.2. It may seem alarming that the resulting timescale for the smaller values of N_m are a fraction of τ. This, however, is a result of choosing a small value of $[k_BT]_{\rm DPD}$.

6.4 Numerical Simulations

We first perform simulations to obtain the shear viscosities of the fluid. Once the viscosities have been determined, we perform simulations of plane Poiseuille flow and flow past a periodic array of square cylinders.

6.4.1 Equilibrium simulations

We first consider equilibrium simulations to determine the shear viscosities of our MD and DPD systems. We calculate the shear viscosity using the Green-Kubo relation

$$\mu = \frac{V}{k_BT} \int_0^\infty \langle \sigma_{\alpha\beta}(0)\sigma_{\alpha\beta}(t)\rangle \, dt, \tag{6.8}$$

	$N_m = 1$	$N_m = 2$	$N_m = 3$	$N_m = 4$	$N_m = 5$	MD
N	6912	3456	2304	1728	1382	1372
Δt (τ)	0.0068	0.013	0.02	0.030	0.04	0.005
t_{sim} (τ)	340	1340	3120	5920	10150	1000
t_{st} (τ)	68	134	208	296	406	10

Table 6.3: Equilibrium simulations: DPD and MD simulation parameters. All values are expressed in reduced units even though the results from this simulation determine the time scales. Note that the DPD simulations were performed on a $(20.52\sigma)^3$ domain whereas the MD simulations were performed on a $(11.97\sigma)^3$ domain.

where $\sigma_{\alpha\beta}$ is an off-diagonal component of the stress tensor given by the Irving-Kirkwood formula

$$\sigma_{\alpha\beta} = -\frac{1}{V}\Big(\sum_{i=1}^{N} m v_{i\alpha} v_{i\beta} + \frac{1}{2}\sum_{j=1, j\neq i}^{N} r_{ij\alpha} f_{ij\beta}\Big). \tag{6.9}$$

To ensure accurate results for the MD simulation, we did not use a cut-off potential. It has been shown, however, that using a cut-off potential can also yield accurate results as long as $r_{cut} > 4.5\sigma$ [45].

In Table 6.3 we list the simulation parameters and Table 6.5 contains the values of the viscosities found via the Green-Kubo relation. In all cases the fully periodic computational domain contained N particles. In reduced units, the DPD and MD simulations correspond to an LJ fluid with $T = 1.2\epsilon/k_B$ and $\rho = 0.8\sigma^{-3}$. In the MD simulation the domain was $11.97\sigma \times 11.97\sigma \times 11.97\sigma$ whereas the DPD simulation domain was $20.52\sigma \times 20.52\sigma \times 20.52\sigma$. The simulations were run to time $t = t_{sim}$ to determine the viscosity. The data were collected after a transient time period $t = t_{st}$. For MD, the Verlet scheme was used for the time integration. We note that for these equilibrium simulations a much smaller domain was used in MD compared to DPD. However, in all other simulations presented below the same size domain was involved in both simulation approaches.

6.4.2 Lees-Edwards simulations

A plane Couette flow generated by Lees-Edwards boundary conditions [38] provides a second way of computing the viscosities of the DPD and MD systems. This is a boundary-free simulation independent of the specific implementation (MD, DPD, etc.) that is employed to impose the no-slip boundary conditions. The shear is imposed in the x direction with the velocity gradient in z direction. Therefore, we can calculate the shear viscosity from the relation:

$$\langle \sigma_{xz} \rangle = \mu \frac{\partial u}{\partial z}, \tag{6.10}$$

where σ_{xz} is given by equation (6.9).

In Table 6.4 we list the simulation parameters; the resulting values of the shear viscosity calculated from the non-equilibrium Lees-Edwards simulations are found in Table 6.5. The agreement with the values obtained through the Green-Kubo relations is good. The simulations were run with N particles in a fully periodic domain. The domain for all simulations was $20.52\sigma \times 20.52\sigma \times 20.52\sigma$. Again, $T = 1.2\epsilon/k_B$ and $\rho = 0.8\sigma^{-3}$. For the MD simulations, the fifth-order Gear predictor-corrector was the time integration scheme, and the Nosé-Hoover thermostat kept the temperature at the desired value. Velocity and stress data was recorded every time step after $t = t_{st}$ to the end of the simulation when $t = t_{sim}$ and averaged over this period. The z dimension of the domain was divided into twenty-four bins over which the velocity and shear stress were averaged.

Now that we have established the shear viscosities of our DPD system for different values of N_m, we can, as we have explained in the section 6.3, find the appropriate relation between τ_{DPD} and τ for each N_m.

With the time scales established, we turn our attention to non-equilibrium flows in which we can both confirm the method of choosing DPD parameters and units and explore the effects of coarse-graining on DPD flow simulations.

	$N_m = 1$	$N_m = 2$	$N_m = 3$	$N_m = 4$	$N_m = 5$	MD
N	6912	3456	2304	1728	1382	6912
Δt (τ)	0.0068	0.013	0.02	0.030	0.04	0.005
t_{sim} (τ)	340	1340	3120	5920	10150	1000
t_{st} (τ)	68	134	208	296	406	10

Table 6.4: Lees-Edwards simulations: DPD and MD simulation parameters. All values are expressed in reduced units even though the results from this simulation determine the time scales. The same size domain is used in DPD and MD simulations.

	$N_m = 1$	$N_m = 2$	$N_m = 3$	$N_m = 4$	$N_m = 5$
$\mu(GK)$	1.05	1.31	1.57	1.84	2.16
$\mu(LE)$	1.04	1.31	1.55	1.82	2.15

Table 6.5: Shear viscosity results from the Green-Kubo (GK) and Lees-Edwards (LE) calculations. The values are expressed in terms of DPD units $(M/(R_c\tau_{\mathrm{DPD}})$. By the method described in the previous section, these values are constructed to be identical (in terms of reduced units) to those found in the MD simulation. The Green-Kubo calculation gave $1.98m/(\sigma\tau)$ as the shear viscosity whereas the Lees-Edwards simulations yielded $1.97m/(\sigma\tau)$.

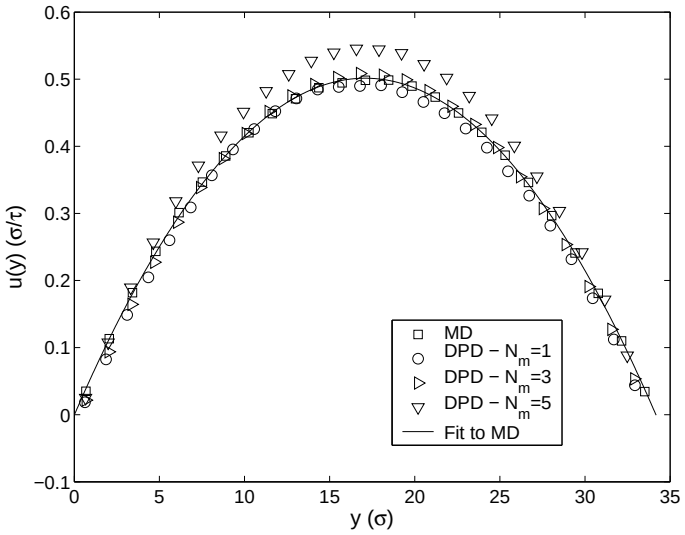

Figure 6.3: Velocity profiles of the Poiseuille flow simulations. The determined DPD spatial and temporal scalings are used such that all the data is reported in MD reduced units. The line is the fit to the MD data while the open squares are the MD data, the open circles correspond to DPD/$N_m = 1$, side triangles to DPD/$N_m = 3$, and the inverted triangles to DPD/$N_m = 5$.

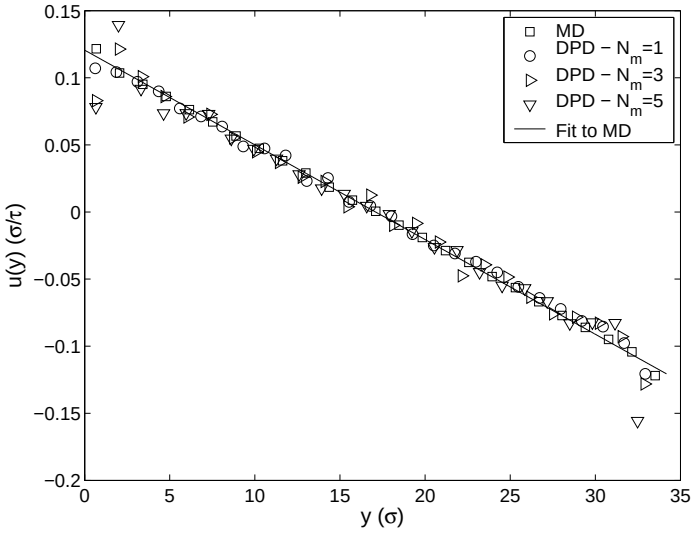

Figure 6.4: Corresponding shear stress profiles of the Poiseuille flow simulations. The legend is the same as in the previous figure.

6.4.3 Poiseuille flow

We aim to compare velocity and stress profiles and examine density fluctuations in MD and DPD Poiseuille flow simulations of an LJ liquid at $T = 1.2\epsilon/k_B$ and $\rho = 0.8\sigma^{-3}$. Based on our derivations of M, R_c and τ_{DPD}, the channel sizes and the imposed pressure gradients in the MD and DPD systems are the same.

With the introduction of bounding surfaces, we adjust our simulations to impose the no-slip boundary condition. In MD, this is accomplished by adjusting the potential between the wall particles and the fluid particles. This can be done in two ways. First, see [69], we can adjust the parameters ϵ_{wf} and σ_{wf} in the LJ potential for wall-fluid particle interactions in addition to adjusting the wall density, ρ_w. Second, see [12], we can include an additional parameter $0 \leq A_{MD} \leq 1$ to multiply the attraction term in the Lennard-Jones potential. Here, we choose the first method since it has been shown to produce a constant slip-length as long as the shear rate is sufficiently small [70]. We find that when our walls are constructed of two (100) layers of an fcc lattice, $\sigma_{wf} = \sigma_{ff}$, $\rho_w = \rho_f$ and $\epsilon_{wf} = 0.6\epsilon_{ff}$ we have no-slip at the wall. For DPD, the walls are modeled using method developed in chapter 5.

To generate the flow, a force is imposed on each particle. In the MD simulation,

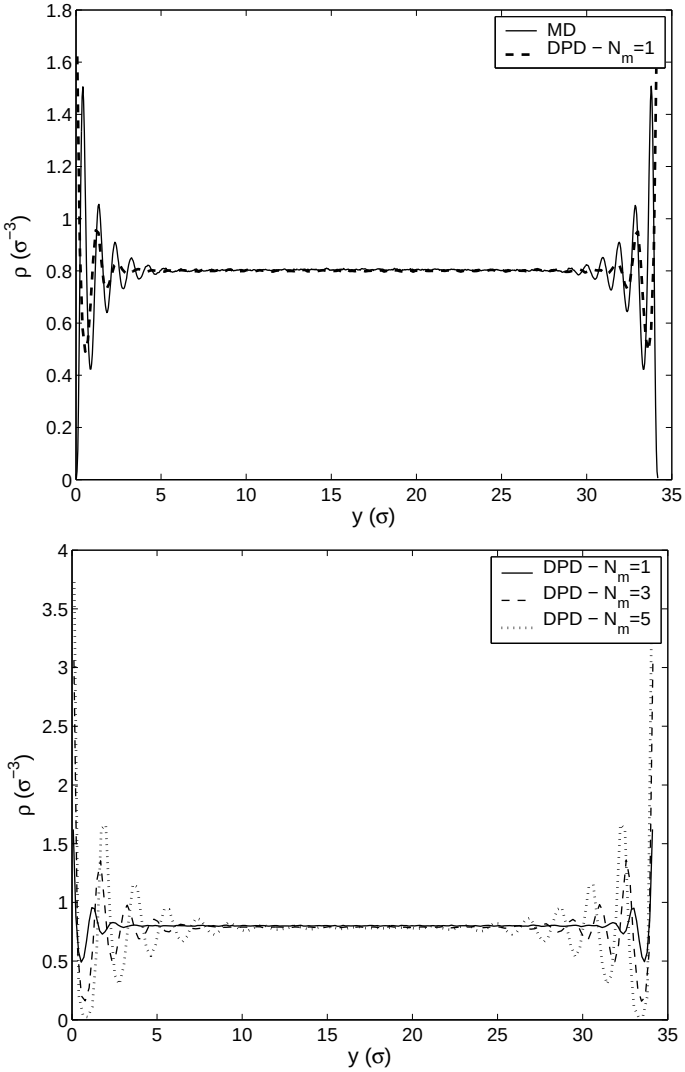

Figure 6.5: Density profiles for Poiseuille flow. In the upper plot the MD density is compared against the DPD density for $N_m = 1$. In the lower plot the DPD density profiles are plotted for $N_m = 1, 3$ and 5.

	$N_m = 1$	$N_m = 3$	$N_m = 5$	MD
N_f	8000	2676	1600	8000
N_w	992	440	304	800
Δt (τ)	0.0068	0.02	0.04	0.005
t_{sim} (τ)	340	3120	10150	15000
t_{st} (τ)	68	208	406	200
h (σ)	0.16	0.22	0.27	0.04275

Table 6.6: Poiseuille flow: MD and DPD simulation parameters in reduced units.

this force was chosen to be $0.0085m\sigma/\tau^2$. Therefore, in reduced units, the corresponding force per particle for the DPD simulations was N_m times this value. Based on this imposed force, the viscosity, and the size of our channel, the Reynolds number of the flow is found to be $Re = 4.6$.

The simulation parameters are summarized in Table 6.6. The number of fluid particles is N_f, while the number of wall particles is N_w. The fluid occupies the region between the two walls. This region has dimensions $34.2\sigma \times 34.2\sigma \times 8.55\sigma$, and is periodic in the x and z directions. The fluid domain is subdivided in y direction into slices of height h where the velocity, density and stress data are collected. The fifth-order Gear predictor-corrector integration scheme with the Nosé-Hoover thermostat is employed in the MD simulation. The simulations were run to $t = t_{sim}$ with timestep Δt and data were averaged over all steps after time $t = t_{st}$.

In figure 6.3 we plot the resulting streamwise velocity profiles from both MD and DPD simulations – the results are in reduced units. Three values of coarse-graining are included in the plot corresponding to $N_m = 1, 3$ and 5. In figure 6.4 we plot the corresponding shear stress obtained from the two types of simulations. We observe a good agreement between the different simulations both in the velocity profile as well as in the shear stress distribution for $N_m = 1, 3$ but large deviations for $N_m = 5$. Figure 6.5 shows the density profile across the channel. We observe that the density fluctuations for MD and DPD simulations corresponding to $N_m = 1$ are similar, with the main difference being the large value of the DPD density at the wall. However, as the value of N_m increases the density fluctuations in the DPD simulations also

	$N_m = 1$	$N_m = 3$	MD
N_f	7500	2504	7500
N_w	512	216	500
Δt (τ)	0.0068	0.02	0.005
t_{sim} (τ)	6800	20800	14000
t_{st} (τ)	340	1040	250
h (σ)	0.16	0.22	0.855

Table 6.7: Flow past array of square cylinders: simulation parameters for DPD with $N_m = 1$, 3 and MD in MD units.

increase, with the $N_m = 5$ case exhibiting very large values at the wall and also inside the flow domain. These large density fluctuations associated with $N_m = 5$ lead to the incorrect velocity profile shown in figure 6.3. There are regions of low density which may be as wide as 1.5σ. In these regions the dissipative force is not effective and we obtain high velocity gradients. It demonstrates that the employed particle-based boundary conditions are not as robust for high values of the conservative force parameter. We note that this value increases when we increase N_m, see Table 6.1.

6.4.4 Flow past an array of square cylinders

Next we consider flow past a periodic array of square elements and perform MD, DPD and Navier-Stokes simulations based on spectral/hp element discretization that provides high-order accuracy [35]. The boundary conditions are similar to those employed in the Poiseuille flow (i.e., no-slip on the elements and periodicity on all outer boundaries), and the force on each particle is the same in both magnitude and direction.

For the simulation of this flow, N_f, N_w and other parameters are listed in Table 6.7. The square cylinder has dimensions $8.55\sigma \times 8.55\sigma \times 8.55\sigma$ and is immersed in a fully periodic domain with dimensions $34.2\sigma \times 34.2\sigma \times 8.55\sigma$, see figure 6.6. The origin of the reference frame is set as shown in figure 6.6, and the flow is along the x direction. The x and y dimensions were divided into bins of size $h \times h$ (see Table 6.7) over which the data were collected. The simulation was run to time $t = t_{sim}$ with

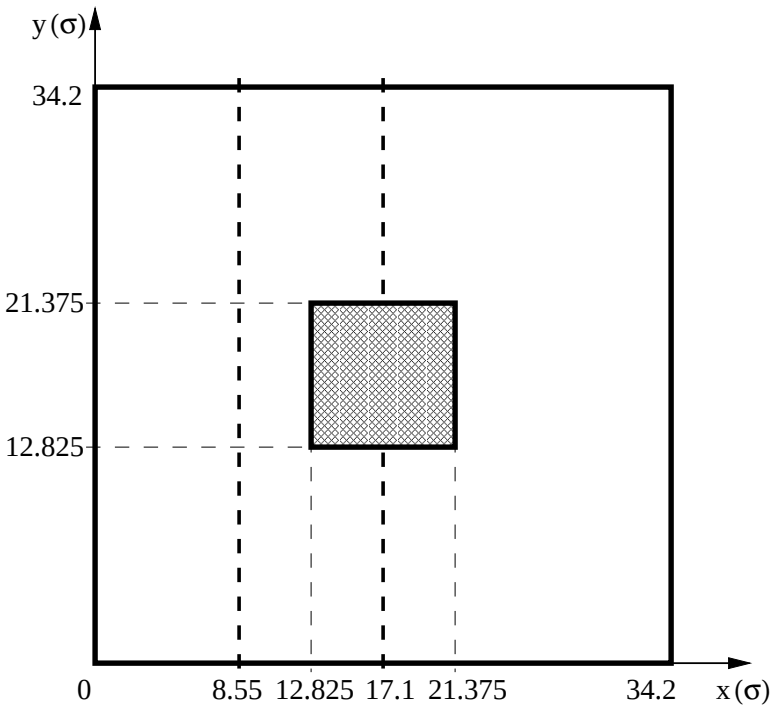

Figure 6.6: The geometry of computational domain for flow past array of square cylinders. The dimensions are in MD units. The thick dash lines are the locations where comparisons are performed.

timestep Δt and data were collected after $t = t_{st}$.

For the spectral/hp element simulation, the computations are done in two dimensions using MD units. The kinematic viscosity of fluid is set to $2.475\sigma^2/\tau$ and the external force is $0.0085m\sigma/\tau^2$. The incompressible two-dimensional Navier-Stokes equations are solved using the spectral/hp element solver Nektar [35]. The domain is discretized into 1500 spectral elements of fourth-order polynomial expansion in each element. The simulation is run until steady state is reached.

First, we compare the DPD results corresponding to different values of the coarse-graining parameter N_m against the results obtained from the MD simulations. In figure 6.7, we plot the streamwise and cross-flow velocity components at the center-plane of the domain, and in figure 6.8 we present similar profiles at another location. Also, in figures 6.9 and 6.10, we plot the corresponding stresses along the y direction. The agreement is good with some small scattering apparent in the stress profiles. We now do similar comparisons of DPD results against the Navier-Stokes solutions

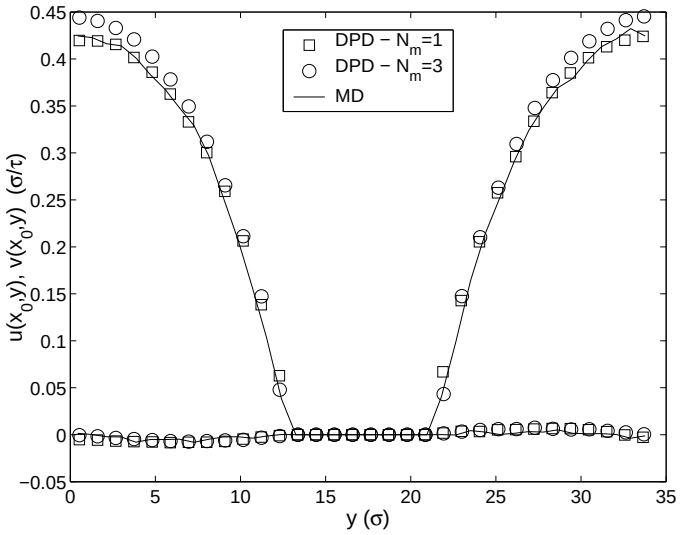

Figure 6.7: DPD versus MD: Plots of the u (streamwise velocity) and v (cross-flow velocity) profiles at the center of the square cylinder ($x_0 = 17.1\sigma$) as given by the DPD and MD simulations.

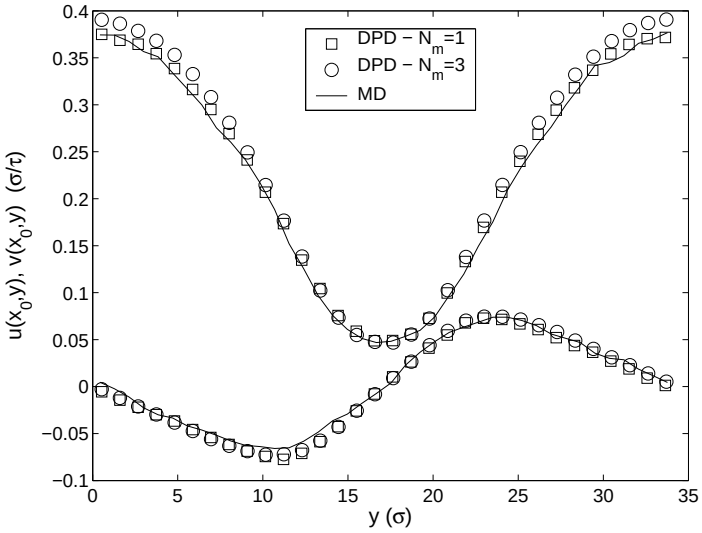

Figure 6.8: DPD versus MD: Plots of the u (streamwise velocity) and v (cross-flow velocity) profiles at $x_0 = 8.55\sigma$.

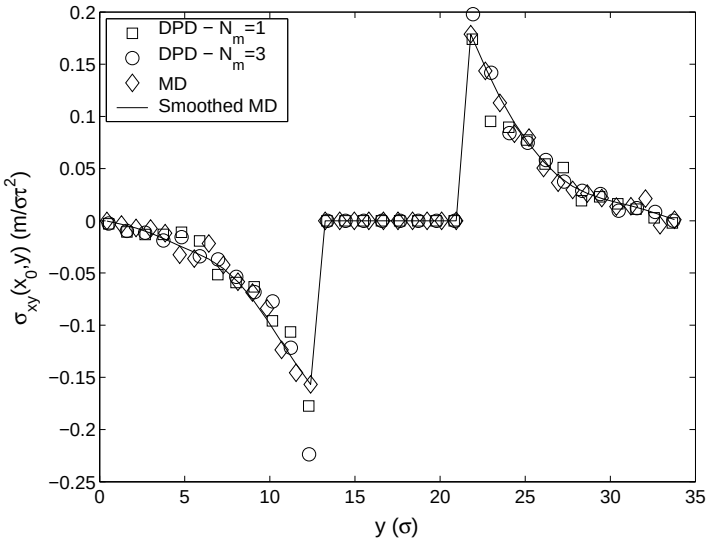

Figure 6.9: DPD versus MD: Plots of the σ_{xy} profiles at the center of the square cylinder ($x_0 = 17.1\sigma$) as given by the DPD and MD simulations.

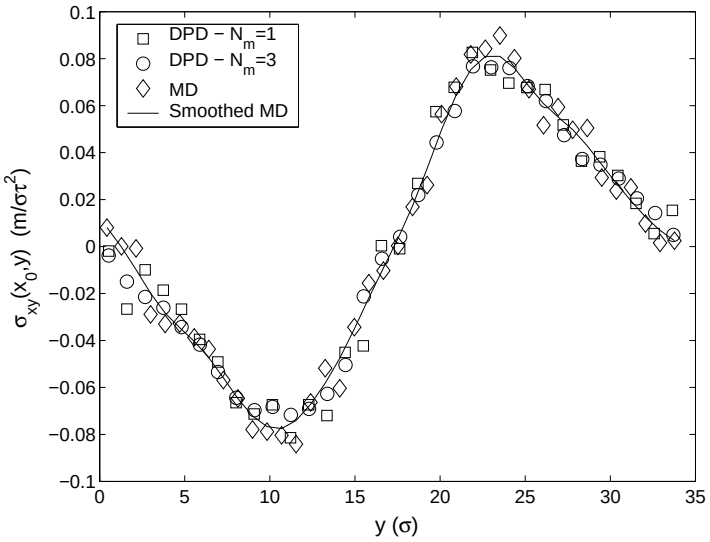

Figure 6.10: DPD versus MD: Plots of the σ_{xy} profiles at $x_0 = 8.55\sigma$.

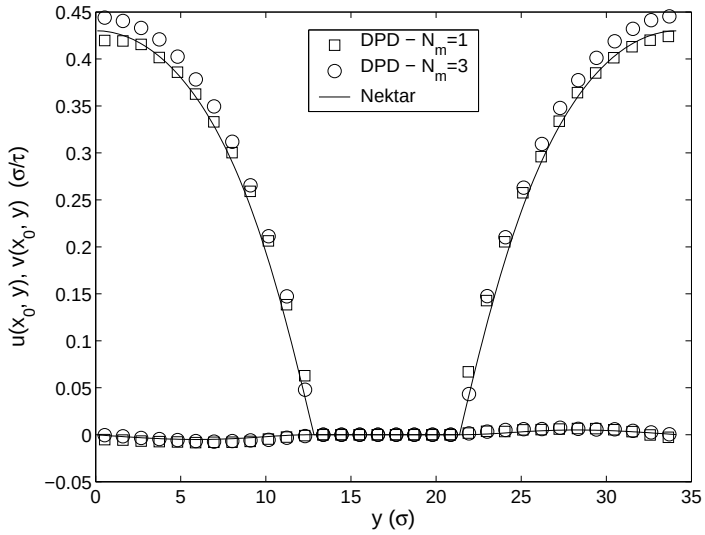

Figure 6.11: DPD versus Navier-Stokes: Plots of the u(streamwise velocity) and v(cross-flow velocity) profiles at the center of the square cylinder ($x = 17.1\sigma$) as given by the DPD and spectral/hp element simulations.

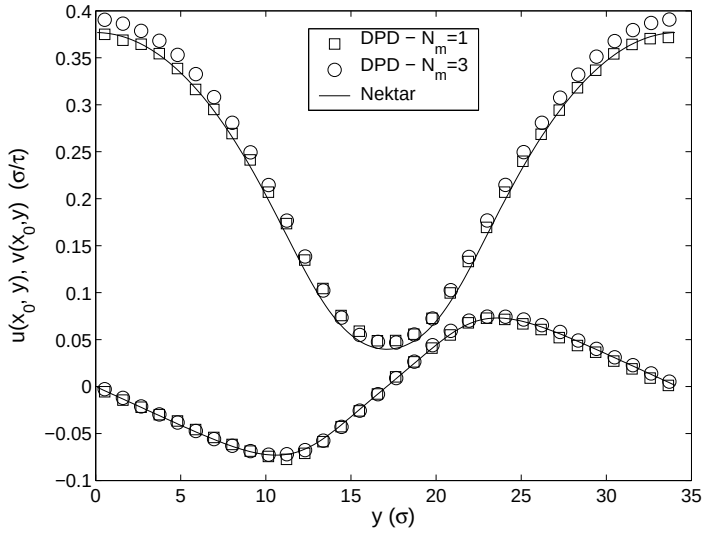

Figure 6.12: DPD versus Navier-Stokes: Plots of the u(streamwise velocity) and v(cross-flow velocity) profiles at $x = 8.55\sigma$.

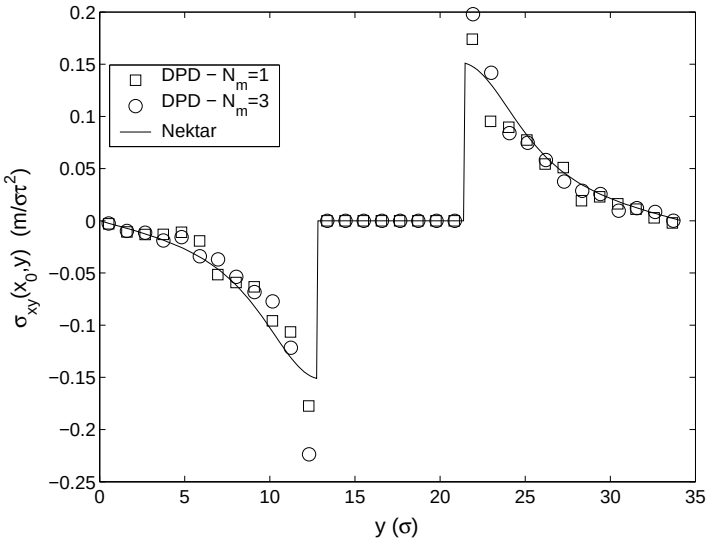

Figure 6.13: DPD versus Navier-Stokes: Plots of the σ_{xy} profiles at the center of the square cylinder ($x = 17.1\sigma$) as given by the DPD and spectral/hp element simulations.

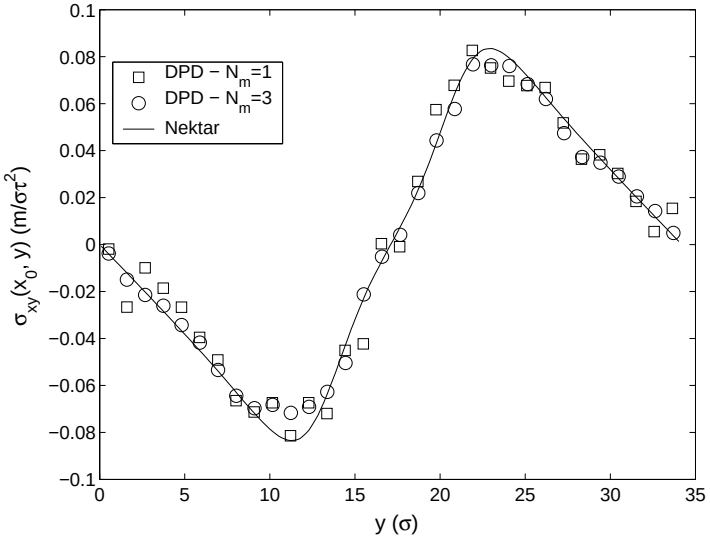

Figure 6.14: DPD versus Navier-Stokes: Plots of the σ_{xy} profiles at $x = 8.55\sigma$.

obtained using spectral/hp element discretizations. In figures 6.11 and 6.12 we plot velocity profiles, and in figures 6.13 and 6.14 we plot the stress profiles.

6.5 Summary

We have shown that for $N_m < 5$ for the channel and for $N_m < 3$ for the cylinder array good agreement is established between DPD and MD (and Navier-Stokes) simulations of continuum, no-slip flows in domains approximately 40σ wide. It is important to note that in addition to the flow quantities, we have, by construction, simulated fluids with the same thermodynamic property, i.e., the same dimensionless compressibility. Furthermore, by matching the densities and the viscosities of the MD and DPD systems, we obtained the appropriate length and time scales for a given degree of coarse-graining represent by N_m. The validity of these choices is illustrated by the agreement of the scaled DPD data with the MD data, and the Navier-Stokes solutions.

The relatively low upper value of the coarse-graining parameter N_m is somewhat surprising. Moreover, it is intriguing that as the coarse-graining parameter is increased larger density fluctuations occur inside the domain. We will address these issues in the following two chapters.

Chapter 7

Limits of Coarse-graining in DPD

7.1 Introduction

Coarse-graining of dense liquid-state systems can potentially lead to fast simulation times, thus providing an effective bridge between atomistic and continuum descriptions. In this chapter we analyze some of the fundamental modeling ideas of DPD and identify three factors that limit its application at high coarse-graining levels: inter-particle force magnitude, compressibility, and geometric confinement.

7.2 DPD Coarse-Graining Procedure

We will apply coarse-graining to a Lennard-Jones (LJ) fluid of density $\rho_{MD} = 0.8\sigma^{-3}$ in a domain $34.2\sigma \times 8.55\sigma \times 34.2\sigma$ in x-y-z, where σ is the atomic diameter. The viscosity of the LJ fluid was obtained via non-equilibrium MD simulations using Lees-Edwards boundary conditions and is equal to $1.97m/(\sigma\tau)$, where m and τ are MD units of mass and time, correspondingly. The dimensionless compressibility $\kappa^{-1} = 15.36$ was found by conducting equilibrium isothermal MD simulations, where the pressure was computed over a range of densities; for details we refer to chapter 6.

In standard DPD method described in section 4.2 the pair of dissipative and random forces constitutes the DPD local thermostat. We will refer to this method as the DPD-Verlet version as we will employ a modified Verlet algorithm to integrate the

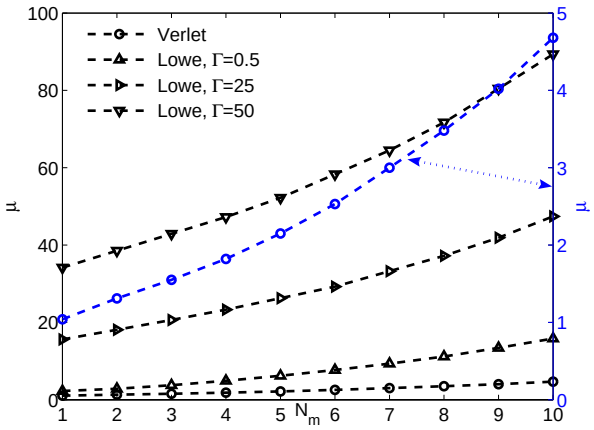

Figure 7.1: Dynamic viscosity (DPD units) of the DPD fluid as a function of N_m. The dashed line in the DPD-Verlet fluid (circles) is a second-order polynomial fit. The right vertical axis corresponds to the Verlet viscosity only.

stochastic equations of motion [24]. An alternative DPD method that employs the Andersen thermostat, instead of the aforementioned pair of forces, has been proposed by Lowe [41]. This method achieves realistic values of the Schmidt number and is less sensitive to the size of the integration time step. Thermal equilibrium is achieved probabilistically by drawing relative velocities from a Maxwell distribution, just like in molecular dynamics (MD) simulations, but for pairs of particles within R_c instead of individual particles as in MD. The probability is $0 \leq \Gamma\Delta t \leq 1$, where Γ is the thermalization parameter with large values corresponding to thermalization of almost all particles. In general, the DPD-Lowe fluid is very viscous so it is of interest to investigate both the DPD-Verlet and the DPD-Lowe versions.

We first compute the viscosity of DPD fluid for $k_BT = 0.1$ ($\sigma_R = 3$, $\gamma = 45$) and different values of the coarse-graining parameter N_m based on the Lees-Edwards method [38]. In figure 7.1 we plot representative values of the dynamic viscosity μ for both the DPD-Verlet and the DPD-Lowe methods. We note that even for small values of the thermalization parameter Γ the DPD-Lowe fluid is more viscous than the DPD-Verlet fluid. In the latter case for $N_m \leq 10$ the viscosity increases approximately as N_m^2.

In the coarse-graining procedure we keep the DPD density constant as we need

N_m	1	5	9	13	17
L	22.01	12.87	10.58	9.36	8.56

Table 7.1: Size of the domain in DPD units at different coarsening levels.

to have $\rho_{DPD} \geq 3R_c^{-3}$ in order to have a liquid phase [24]; hence, the volume of the domain has to decrease accordingly as we increase N_m. In table 7.1 we present the domain size for different values of N_m.

7.3 Open DPD Systems

We first investigate the effect of coarse-graining by performing DPD-Verlet simulations in a fully periodic domain of size $(10R_c)^3$ containing $3,000$ particles. The temperature of the fluid is set to $k_BT = 0.1$ and the DPD force parameters are $\sigma_R = 3$ and $\gamma = 45$. Equation (6.6) is used to calculate the conservative force parameter a. The modified velocity Verlet method (with $\lambda = 0.5$) [24] and time step 0.02 is used to advance the system in time. Initially, all DPD particles are densely packed occupying only a small fraction of the computational domain. After letting the fluid to equilibrate for $80,000$ time steps, we record the mean-square displacement (MSD) for $20,000$ steps.

In three-dimensions and for periodic equilibrium systems, the MSD of atoms is related to the diffusion coefficient D through the Einstein relation

$$D = \lim_{t\to\infty} \frac{\langle[\vec{r}(t) - \vec{r}(0)]^2\rangle}{6t}. \tag{7.1}$$

Equation (7.1) implies that for large times the mean-square displacement grows linearly. The diffusion coefficient is obtained by calculating the slope of MSD versus time in the asymptotic regime. (For non-equilibrium systems the displacement of the atoms due to the bulk transport is subtracted.) In figure 7.2 we plot the MSD for the $N_m = 1$ and $N_m = 100$ cases. The former shows the initial quadratic response and the subsequent linear growth with time, as expected; however, in the latter ($N_m = 100$)

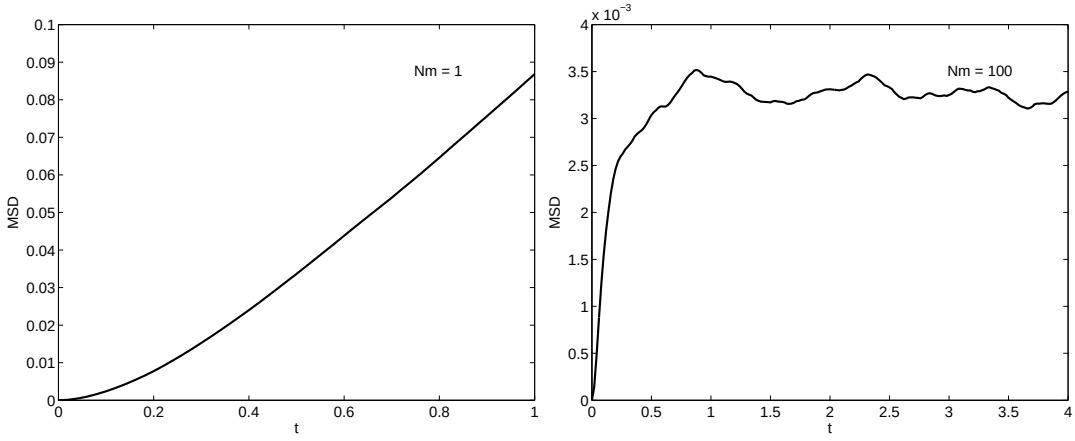

Figure 7.2: Mean-square displacements $N_m = 1$ and $N_m = 100$ measured in a large periodic domain. The results are shown in DPD units.

we observe a very different behavior, more characteristic of solid-like structures. In figure 7.3 we plot the diffusion coefficient D computed for different levels of coarse-graining of the DPD fluid. The values of D gradually decrease with N_m, and for $N_m = 30$ the diffusion coefficient is about 450 times smaller than that for $N_m = 1$.

For homogeneous substances the structural arrangement of atoms depends only on the distance r between atoms. The radial distribution function (RDF) is proportional to the probability of finding two atoms separated by distance r and it is defined by

$$g(r) = \frac{1}{N\rho_{DPD}} \langle \sum_{i}^{N} \sum_{i \neq j}^{N} \delta[r - r_{ij}] \rangle. \tag{7.2}$$

Here, N is the total number of atoms, ρ_{DPD} is the number density, r_{ij} is the distance between centers of atoms i and j, and the angular brackets represent time-averaging. In figure 7.4 we present the radial distribution functions for different levels of coarse graining N_m. In all cases $g(r)$ is computed using equilibrium simulations with $3,000$ particles in the fully periodic domain of size $(10R_c)^3$. The simulations were run for $12,000$ time steps and the RDF was computed during the last $2,000$ steps. RDF is a helpful indicator of the nature of the phase assumed by the simulated system [27]. For atoms frozen onto the sites of regular lattice structures, $g(r)$ takes the form of a sequence of delta distributions (figure 7.5). If atoms are vibrating about

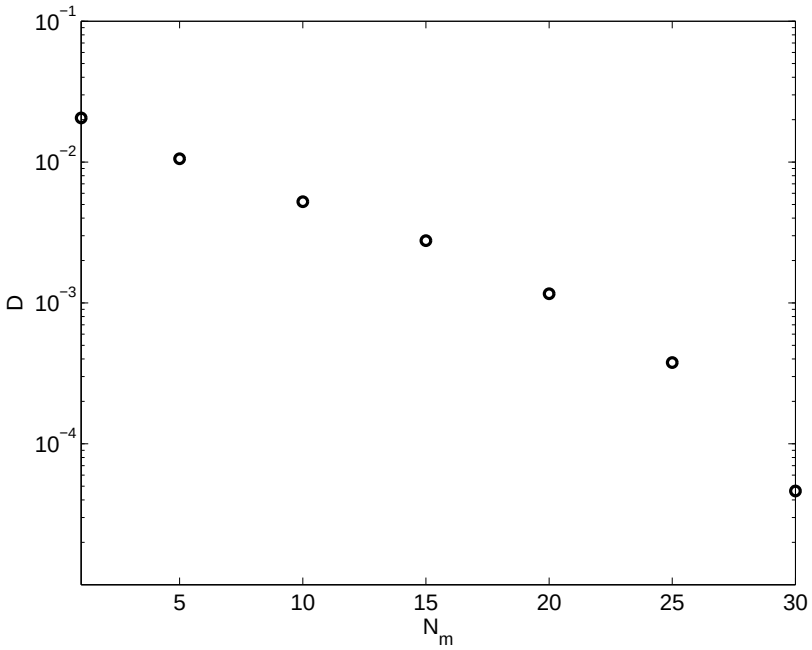

Figure 7.3: Diffusion coefficient as a function of the coarsening parameter N_m measured in a large periodic domain. The results are shown in DPD units.

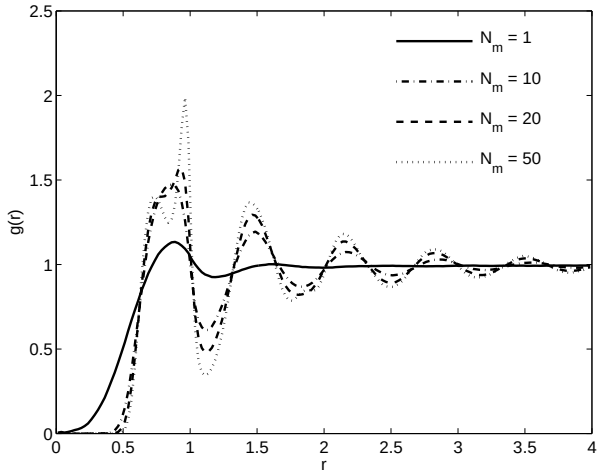

Figure 7.4: Radial distribution function for different N_m in an open DPD system (DPD units).

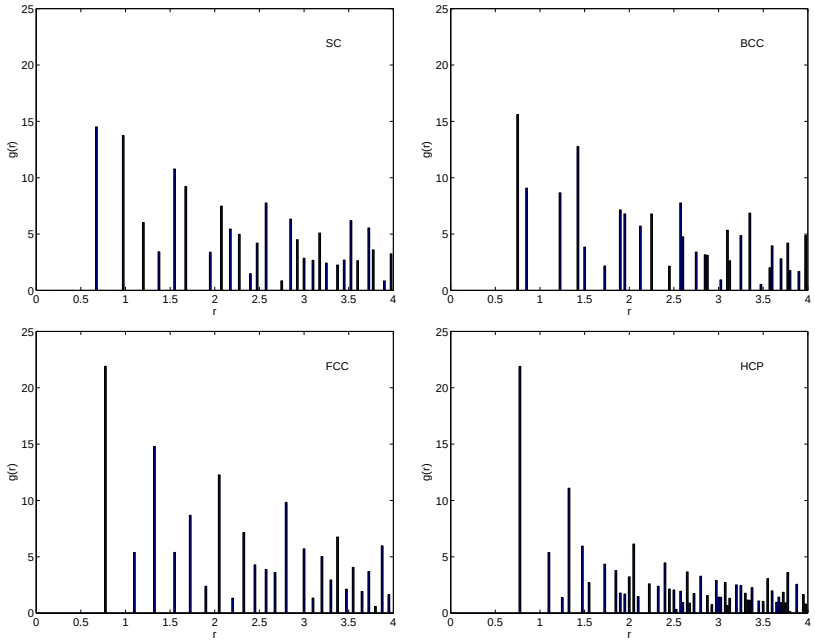

Figure 7.5: Radial distribution functions computed for perfect lattices.

rather than being fixed to the lattice sites, then the delta distributions in $g(r)$ resolve into Gaussians; but the positions and relative heights of those Gaussian distributions still allow determination of the crystalline structure (figure 7.6)[27]. For partially crystalized substances, $g(r)$ may contain secondary peaks not found in $g(r)$ for a liquid. Such additional peaks are caused by remnants of the lattice structure and can be readily seen in figure 7.4 for $N_m \geq 20$. Comparing figures 7.4 and 7.6, we note that the location of the peaks of the RDF for the DPD fluid with large N_m are similar to those of the fcc lattice, therefore we assume the DPD fluid crystalizes to fcc lattice.

Next we study the effect of coarse-graining on the speed of sound in the DPD fluid as this will provide an estimate of compressibility in the coarse-grained DPD system. The isothermal speed of sound is given by

$$c = \sqrt{k_B T + \frac{4\pi\rho}{3} \int_0^\infty |F^C(r)| g(r) r^3 dr} \tag{7.3}$$

and can be obtained from the DPD equation of state [24]

$$p = \rho k_B T + \frac{2\pi\rho^2}{3} \int_0^\infty |F^C(r)| g(r) r^3 dr, \tag{7.4}$$

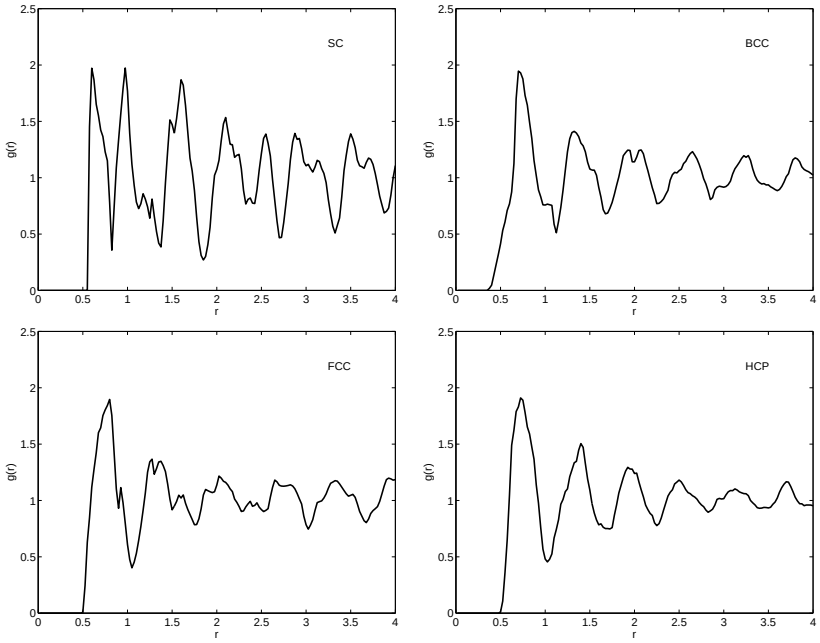

Figure 7.6: Radial distribution functions computed for randomly perturbed lattices.

where $|F^C(r)|$ is the magnitude of the conservative force. The values of the speed of sound given by equation (7.3) as a function of N_m are plotted in figure 7.7. We note here that c increases approximately as $N_m^{1/2}$.

In summary, in this section we have shown that for the specific periodic system we have examined there seems to be an artificial solidification taking place for $N_m \geq 20$ at $k_BT = 0.1$. It is also in agreement with the findings of [71] where such solidification was reported for values of the conservative force coefficient $a \geq 250$ for temperature level $k_BT = 1$. Using equation (6.6) we find that the corresponding value of the coarsening parameter is $N_m \geq 10$, which is more conservative than the limit we established directly here.

7.4 Wall-bounded DPD Systems

We now turn our attention to confined DPD fluid flows. In particular, we will examine Poiseuille flow with two different models for the effect of the wall: (a) ideal periodic walls, and (b) solid DPD walls. We will investigate for both cases the effect of the coarse-graining by examining similar quantities as in the previous section.

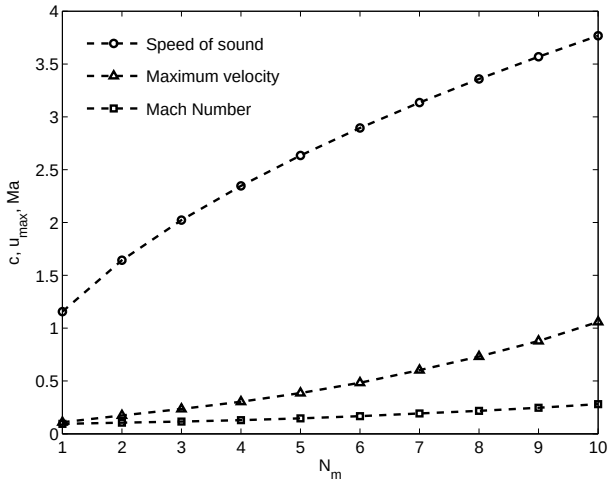

Figure 7.7: Speed of sound c, Poiseuille flow maximum velocity u_{max} (DPD units), and Mach number Ma as functions of N_m.

In the first boundary condition model, we set-up two adjacent counter-flowing Poiseuille flows using periodic boundaries [3]. Specifically, a rectangular domain is doubled in size in the cross-flow z direction and the flow is sustained by applying a body force (x direction) to each particle; the direction of the force is opposite in the two halves of the domains. This is schematically shown in figure 7.8. This periodic Poiseuille flow method (PPFM) produces a flow with uniform density from wall-to-wall apart from the statistical fluctuations. The absence of density artifacts makes PPFM useful for studying the bulk Poiseuille flow (in the continuum limit), i.e., without any density oscillations associated with the presence of solid boundaries. The second boundary condition we use is the model developed in chapter 5.

We report first results with the ideal walls. We employ the same domain as described in the section 7.2 and we double it in the z direction while a body force $F = 0.0085m\sigma/\tau^2$ is applied in the x direction. The simulations are carried out for $410,000$ time steps using the Verlet algorithm while the flow data are collected over the last $40,000$ steps by subdividing the z direction into bins of size $0.2R_c$. These results are further averaged over both halves of the domain.

The DPD density, velocity in x direction, shear stress and partial temperatures are shown in figure 7.9. The agreement with incompressible Navier-Stokes solution for Poiseuille flow is good for $N_m \leq 5$. For $N_m = 6$ there is a slight deviation of the

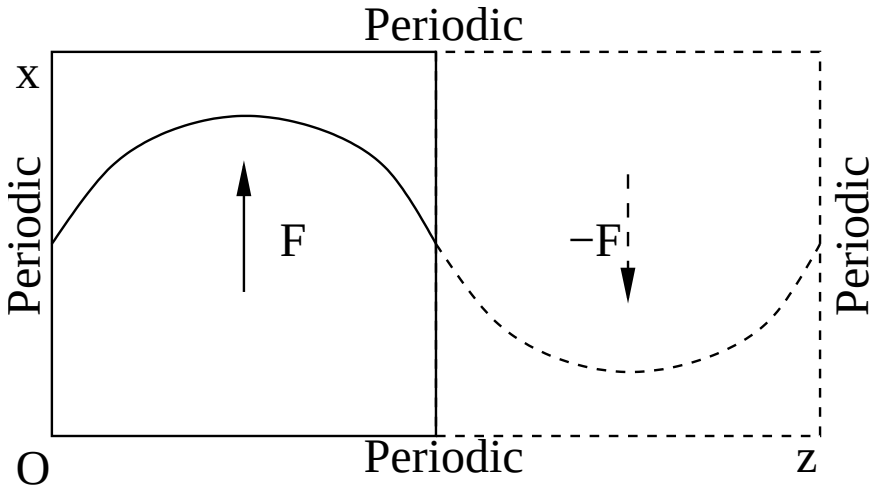

Figure 7.8: Sketch of periodic poiseuille flow method. A rectangular domain is doubled in size in the cross-flow z direction and the flow is sustained by applying a body force (x direction) to each particle; the direction of the force is opposite in the two halves of the domains.

computed velocity profile from the analytic prediction, as well as an increase of the temperature inside the domain. For higher N_m, the results differ significantly from the incompressible Navier-Stokes solution.

To understand these results, we consider the scaling of DPD units of the body force with N_m using an approximate analysis. Let us ignore, at first, the dependence of the DPD length scale on the coarse-graining parameter N_m. As noted in section 7.2 the viscosity of the DPD fluid increases approximately as N_m^2. Since the DPD time scale is roughly proportional to the DPD viscosity, we see that, as a first approximation, the DPD unit of force scales as N_m^4. Assuming the validity of the incompressible Poiseuille flow solution, we obtain that the velocity u_{max} at the center of the channel scales approximately as N_m^2. Given that the speed of sound is roughly only proportional to $N_m^{1/2}$, we obtain that the Mach number scales as $N_m^{3/2}$, thus increasing with N_m. In figure 7.7 we plot the velocity u_{max} and the Mach number $Ma = u_{max}/c$ computed without ignoring the dependence of the DPD unit of length R_c on N_m; the computed results are consistent with the approximate analysis. Specifically, for $N_m > 5$ the Mach number is greater than 0.15 and hence compressibility effects start becoming important.

In order to document this point more accurately we also examine the influence of

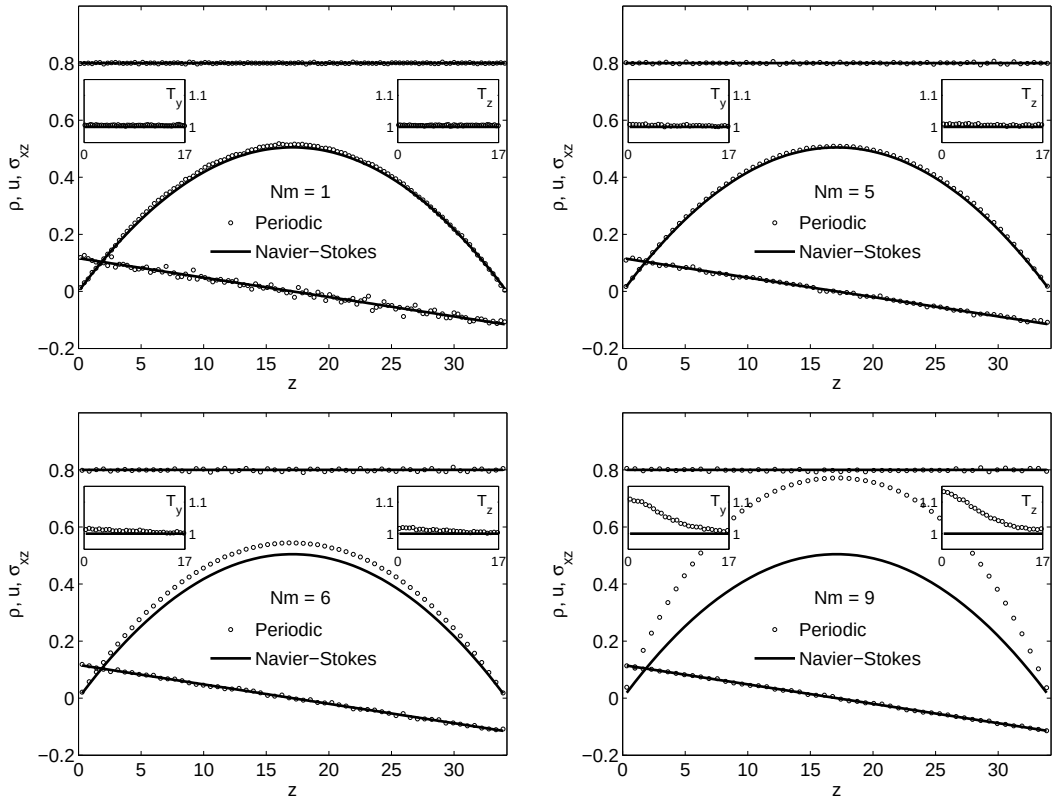

Figure 7.9: Density, velocity, temperature and stress profiles in Poiseuille flow obtained using the periodic boundary condition for different levels of coarse-graining. The results are shown in MD units.

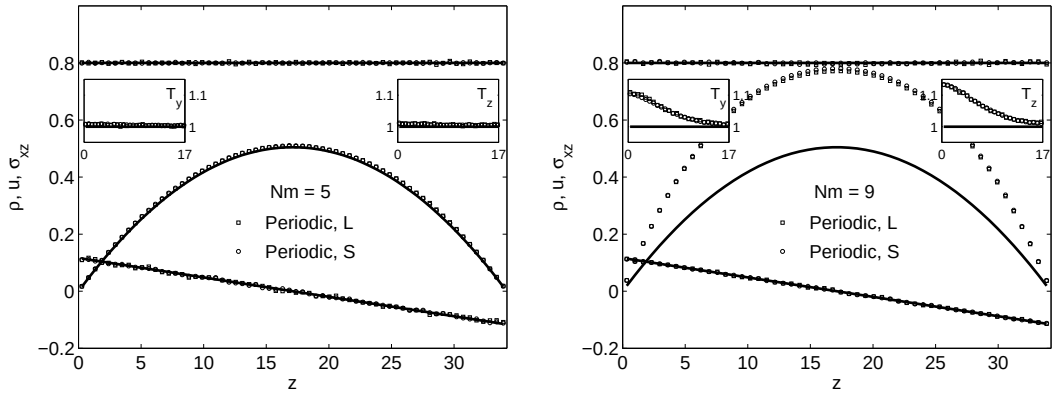

Figure 7.10: Density, velocity, temperature and stress profiles in Poiseuille flow obtained in a large (L) and small (S) domains using the periodic boundary condition for different levels of coarse-graining. The results are shown in MD units.

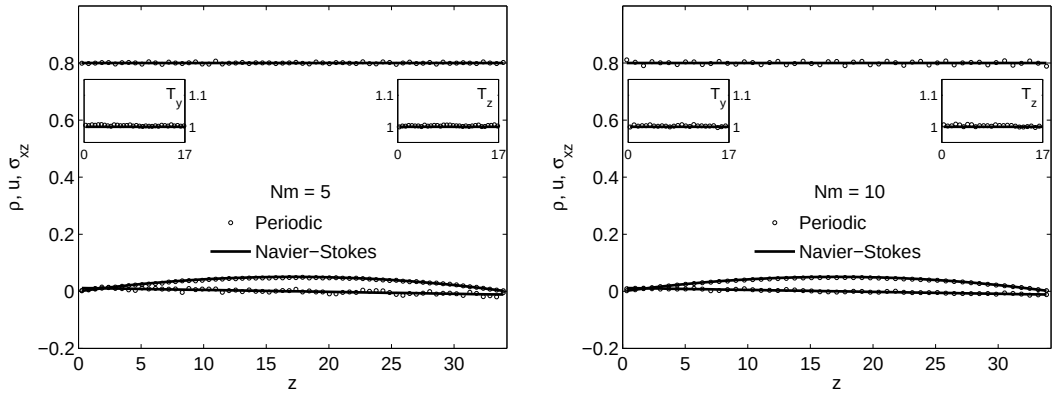

Figure 7.11: Density, velocity, temperature and stress profiles in Poiseuille flow obtained using the periodic boundary condition for different levels of coarse-graining with the body force decreased by 90%. The results are shown in MD units.

the domain size in the spanwise y direction which becomes relatively small for high N_m (see table 7.1). To this end, we first repeat the simulations in a larger domain by increasing the spanwise dimension by four times, i.e. from 8.55σ to 34.2σ. The results are essentially the same as in the small domain (see figure 7.10), and therefore we eliminate the spanwise size of the domain as a reason for the deviation of simulation results for large N_m from the incompressible Poiseuille flow solution. Next, we repeat the simulations with the body force decreased by 90%, i.e., $F = 0.00085m\sigma/\tau^2$. In this case the predicted Mach number is less than 0.15 (up to $N_m \leq 20$) and the simulation results (figure 7.11) are in agreement with the incompressible Poiseuille flow for $N_m \leq 10$, that is, we almost double the limit above which deviations occur by suppressing compressibility effects. This illustrates one of the limits of the coarse-graining procedure: due to the specific scaling of the DPD units for large values of N_m the Mach number may become large and, hence, compressibility effects cause deviations from the incompressible continuum solutions.

We further coarse-grain the system keeping the body force small so that the Mach number is kept less than 0.15 in the considered range of N_m values. For $N_m > 10$, in both the small and enlarged domains, large increases in temperature and relatively small deviations from the parabolic velocity profile are observed (figure 7.12). These effects are likely caused by partial solidification of the DPD system even though

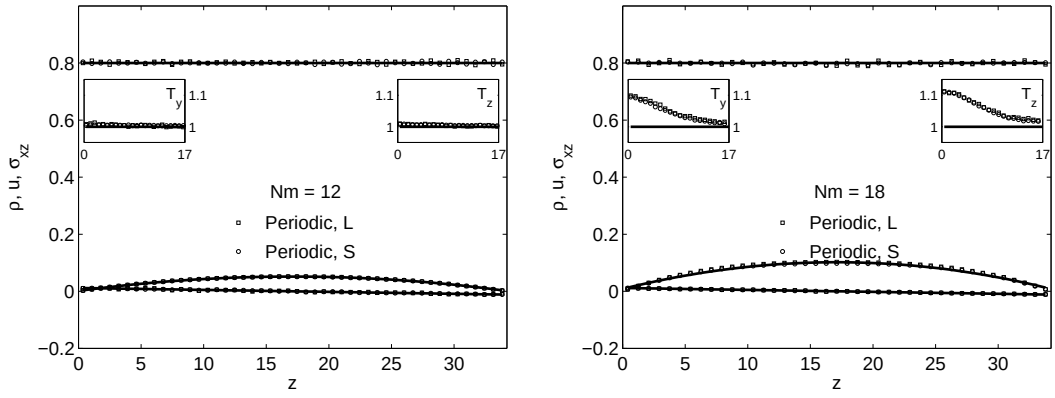

Figure 7.12: Periodic Poiseuille method, large(L) vs small(S) domain. Density, velocity, temperature and stress.

the diffusion coefficient remains approximately constant as a result of shearing (see figure 7.13) in contrast to the open system; no specific crystal structure is observed as we coarse-grain the system for $N_m \leq 20$.

As we have already seen for open systems, the DPD fluid solidifies at high levels of coarse-graining as a result of relatively large magnitude of the conservative force. In addition, the DPD unit of length R_c is proportional to $N_m^{1/3}$, i.e., it increases with N_m. Correspondingly, the size of the computational domain in DPD units decreases, as shown in table 7.1, in order to maintain constant density. Such a geometric constraint may affect the results when shear is imposed through the aforementioned PPFM approach or by explicitly imposing the wall no-slip condition. In the absence of the body force, i.e. in equilibrium simulations in the small *periodic* domain, the system behavior also changes with N_m. In figure 7.13 we plot the computed diffusion coefficient D for $N_m \leq 20$. There is a sudden drop of D at $N_m = 20$ due to formation of a crystal structure inside the domain. The crystal structure shown in figure 7.14 formed after a long-term time-integration, i.e., approximately $200,000$ simulation steps. A lattice is clearly present, however, it is difficult to distinguish between possible packing structures from simply visualizing the locations of the DPD particles inside the domain. It is possible, however, to compute the radial distribution function of the crystalized system. The resulting $g(r)$ shown in figure 7.15 suggests the presence of a sc lattice in contrast with our initial assumption about the lattice structure in

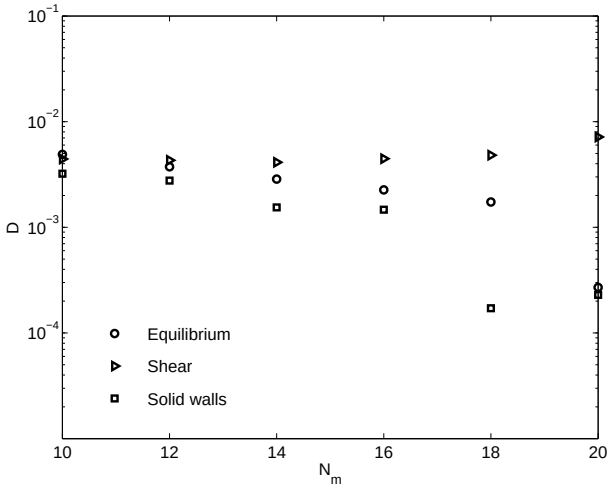

Figure 7.13: Diffusion coefficient (DPD units) for different N_m measured in a small domain with periodic walls and with solid walls in Poiseuille flow. For comparison the diffusion coefficient at zero flow (equilibrium) is also shown.

section 7.3. This is probably caused by the layering of the DPD particles imposed by the geometry as only three layers of particles fit across the domain in the y direction. In general, the calculated values of RDF are reliable only for distances less than half size of the domain, which in this case is about $1.01R_c$.

Now we report results based on DPD simulations with the second type of boundary conditions, i.e. the solid walls, which tend to induce density fluctuations close to the wall. These fluctuations become larger when the conservative force parameter a increases as we coarse-grain the system. In chapter 6 it was found that density fluctuations can affect the simulation results for N_m as low as 5. The solid-wall induced layering of DPD particles close to the walls is observed as we coarse-grain the system starting from low levels of N_m. This facilitates the structuring of the DPD fluid and in equilibrium simulations, similar to the aforementioned ones, crystallization occurs at $N_m = 18$. The dependence of the diffusion coefficient D on N_m is presented in figure 7.13; we observe a sudden drop in D at $N_m = 18$ for this case.

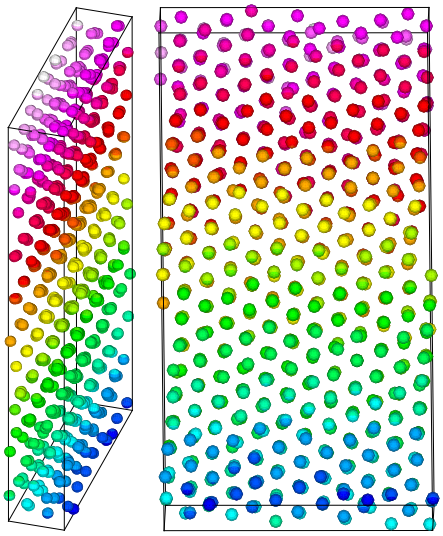

Figure 7.14: Crystal structure formed in a small domain for $N_m = 20$.

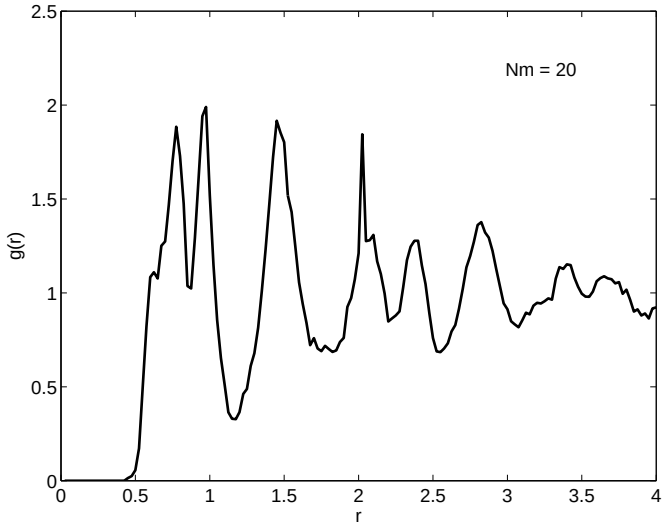

Figure 7.15: RDF for crystal structure formed in a small domain for $N_m = 20$.

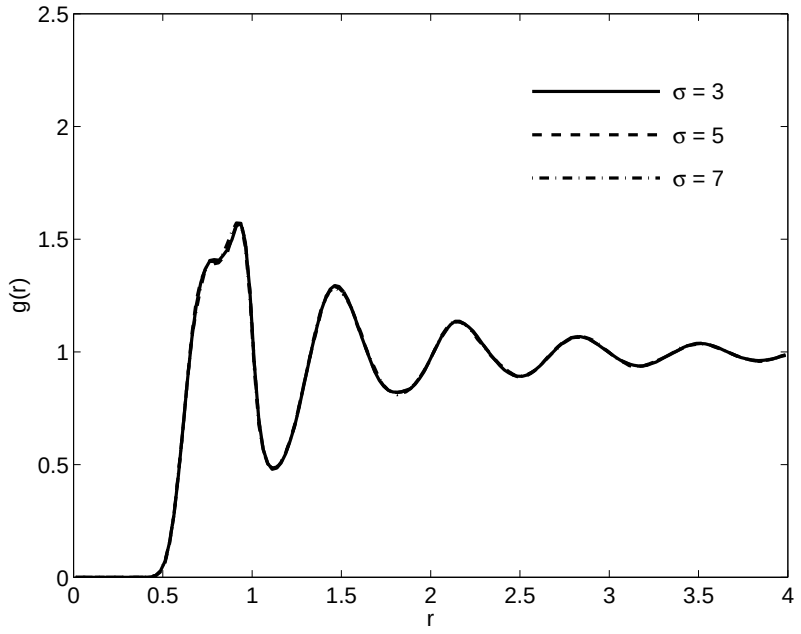

Figure 7.16: Radial distribution functions for $N_m = 20$ computed in a large periodic domain with different values of σ_R.

7.5 Effect of Thermostats

So far we have examined effects of coarse-graining due to the conservative coefficient, the Mach number and the geometric confinement. Next, we discuss how these results change if the basic DPD thermostat, consisting of the pair of dissipative and random forces, changes. We also obtain results with the alternative DPD-Lowe method.

First, we investigate the effects of random force coefficient σ_R on the DPD coarse-graining limits. To this end, we perform equilibrium simulations in a fully periodic domain of size $(10R_c)^3$ with $N_m = 20$ and $\sigma_R = 3, 5, 7$. (For $\sigma_R = 5$ and 7 the timestep is decreased from 0.02 to 0.01 and 0.005 respectively, to achieve stable simulations with temperature $k_BT = 0.1$.) In figure 7.16 we show the radial distribution functions for the simulated cases. The computed RDFs are almost identical, thus the choice of σ_R does not seem to affect the structure of the DPD fluid. Similarly, the speed of sound remains constant as σ_R varies; also the volume of the domain, and thus the geometric confinement, is independent of σ_R.

In order to also consider the effect of temperature on the DPD fluid structure,

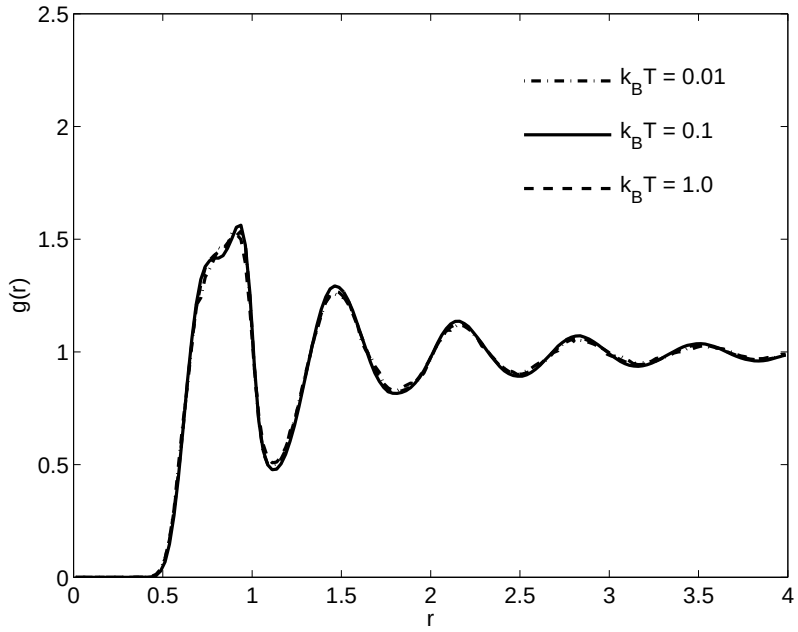

Figure 7.17: Radial distribution functions for $N_m = 20$ computed in a large periodic domain with different values of k_BT.

we performed simulations at different temperature levels in the same fully periodic domain of size $(10R_c)^3$. A DPD fluid was simulated with $N_m = 20$. The simulations were repeated with fixed $\sigma_R = 3$ and $\gamma = 450$, 45 and 4.5 with corresponding temperature levels at $k_BT = 0.01$, 0.1 and 1.0, respectively. (In the simulations with $k_BT = 0.01$ the timestep is decreased to 0.002.) We found that the computed RDFs (see figure 7.17) are unaffected by the temperature chosen in the considered range.

Finally, we considered the DPD-Lowe [41] method with the alternative Andersen type thermostat that can be tuned by employing different values of the thermalization parameter Γ. Equilibrium simulations were carried out in a periodic domain of size $(10R_c)^3$ at $k_BT = 0.1$. The time step was set to 0.02 in DPD units and the system was simulated for $12,000$ time steps with the statistics collected over the last $2,000$ steps. We simulated two extreme cases where the percent of DPD particles being thermalized at each time step is 1% and 100% for $\Gamma = 0.5$ and 50, respectively. Here too, we observed that the computed RDFs for different levels of coarse-graining are the same for both values of Γ and are almost identical to those obtained from the aforementioned DPD-Verlet method simulations (see figure 7.18). This suggests that

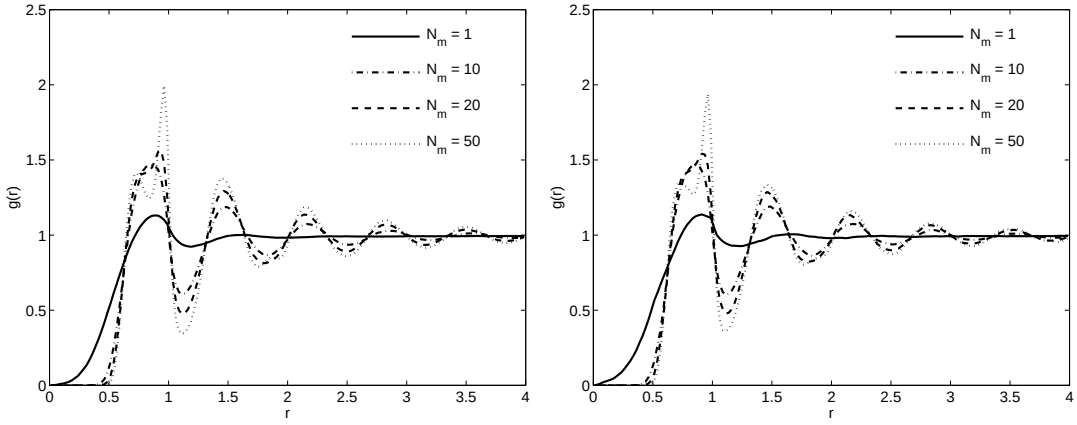

Figure 7.18: Radial distribution functions computed in a large periodic domain for different N_m. Lowe thermostat, time step $\Delta t = 0.02$. Left: $\Gamma = 0.5$. Right: $\Gamma = 50$.

the structure of the DPD fluid simulated with the Andersen thermostat is the same to the one obtained with the standard DPD thermostat. Therefore, we expect both fluids to solidify at the same level of coarse-graining in equilibrium conditions, which is indeed the case as we have verified with DPD-Lowe simulations.

There is a significant difference, however, of the DPD-Lowe method with the standard DPD-Verlet method in non-equilibrium simulations as the former yields fluids with much larger viscosity. We computed the dynamic viscosity using the periodic Poiseuille flow method [3] described in section 7.4. Three values of Γ were used in the simulations, $\Gamma = 0.5$, 25 and 50. The calculated values of the dynamic viscosity for different N_m are plotted in figure 7.1 along with the DPD-Verlet fluid viscosity.

We note that the dynamic viscosity in all cases is higher than the one in DPD-Verlet simulations. Therefore, the DPD unit of force is expected to be larger in Lowe than in Verlet simulations. Consequently, the predicted Mach number for all levels of coarse-graining of the Poiseuille system are in the supersonic regime for $\Gamma = 25$ and 50! Thus, for Γ between 0.5 and 50 compressibility effects are expected to be significantly more pronounced with the DPD-Lowe thermostat than with the DPD-Verlet thermostat. Finally, we note that the DPD unit of length does not depend on the choice of thermostat and therefore the geometric constraints in simulations are the same for both methods.

7.6 Summary

We have considered liquid-state systems both in equilibrium and in Poiseuille flow in order to investigate the fluid states as a function of the coarse-graining parameter N_m that expresses how many atoms are packed in a DPD particle. So far the majority of published work has considered $N_m = 1$ in applications although the original developers of DPD advocated coarse-grained versions with $N_m > 1$, see [15, 24, 31]. In the current work we identified fundamental and practical limits of coarse-graining in DPD due to the following three factors:

- Solidification of the DPD liquid due to the increase in the magnitude of the conservative force.
- Compressibility effects due to the increase of the Mach number in non-equilibrium simulations.
- Geometry constraints due to the decrease of size of the computational domain.

The minimum value of N_m set by these limits determines the maximum level of coarse-graining and it depends on the particular system being simulated. In addition, we investigated the effects of thermostats and observed that the fluid structure remains basically the same irrespective of the thermostat, i.e. artificial crystallization is often observed above $N_m > 20$. We also note that the artifacts reported in the current chapter are different than the well-known artifacts attributed to large time steps in the DPD simulations as has been reported in previous works, e.g. see [34].

Chapter 8

Adaptive Boundary Conditions in DPD

8.1 Introduction

Dissipative Particle Dynamics simulations of wall-bounded flows exhibit density fluctuations that depend strongly on the no-slip boundary condition and increase with the level of coarse-graining. These fluctuations may be physical and thus desirable but in other applications may be erroneous. In this chapter we develop an adaptive model for wall-particle interactions that eliminates such oscillations and can target prescribed density profiles.

A typical density profile for a Lennard-Jones fluid with $\kappa^{-1} = 15.36$ is shown in figure 8.1. We simulate Poiseuille flow and details of the DPD and corresponding MD simulations can be found in chapter 6. The density fluctuations for MD and DPD corresponding to $N_m = 1$ are similar, with the main difference being the large values of the DPD density at the wall. As N_m increases, the density fluctuations in the DPD simulations also increase, with the $N_m = 5$ case exhibiting very large values at the wall and also inside the flow domain. This is not a desired effect, because we expect the fluctuations to decrease as we approach the continuum, i.e. $N_m \to \infty$. We present next a new model that implements the no-slip boundary condition in DPD while at the same time can target a prescribed density profile, i.e. flat or oscillatory.

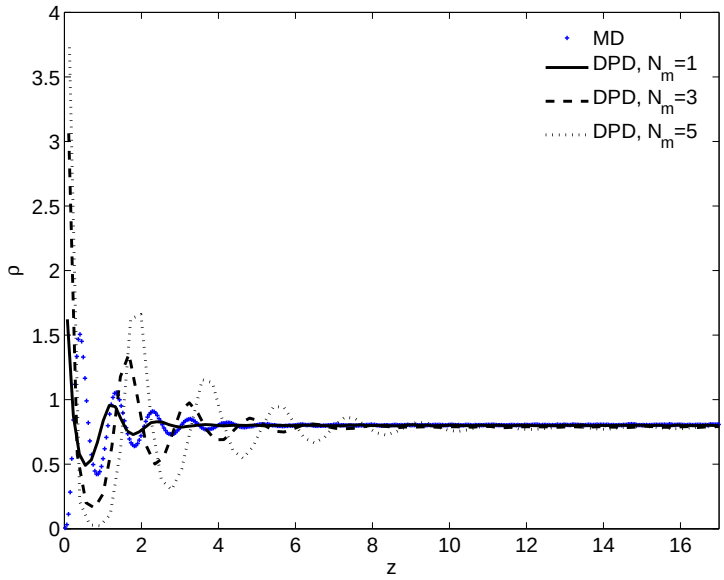

Figure 8.1: Density profiles for Poiseuille flow. The domain extends from one wall to the centerline of the channel.

8.2 Adaptive Boundary Conditions

Let us consider a wall perpendicular to the z-axis and located at $z = 0$. The wall is moving with the velocity $\vec{V}_W$ remaining in $z = 0$ plane. On each particle within specified distance from the wall we apply a force $\vec{F}^W$ directed perpendicular to the wall, positive in the direction pointing normal into the fluid region. The magnitude of the force $\vec{F}^W$ depends on the distance from the wall and is iteratively re-computed based on the estimated density fluctuations as described next. We consider a subregion of the computational domain of width L adjacent to the wall and divide it into bins of size h (see figure 8.2). In general, L should be greater or equal to the cutoff radius R_c. The value of h can be chosen based on the desired resolution of the simulation results. The total number of bins is then $N_b = L/h$, and we number them in increasing order away from the wall, so that the bin adjacent to the wall has index $i_b = 1$, and the furthest bin from the wall has index N_b. During the simulations in each bin i_b the time-averaged density $\rho_s(i_b)$ is collected over a specified number of time-steps N_{av}. Next, the values of ρ_s are locally averaged over (up) to n_{av} bins and compared to desired density values ρ_d averaged over the same bins. Specifically, for the bin i_b the

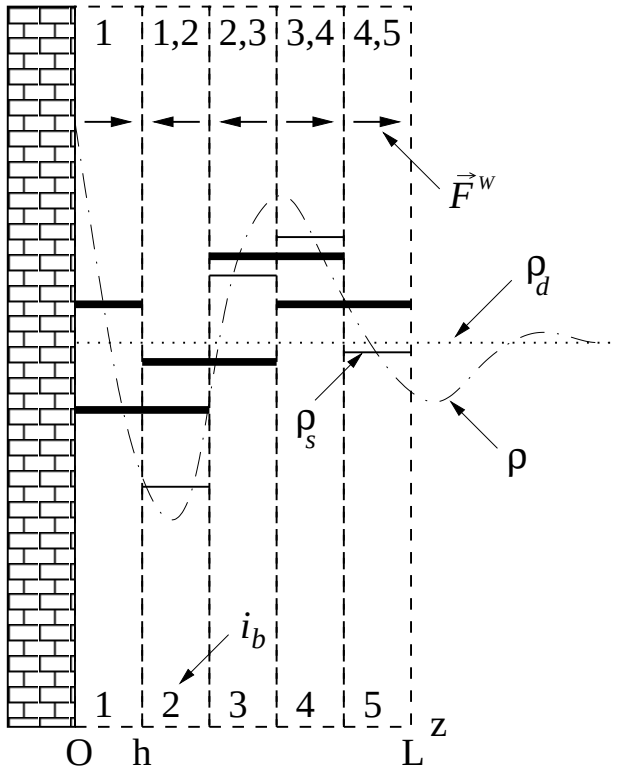

Figure 8.2: Sketch illustrating the concept of adaptive boundary condition (ABC). The sketch corresponds to the case with parameters $n_{av} = 2$ and $N_b = 5$ (defined in the text). The bins are shown with dashed lines. The bin indices i_b are shown in a lower part of the bins. The desired (uniform in this case) density level ρ_d is shown with a dotted line. The DPD density profile ρ is shown with a dash-dotted line. The time averaged density levels ρ_s in the bins are shown with thin solid lines. The locally averaged density levels are shown with thick solid lines. The densities are averaged over the bins with indices from $i_a = \max(i_b - n_{av} + 1, 1)$ to i_b. These indices are listed in the upper part of the bins. If locally averaged density is higher than desired density the force from the wall $\vec{F}^W(i_b)$ is increased (shown with the arrow pointing away from the wall). If the averaged density is lower, the force is decreased (shown with the arrow pointing towards the wall).

densities are averaged over the bins with indices from $i_a = \max(i_b - n_{av} + 1, 1)$ to i_b. The values of i_a for different bin indices for specific value of $n_{av} = 3$ used later in this chapter are: (i_b,i_a): (1,1);(2,1);(3,1);(4,2);(5,3); etc. The case with $n_{av} = 2$ is illustrated in figure 8.2. The force $\vec{F}^W(i_b)$ acting on the particles in bin i_b is then updated according to

$$\vec{F}^W(i_b) = \vec{F}^W(i_b) + C_W \left(\frac{\sum_{i=i_a}^{i_b} \rho_s(i)}{\sum_{i=i_a}^{i_b} \rho_d(i)} - 1 \right), \tag{8.1}$$

where C_W is a positive constant of order one. After the force is updated, new values of ρ_s are computed and the iterative process continues. The wall force $\vec{F}^W$ is added to the particles within distance L from the wall at each time-integration step.

The random and dissipative force contributions from the wall are computed in a way similar to [76]. We describe the procedure next.

Let us assume that there are N_W particles within distance L from the wall. The i-th particle has coordinates x_i, y_i, z_i and velocity $\vec{v}_i$. The total force acting on particle i located inside the bin i_b is $\vec{F}_i = \vec{F}^W(i_b) + \Sigma_{j \neq i}(\vec{F}^C_{ij} + \vec{F}^D_{ij} + \Delta t^{-1/2} \vec{F}^R_{ij})$. It is convenient to introduce a ghost particle g, although it is not necessary to construct it explicitly in the simulations. The force contribution of the wall boundary conditions at each time step is expressed using the following pseudo-code.

for particle $i = 1, .., N_W$
  find bin i_b in which particle i is located
  $\vec{F}_i = \vec{F}_i + \vec{F}^W(i_b)$
  create ghost particle g with $x_g = x_i + \xi_x$, $y_g = y_i + \xi_y$, $z_g = -z_i$ and $\vec{v}_g = 2\vec{V}_W - \vec{v}_i$
  for particle $j = i, .., N_W$
    compute $\vec{F}^R_{jg}$, $\vec{F}^D_{jg}$
    $\vec{F}_j = \vec{F}_j + \vec{F}^D_{jg} + \Delta t^{-1/2} \vec{F}^R_{jg}$
    if $i \neq j$ $\vec{F}_i = \vec{F}_i - \vec{F}^D_{jg} - \Delta t^{-1/2} \vec{F}^R_{jg}$
  end
end

Variables ξ_x and ξ_y take uniformly random values from the interval $[-R_c, R_c]$.

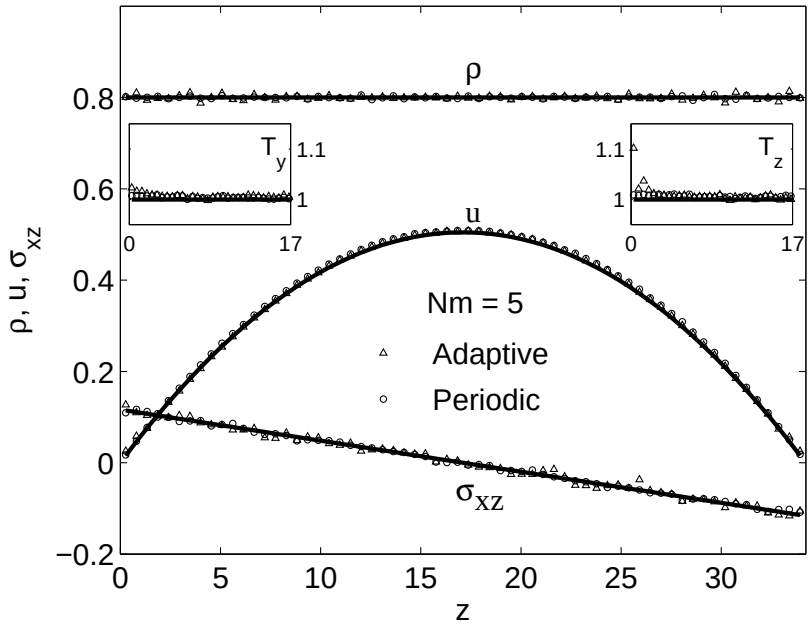

Figure 8.3: Comparison of density, velocity, temperature and stress profiles for Poiseuille flow corresponding to adaptive and periodic boundary conditions ($N_m = 5$). The incompressible Navier-Stokes solution is shown with lines.

In addition, when fluid particles penetrate into the wall region we perform a bounce-back reflection of these particles. Typically, we start the simulations with the wall force $\vec{F}^W = 0$ in all bins. We let the DPD fluid equilibrate for a short time (about 1000 steps). As a result large density fluctuations form next to the wall. Next, we apply the adaptive procedure described above. Once the desired density fluctuations are obtained, we collect statistical data from the simulations. We will refer to this procedure as adaptive boundary conditions or ABC.

8.3 Simulation Results

To evaluate the performance of the proposed model, we have simulated Poiseuille flow using both the periodic Poiseuille flow method(PPFM) [3] and adaptive (ABC) techniques at different levels of coarse-graining $N_m \leq 5$. The fluid we consider is governed by a modified Lennard-Jones potential with density $\rho_{MD} = 0.8\sigma^{-3}$ and occupies a volume of $34.2\sigma \times 8.55\sigma \times 34.2\sigma$; here σ is the atomic diameter in MD. The

dimensionless compressibility of the fluid is $\kappa^{-1} = 15.36$ (see chapter 6). The DPD fluid density ρ_{DPD} is chosen to be $3R_c^{-3}$. The viscosity of DPD fluid for each value of coarse-graining parameter N_m can be computed using the Lees-Edwards method [38]. The values of the dynamic viscosity μ for different levels of coarse-graining are: $(N_m, \mu) : (1, 1.04); (2, 1.31); (3, 1.55); (4, 1.82); (5, 2.15)$. The random ($\sigma_R = 3$) and dissipative ($\gamma = 45$) force coefficients are used in the DPD integration scheme (a modified velocity Verlet method with $\lambda = 0.5$, [24]), timestep $\Delta t = 0.02$ and temperature $k_B T = 0.1$, all in DPD units. All plots, except for the temperature which is normalized by the equilibrium temperature $k_B T = 0.1$, are in reduced MD units in this chapter.

In the PPFM simulations the domain was doubled in the z direction and the body force $F = 0.0085$ was applied in the x direction. The simulations were run for $410,000$ timesteps and the domain was subdivided in the z direction into equal bins of size $0.2R_c$, with the data collected over the last $40,000$ steps. The simulation results for $N_m = 5$ are plotted in figure 8.3. The DPD density, x-velocity, shear stress and partial temperatures averaged over both halves of the computational domain are shown. The agreement with incompressible Navier-Stokes solution for Poiseuille flow is good for $N_m \leq 5$. For larger values of N_m we observed deviations and above $N_m = 20$ an apparent solidification process is in place.

In the ABC simulations we integrated the DPD equations for $1,000,000$ timesteps and the statistical data were averaged over the last $40,000$ time steps. A uniform density profile ρ_d was imposed at $\rho_{DPD} = 3R_c^{-3}$. Also, we used $L = 1R_c$, $h = 0.2R_c$, $n_{av} = 3$ and $C_W = 1$; the local density values were averaged over $N_{av} = 500$ timesteps. Typically, about 50 wall force adjustments in simulations were enough to obtain desired density values close to the wall (figure 8.4). In figure 8.5 the magnitudes of density fluctuations across the channel are plotted for the first 100 interactions for one of the simulation cases. Statistical fluctuations obtained through density averaging in the bins of the same size and over the same number of steps for the periodic Poiseuille flow method are shown for comparison. The simulation results are shown in figure 8.3 for $N_m = 5$; for $N_m < 5$ similar results were obtained. In general, they are in a good

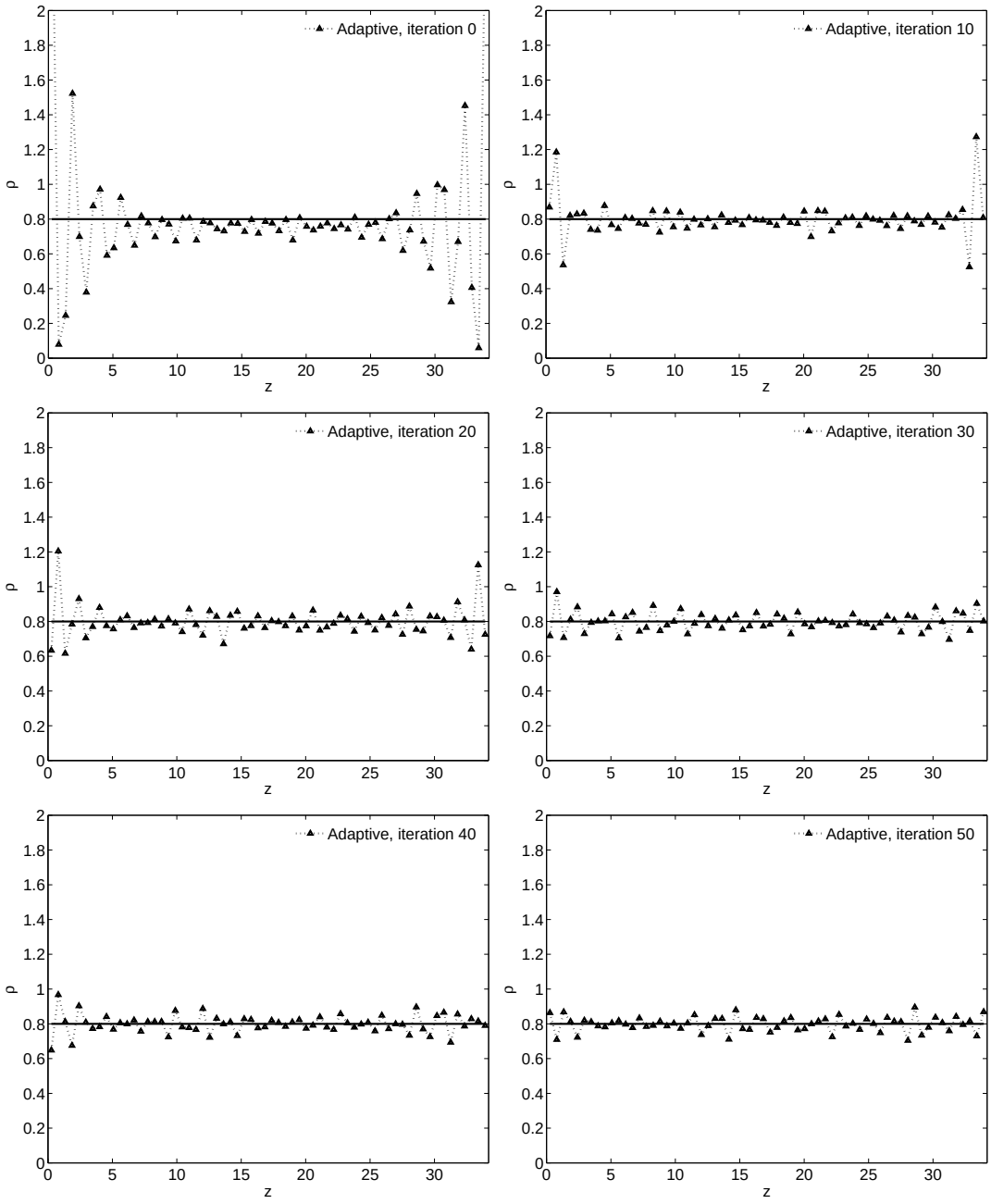

Figure 8.4: Evolution of density fluctuation versus force-iterations in simulations ($N_m = 5$) with adaptive boundary condition.

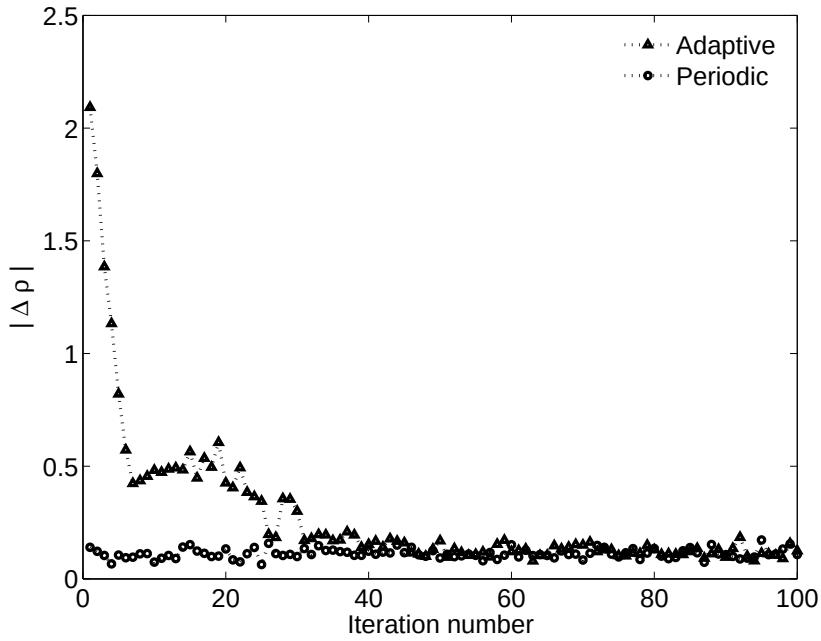

Figure 8.5: Maximum density fluctuation versus force-iterations in simulations ($N_m = 5$) with adaptive boundary condition. Statistical fluctuations obtained through density averaging in the bins of the same size and over the same number of steps for the periodic Poiseuille flow method are shown for comparison.

agreement with those obtained from the PPFM method, although there is a difference in the temperature profile close to the wall.

The reason for an increase of partial temperature in the normal to the wall direction is the wall force $\vec{F}^W$. In simulations presented here, an average increase of partial temperature in the z direction was about 11% while the total temperature increase was about 4%. It is possible to affect the temperature close to the wall by modifying the dissipative force coefficient γ of DPD particles. The procedure we apply for adjusting the temperature is similar to one used for the density. Specifically, the coefficient γ of particles in the bin close to the wall is increased if the temperature is above the desired level in that bin or decreased otherwise. This can effectively control the total temperature, however the difference between the partial temperatures in normal and parallel to the wall directions remains about the same. For example, for the case considered here with $N_m = 5$ the average increase of partial temperature dropped by 3-4% and the total temperature was within 2% of $0.1k_BT$ (figure 8.6).

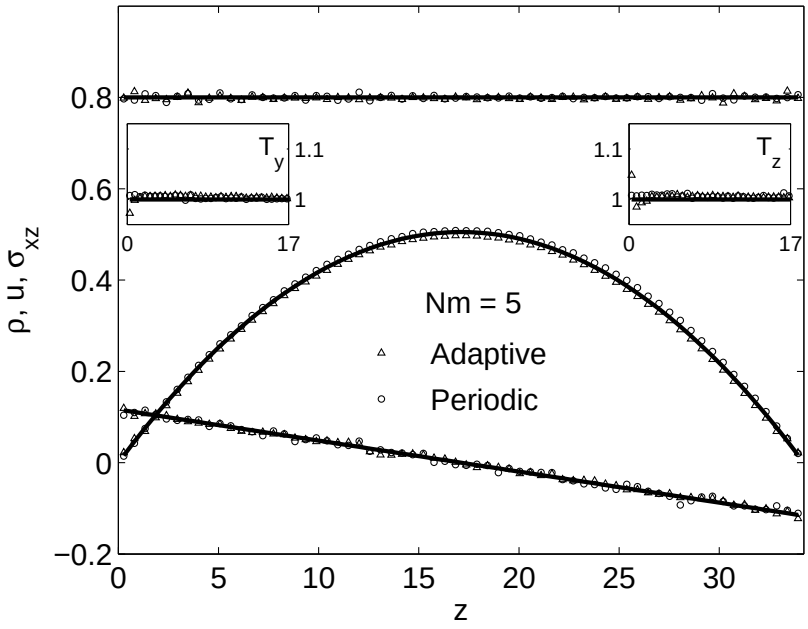

Figure 8.6: Density, velocity, temperature and stress profiles for Poiseuille flow for adaptive boundary conditions ($N_m = 5$). The temperature close to the wall is controlled by modifying the dissipative force coefficient of DPD particles. The incompressible Navier-Stokes solution is shown with lines.

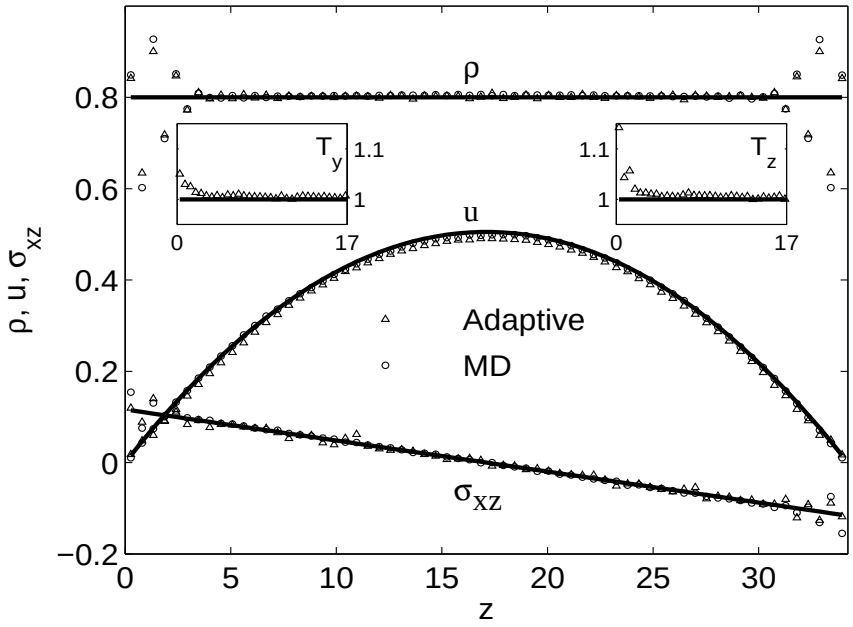

Figure 8.7: Comparison of density, velocity, temperature and stress profiles for Poiseuille flow corresponding to adaptive boundary conditions and coarse-grained MD results ($N_m = 5$).

Finally, we demonstrate that the ABC approach can be employed to target specific density fluctuations close to the solid wall. Here, for illustration purposes, we present a case, where the density fluctuations imposed by boundary conditions in DPD correspond to the coarse-grained MD density fluctuations. Specifically, the coarse-grained density fluctuations close to the wall are obtained from MD simulations by averaging them in bins of size $0.2R_c$, where the value of DPD unit of length R_c corresponds to $N_m = 5$, see equation (6.5). The fluctuations are significant within distance of $2R_c$ from the wall and therefore we chose $L = 2R_c$ in the ABC method. In addition, we set $h = 0.2R_c$, $N_{av} = 500$, $n_{av} = 3$ and $C_W = 1$. The desired level for density fluctuations ρ_d in each bin is set based on coarse-grained MD data. In figure 8.7 we plot the MD and DPD simulation results. In general, the density, velocity and stress profiles are in good agreement, although the DPD temperature is increased close to the wall due the aforementioned reasons.

8.4 Summary

In this chapter we have developed an adaptive model for wall-particle interactions that allows to target the desired density profile close to the wall, while at the same time keeping the no-slip boundary condition. We note here that the method is general and not limited to dissipative particle dynamics. We believe it can be used in molecular dynamics (MD) and Monte-Carlo (MC) simulations in various fields but also in the lattice Boltzmann method (LBM) and in smooth particle hydrodynamics (SPH).

Chapter 9

Simulation of Flows Around Solid Spheres using DPD

9.1 Introduction

Suspensions of small particles such as colloids, food products, paints and physiological systems (including blood) are common to many industrial and natural processes. The properties of such suspensions are often determined by their mesoscale structure and mesoscopic computer simulation methods offer a powerful alternative to the experiments. In this chapter we use the Dissipative Particle Dynamics method to model flows around solid spherical particles. Several approaches for simulating rigid particles are presented and evaluated. The simulation results are compared with analytic predictions, experimental observations and other simulation results. All parameters are in DPD units.

9.2 Models for Simulating Spherical Particles

Several types of models for simulating spherical particles in DPD can be found in literature. In [75] the solid spheres are modeled as a structureless objects. There, the fluid particles interact with the surface of the sphere instead of its center. The advantage of this method is that each sphere can be represented with just one particle.

The disadvantage is that it is difficult to extend the method to the objects of arbitrary shape. Another commonly used approach for modeling solid objects is to group and "freeze" collections of DPD particles. The particles can be grouped in a specific way to reduce the roughness of the surface as in [11], or simply be a subset of the initial lattice, which is typically of fcc or sc type [7, 42]. In simulations the motion of these DPD particles is constrained so that their relative positions remain the same. It was observed that for finite Reynolds number flows around solid objects constructed this way the fluid particles can penetrate the objects. This can affect the accuracy of DPD calculations, and hence the reflection boundary conditions sometimes are added [37]. In this chapter we consider four models for simulating solid spheres, two of them are based on the ideas developed in chapters 5 and 8.

In the first model the spherical particle is created by grouping the subset of the initial DPD particle lattice. We will refer to this model as model "A" in the following sections.

Model "B" is a combination of model "A" with a bounce-back reflection at the surface of the sphere.

An extension of the solid wall boundary conditions described in chapter 5 will be referred to as model "C". In this model, the DPD particles inside the sphere are distributed in layers, in combination with bounce-back reflection at the surface of the sphere. In addition, the conservative force coefficient of DPD particles inside the sphere is adjusted using equation (5.3). The density of the sphere, ρ_s, is chosen to be equal to the fluid density, ρ_f. The layers are formed starting from the outer layer which is located on the surface of the sphere. The density of the particles in this layer is equal to $\rho_s^{2/3}$. Other layers are formed within distance $\rho_s^{-1/3}$ of each other and fill the inner part of the sphere. Each new layer has density equal to $\rho_s^{2/3}$ or less if there are not enough particles to fill in the layer completely. The number of layers depends on the sphere radius and the volume density of the sphere. For example, the sphere of radius $A = 3$ and density $\rho_s = 3$ consists of 2 layers. The outer layer has 235 particles while the inner layer - 104 particles. To achieve uniform distribution of the DPD particles in each layer the following procedure is used. Initially, the particles

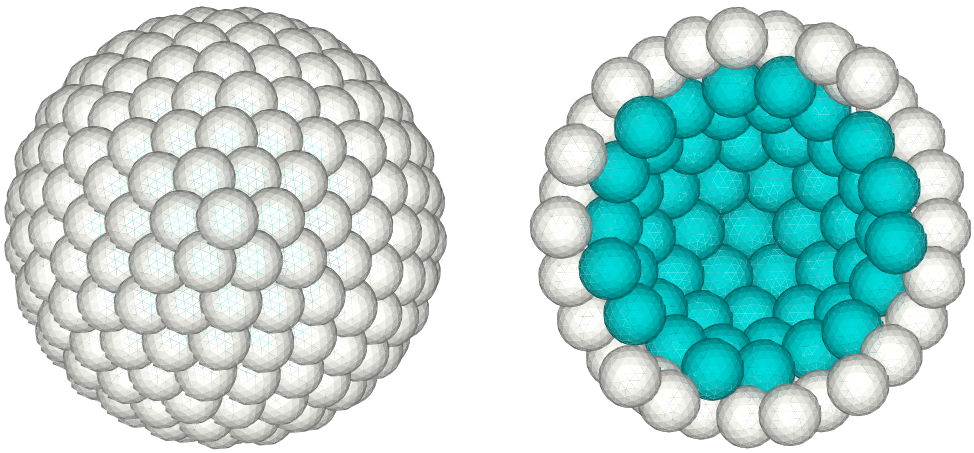

Figure 9.1: DPD particle distribution inside the sphere of radius $A = 3$ and density $\rho_s = 3$. The sphere consists of 2 layers of particles. The outer layer has 235 particles while the inner layer - 104. The particles are distributed uniformly in each layer to reduce the roughness of the sphere surface.

are placed randomly inside the layer. Then, the pairwise repulsive force proportional to the inverse of the inter-particle distance is added to all particles. The positions of the particles are iteratively updated to minimize the energy of the system. During this process the positions of the particles are constrained to the corresponding layers. The final distribution of the particles inside the sphere of radius $A = 3$ and density $\rho_s = 3$ is shown in figure 9.1. The sphere has a smooth surface, however due to the uneven distribution of the DPD particles inside the volume, the moments of inertia are different from the moments for a sphere with uniform density. In some applications this may be important.

Model "D" is based on the adaptive boundary conditions developed in chapter 8. The sphere is again constructed from layers of DPD particles in combination with bounce back reflection at the surface of the sphere. The conservative force coefficient of the DPD particles inside the sphere is set to zero and an adaptive force acting on the fluid particles in the radial direction is added to minimize density fluctuations close to the surface of the sphere. For low Reynolds number flows this model can produce almost uniform density profile close to the sphere.

9.3 Flow over simple cubic array of spheres

In this section fluid flow past a periodic array of spheres is considered. Simulation domain is a cube, periodic in all directions. A single sphere is placed in the center of the domain; periodic images of the sphere form a simple cubic lattice in three dimensional space. An external force F_{ext} is applied to the fluid in x direction, while the position of the sphere is fixed in space. The volume of simulation domain Ω is subdivided into the volume occupied by the fluid, Ω_f, and the volume occupied by the sphere, Ω_p. The superficial velocity is defined as

$$\bar{u} = \frac{1}{\Omega} \int_{\Omega_f} \vec{u}(x)\ d^3x, \tag{9.1}$$

where $\vec{u}(x)$ is a fluid velocity. It can be shown that sedimentation velocity of an array of objects under the action of a body force is equal to the superficial velocity [14].

In 1959 Hasimoto [29] calculated the drag force on the dilute arrays of spheres from the fundamental periodic solutions of the Stokes equations. For a simple cubic array of spheres the drag force normalized by the Stokes drag is given by

$$F^{-1} = 1 - 1.7601\varphi^{1/3} + \varphi - 1.5593\varphi^2 + O(\varphi^{8/3}). \tag{9.2}$$

The volume fraction φ is defined as Ω_p/Ω. In 1982 Sangani and Acrivos [60] extended Hasimoto's results to a larger volume fractions. They obtained

$$F^{-1} = 1 - 1.7601\varphi^{1/3} + \varphi - 1.5593\varphi^2 + 3.9799\varphi^{8/3} - 3.0734\varphi^{10/3}. \tag{9.3}$$

For a spherical particle the drag force coefficient is defined as

$$C_D = \frac{F_s}{\frac{1}{2}\rho_f \bar{u} \pi A^2}, \tag{9.4}$$

where F_s is a total force exerted by fluid on the sphere surface. For small particle Reynolds numbers ($Re_P < 1$) the drag coefficient can be estimated using a Stokes

drag law,

$$C_D = \frac{24}{Re_P}, \tag{9.5}$$

or with the Oseen correction,

$$C_D = \frac{24}{Re_P}(1 + \frac{3}{16}Re_P). \tag{9.6}$$

The particle Reynolds number is based on the particle diameter, the superficial velocity and kinematic viscosity of the fluid, and is defined as

$$Re_P = \frac{2A|\bar{u}|}{\nu}. \tag{9.7}$$

In the simulations we set the DPD fluid density $\rho_f = 3$. The dissipative and random force coefficients are $\gamma = 4.5$ and $\sigma_R = 3$. The conservative force coefficient is set to $a = 25$. The modified velocity Verlet method [24] with parameter $\lambda = 0.5$ and time step 0.02 is used for time integration. The cubic domain of size L is periodic in all directions. The sphere of radius A is placed in the center of the domain. The solid volume fraction is defined as

$$\varphi = \frac{4/3\pi A^3}{L^3}. \tag{9.8}$$

By varying sphere radius or the size of the computational domain different volume fractions can be obtained. The flow is driven by an external force, F_{ext}, applied to the DPD fluid particles in x direction. In all cases the simulations are run for more than 1000000 time steps. The results are averaged over at least 750000 time steps.

We start from considering the case with the sphere radius $A = 3$ and domain size $L = 18.568034$. The solid volume fraction of this system is equal to $\varphi = 0.01325$. The force F_{ext} in a range from 0.00005 to 0.5 is applied to generate the flow. The superficial velocity $\bar{u}$ is computed from the velocities of the fluid particles. Given the force exerted by fluid on the sphere, F_s, and fluid superficial velocity, $\bar{u}$, the particle Reynolds number, Re_P, and the drag coefficient, C_D, can be calculated.

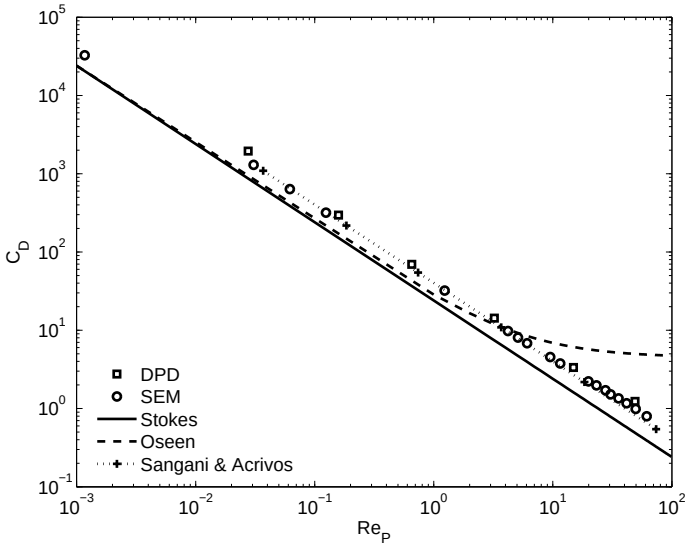

Figure 9.2: Drag coefficient C_D as a function of particle Reynolds number Re_P for the flow past solid sphere in a periodic domain. The periodic images of the sphere form a simple cubic lattice in three dimensional space. The sphere radius is $A = 3$, the solid volume fraction is $\varphi = 0.01325$. The sphere is modeled by freezing the portion of the initial DPD particle lattice (model "A").

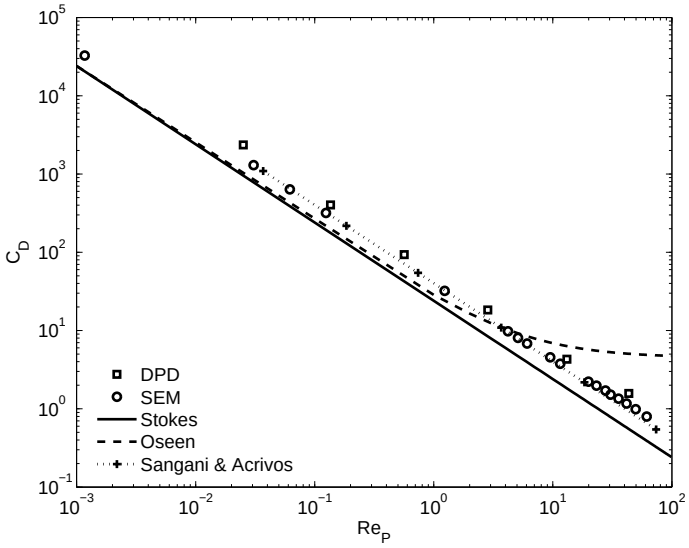

Figure 9.3: Drag coefficient C_D as a function of particle Reynolds number Re_P for the flow past solid sphere in a periodic domain. The periodic images of the sphere form a simple cubic lattice in three dimensional space. The sphere radius is $A = 3$, the solid volume fraction is $\varphi = 0.01325$. The sphere is modeled by freezing the portion of the initial DPD particle lattice in combination with bounce back reflection at the solid-fluid interface (model "B").

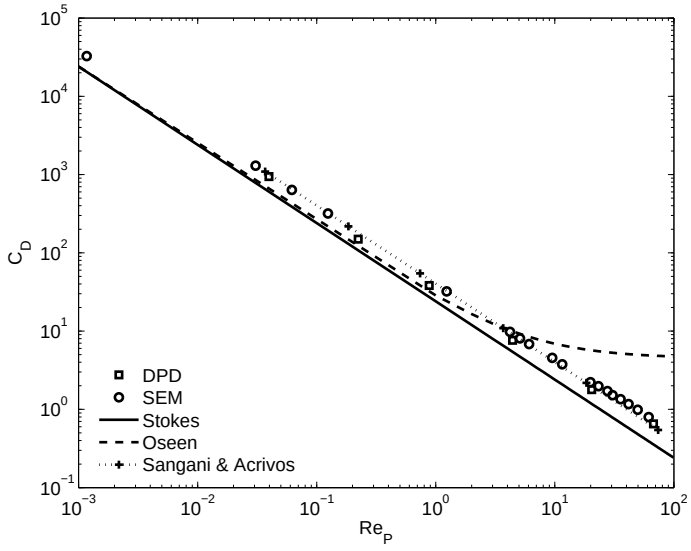

Figure 9.4: Drag coefficient C_D as a function of particle Reynolds number Re_P for the flow past solid sphere in a periodic domain. The periodic images of the sphere form a simple cubic lattice in three dimensional space. The sphere radius is $A = 3$, the solid volume fraction is $\varphi = 0.01325$. The sphere is modeled using layers of DPD particles, in combination with bounce back reflection at the sphere surface. The conservative force coefficient of the DPD particles inside the sphere is adjusted using equation (5.3) (model "C").

In figures 9.2, 9.3, 9.4 and 9.5 we plot the drag force coefficient as a function of particle Reynolds number for sphere models "A", "B", "C" and "D", respectively. The calculated values of C_D are compared with spectral element method (SEM) simulation results obtained by Gelonia Dent at Brown University [14]. Stokes, Oseen and Sangani & Acrivos predictions are also shown in the figures. All models give acceptable results, although models "C" and "D" seem to be more accurate.

For fixed sphere radius ($A = 3$) we decrease the size of the domain to $L = 7.513251$ to obtain higher solid volume fraction $\varphi = 0.2$. The calculated drag coefficients for models "A", "B" and "C" are plotted in figures 9.6 - 9.8. In all cases, large deviations of the DPD simulation results from the spectral element method prediction obtained by Dent are observed. For a fixed sphere radius the number of DPD particles in the gaps between the spheres decreases with increasing solid volume fraction, and hence, to resolve the flow accurately for high volume fractions, large sphere radii are required in simulations. Therefore, we increase the sphere radius to $A = 8$ keeping the solid

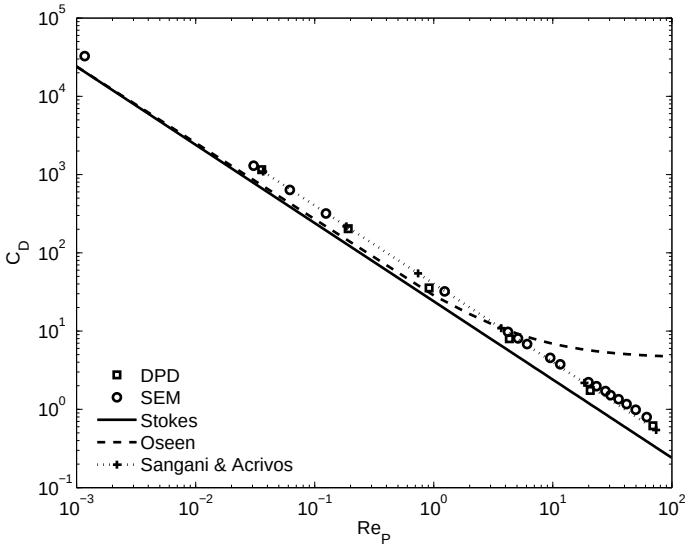

Figure 9.5: Drag coefficient C_D as a function of particle Reynolds number Re_P for the flow past solid sphere in a periodic domain. The periodic images of the sphere form a simple cubic lattice in three dimensional space. The sphere radius is $A = 3$, the solid volume fraction is $\varphi = 0.01325$. The sphere is modeled using layers of DPD particles, in combination with bounce back reflection at the sphere surface. An adaptive model for wall-particle interactions is used to obtain uniform density profile close to the sphere surface (model "D").

volume fraction constant ($\varphi = 0.2$). The simulation results are shown in figures 9.9 - 9.11. The results for model "C" can be further improved by rearranging the DPD particles inside the sphere. Specifically, the density of the particles inside each layer can be increased to match the fluid density ρ_f. The computed drag coefficient in this case is in a good agreement with spectral element simulation results (figure 9.12).

9.4 Spherical Particle Settling in a Fluid at Rest

In this section we study the motion of a solid sphere settling under gravity in a fluid at rest. The computational domain is periodic in x and y directions. The DPD fluid covers $0 \leq x \leq 249.61$, $0 \leq y \leq 48.53$, $1 \leq z \leq 172.24$ and is bounded by two walls of width 1 in z direction. The walls are modeled by freezing the DPD particles. The fluid density is equal to $\rho_f = 3$. There are about 6.5 million DPD particles in the domain. The modified velocity Verlet method with $\lambda = 0.5$ and timestep 0.02

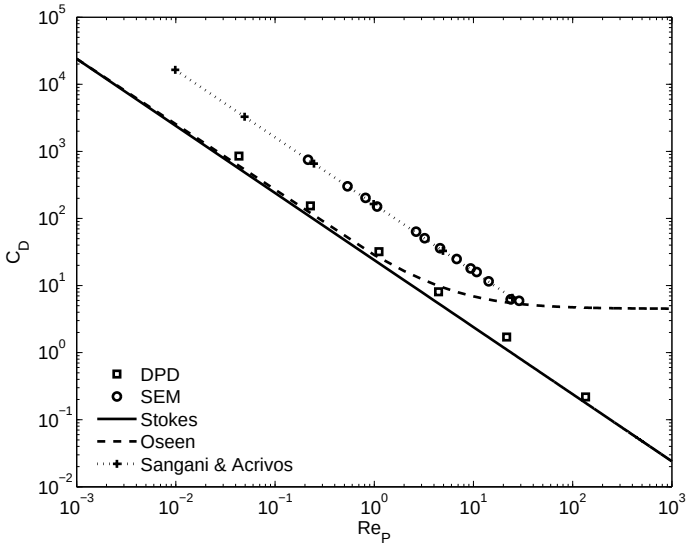

Figure 9.6: Drag coefficient C_D as a function of particle Reynolds number Re_P for the flow past solid sphere in a periodic domain. The periodic images of the sphere form a simple cubic lattice in three dimensional space. The sphere radius is $A = 3$, the solid volume fraction is $\varphi = 0.2$. The sphere is modeled by freezing the portion of the initial DPD particle lattice (model "A").

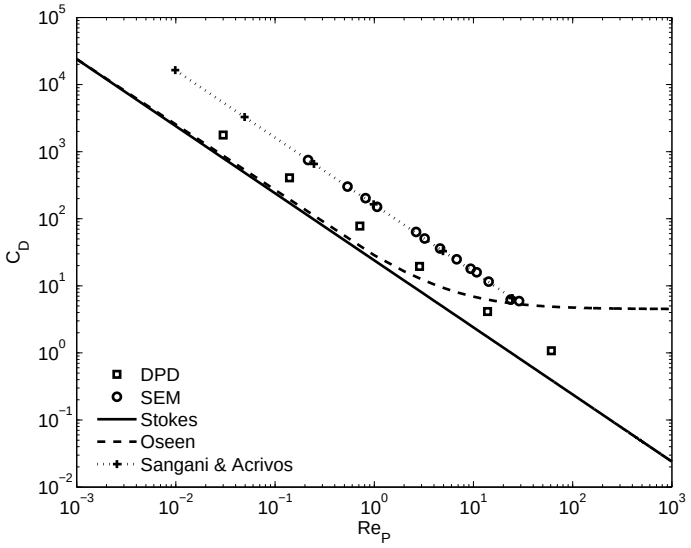

Figure 9.7: Drag coefficient C_D as a function of particle Reynolds number Re_P for the flow past solid sphere in a periodic domain. The periodic images of the sphere form a simple cubic lattice in three dimensional space. The sphere radius is $A = 3$, the solid volume fraction is $\varphi = 0.2$. The sphere is modeled by freezing the portion of the initial DPD particle lattice in combination with bounce back reflection at the solid-fluid interface (model "B").

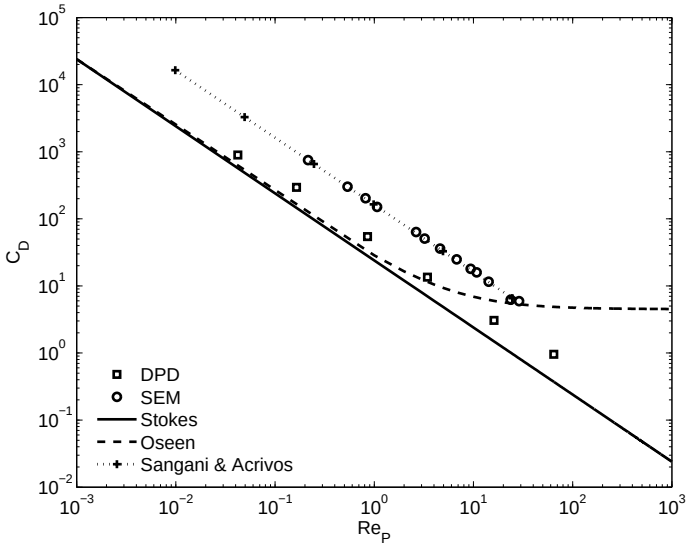

Figure 9.8: Drag coefficient C_D as a function of particle Reynolds number Re_P for the flow past solid sphere in a periodic domain. The periodic images of the sphere form a simple cubic lattice in three dimensional space. The sphere radius is $A = 3$, the solid volume fraction is $\varphi = 0.2$. The sphere is modeled using layers of DPD particles, in combination with bounce back reflection at the sphere surface. The conservative force coefficient of the DPD particles inside the sphere is adjusted using equation (5.3) (model "C").

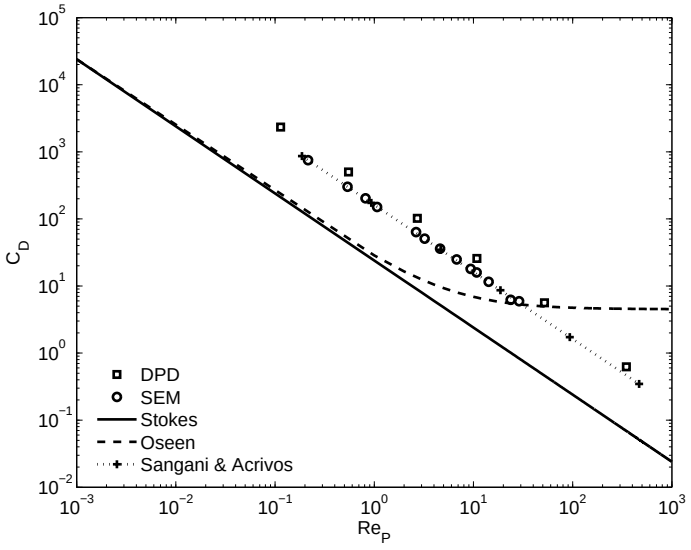

Figure 9.9: Drag coefficient C_D as a function of particle Reynolds number Re_P for the flow past solid sphere in a periodic domain. The periodic images of the sphere form a simple cubic lattice in three dimensional space. The sphere radius is $A = 8$, the solid volume fraction is $\varphi = 0.2$. The sphere is modeled by freezing the portion of the initial DPD particle lattice (model "A").

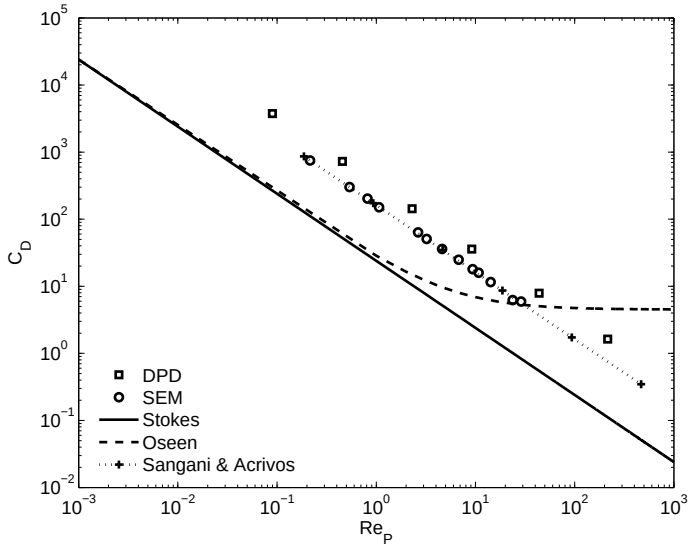

Figure 9.10: Drag coefficient C_D as a function of particle Reynolds number Re_P for the flow past solid sphere in a periodic domain. The periodic images of the sphere form a simple cubic lattice in three dimensional space. The sphere radius is $A = 8$, the solid volume fraction is $\varphi = 0.2$. The sphere is modeled by freezing the portion of the initial DPD particle lattice in combination with bounce back reflection at the solid-fluid interface (model "B").

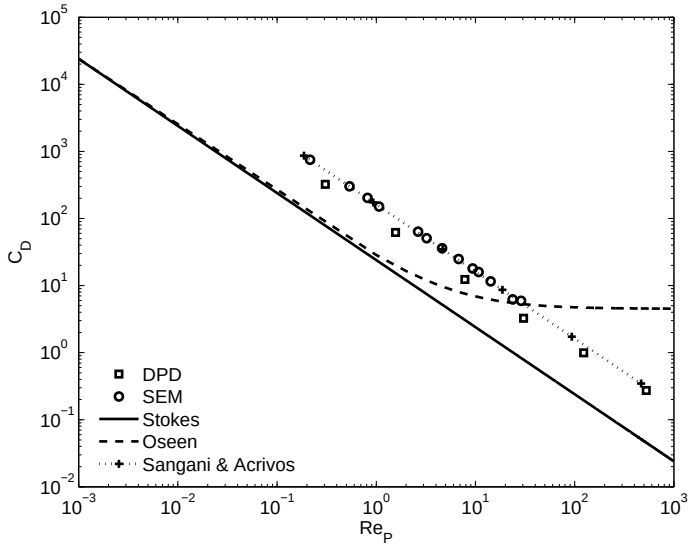

Figure 9.11: Drag coefficient C_D as a function of particle Reynolds number Re_P for the flow past solid sphere in a periodic domain. The periodic images of the sphere form a simple cubic lattice in three dimensional space. The sphere radius is $A = 8$, the solid volume fraction is $\varphi = 0.2$. The sphere is modeled using layers of DPD particles, in combination with bounce back reflection at the sphere surface. The conservative force coefficient of the DPD particles inside the sphere is adjusted using equation (5.3) (model "C").

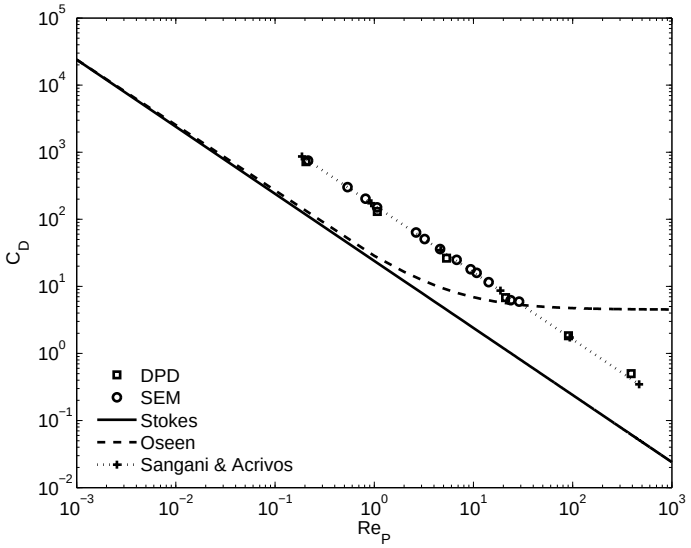

Figure 9.12: Drag coefficient C_D as a function of particle Reynolds number Re_P for the flow past solid sphere in a periodic domain. The periodic images of the sphere form a simple cubic lattice in three dimensional space. The sphere radius is $A = 8$, the solid volume fraction is $\varphi = 0.2$. The sphere is modeled using layers of DPD particles with the density matching the fluid density, in combination with bounce back reflection at the sphere surface. The conservative force coefficient of the DPD particles inside the sphere is adjusted using equation (5.3).

is used in simulations. The temperature is set to $k_BT = 1$ ($\sigma_R = 3$, $\gamma = 4.5$). The conservative force coefficient is equal to $a = 25$. A spherical particle of radius $A = 6$ initially is placed inside the domain with its center at (x_0, y_0, z_0)=$(20.8, 24.26, 88.05)$. The sphere is constructed by freezing the layers of DPD particles in combination with bounce-back reflection at the solid-fluid interface. The density of the sphere is equal to the fluid density. The conservative force coefficient of the DPD particles inside the sphere is set to 3.2447 (equation (5.3)). The sphere is released without initial velocity or rotation and is settling under the force $F_{ext} = 1.033912$ in z direction.

Eight simulations are performed. In each simulation initial velocities of fluid particles are randomly chosen from the Maxwell equilibrium distribution. The settling velocity of the sphere, V_s, is found as an ensemble average. In figure 9.13 we plot V_s as a function of time. The symbols are the mean value of velocity at different time moments while the bars are standard deviation. The settling velocity is normalized by the terminal velocity V_T. The time is normalized by the characteristic time τ_{95},

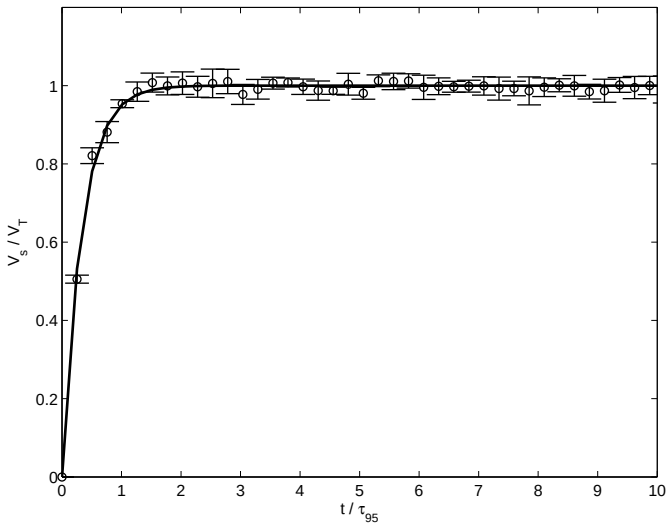

Figure 9.13: Sphere velocity versus time. The sphere velocity V_s is normalized by the terminal velocity V_T. τ_{95} is the time it takes for the sphere to reach 95% of the terminal velocity. The symbols represent the mean values of velocity averaged over 8 DPD simulations; the standard deviations are shown with bars. The solid line is an empirical curve obtained from the experimental measurements by Mordant and Pinton [47].

which is defined as the time it takes the particle to reach 95% of the terminal velocity. The simulation results are compared with the empirical curve obtained from the experimental measurements by Mordant and Pinton [47]. The results are in a good agreement.

9.5 Flow past a sphere near one wall of a 3D channel

In this section we consider the flow past a sphere placed near one wall of a three dimensional channel. For comparison we employ spectral/hp element discretization [35] to obtain an accurate numerical solutions.

The fluid domain occupies the region $0 \leq x \leq 52.002$, $0 \leq y \leq 24.2676$ and $0 \leq z \leq 24.2676$. The domain is periodic in x and z directions, while the no slip boundary conditions are modeled on the y boundaries of the domain using the particle based boundary condition described in chapter 5. The DPD fluid density is $\rho_f = 3$.

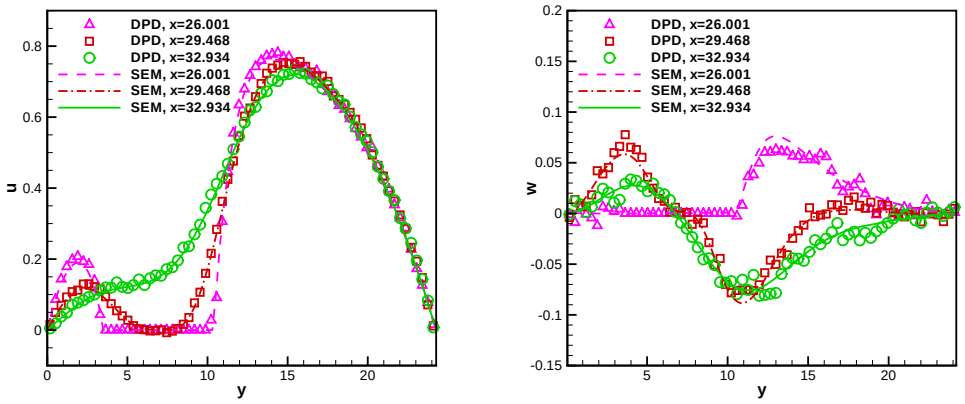

Figure 9.14: Flow past a sphere near one wall of a 3D channel. The DPD streamwise and normal fluid velocity profiles (symbols) are compared to spectral element method (SEM) results (lines).

The random and dissipative force coefficients are set to 3 and 4.5, respectively. The conservative force coefficient is equal to 25. The positions of the particles are updated using the modified velocity Verlet algorithm [24] with $\lambda = 0.5$ and time step 0.02. The DPD fluid kinematic viscosity was found to be $\nu = 0.284$. The spherical particle of radius $A = 3.4668$ is placed with its center at $x = 26.001$, $y = 12.1338$ and $z = 6.9336$. The sphere is modeled by freezing the layers of DPD particles with conservative force adjusted according to equation (5.3) in combination with bounce back reflection at the surface of the sphere. The flow is sustained by the external force $F_{ext} = 0.00125277$ in x direction. The simulations were run for 1.6 million time steps. The domain was divided into bins of size $h = 0.5$ over which the velocity was averaged for 1.2 million time steps. The fluid velocity profiles were extracted along three lines inside the computational domain. The lines are located in $y = 12.1338$ plane and are parallel to z axis. The x coordinates of the lines are $x = 26.001$, $x = 29.468$ and $x = 32.934$.

In spectral element simulations the 3D channel has dimensions 15, 7 and 7 in x, y and z directions, respectively. The channel is periodic in x and z directions. The no-slip boundary conditions are specified in y direction. The sphere of radius $A = 1$ is placed with its center within distance 2 from the $y = 0$ boundary. The simulation

domain is discretized into the 4608 spectral hexahedra elements. The third order polynomial expansion is used in each element. The kinematic viscosity of the fluid is set to $\nu = 1$. The flow is driven by constant force in x direction, $F_{ext} = 1.94152185$. The simulations were run until steady state was reached.

In figure 9.14 we compare extracted streamwise and normal velocity profiles obtained by DPD and SEM. The SEM simulation results were scaled appropriately to be in DPD units. The agreement is good with some scattering apparent in the normal velocity profiles in DPD. We note here that the DPD results can be improved by averaging over larger number of time steps.

9.6 Migration of a Spherical Particle in Shear

In this section we consider migration of neutrally buoyant spherical particle in shear. Several experimental, theoretical and numerical studies of this phenomenon can be found in literature [43, 58, 61, 62, 63]. Here, we compare the DPD simulation results with the computational results obtained by Lomholt [39] using the Force Coupling Method [40, 44].

The computational domain is a box, periodic in x and y directions. The particle based boundary conditions (chapter 5) are used on the boundaries in z direction. The fluid domain covers the region $0 \leq x \leq 48.535289$, $0 \leq y \leq 27.734450$, $0 \leq z \leq 49.922011$. The DPD fluid density is $\rho_f = 3$. The temperature is set to $k_BT = 1$ by choosing $\sigma_R = 3$ and $\gamma = 4.5$. The conservative force coefficient of the fluid particles is equal to $a = 25$. The modified velocity Verlet scheme is used for time integration [24]. Parameter λ is equal to 0.5, while the time step is 0.02. The flow is driven by the force $F_{ext} = 0.00041296$ applied in x direction. The Reynolds number based on the half width of the channel, $L = 24.9610055$, fluid kinematic viscosity, $\nu = 0.284$, and fluid velocity in the center plane ($z = 24.9610055$), $u_{max} = 0.4544$, is equal to $Re = \frac{Lu_{max}}{\nu} = 40$. The sphere is created by freezing the DPD particles. Initially it is located close to the center of the channel. The trajectory of the sphere was recorded during the simulations for about 2,000,000 time steps. In figure 9.15 we plot

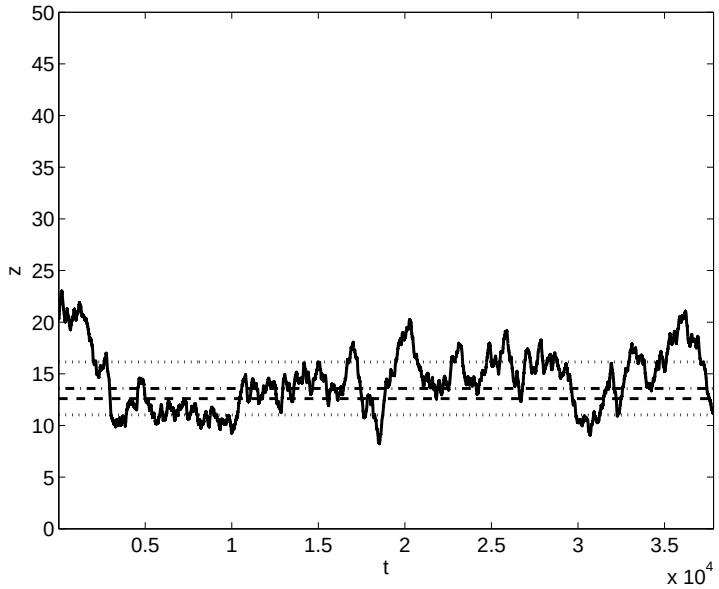

Figure 9.15: Migration of neutrally buoyant spherical particle in poiseuille flow. The trajectory of the z coordinate of the sphere center as a function of time is shown with a solid line. The time-averaged mean position of the sphere is shown with a dash-dotted line. The dotted lines are one standard deviation away from the mean position. The dashed line, represents the final position of the sphere obtained in [39] using Force Coupling Method simulations.

z coordinate of the sphere center as a function of time. The sphere wanders around its equilibrium position which is located approximately in the middle of the channel midplane and the wall. The time-averaged mean position of the sphere ($z = 13.5815$) is shown in figure with a dash-dotted line. The dotted lines are one standard deviation (2.5614) away from the mean position. The dashed line, represents the final position of the sphere ($z = 0.504L$) obtained by Lomholt [39].

9.7 Viscosity of a Dilute Suspension of Spherical Particles

In this section we calculate viscosity of a dilute suspension of spherical particles. We use a method introduced by Gosling *et al* [22] in 1973. In this method a domain of

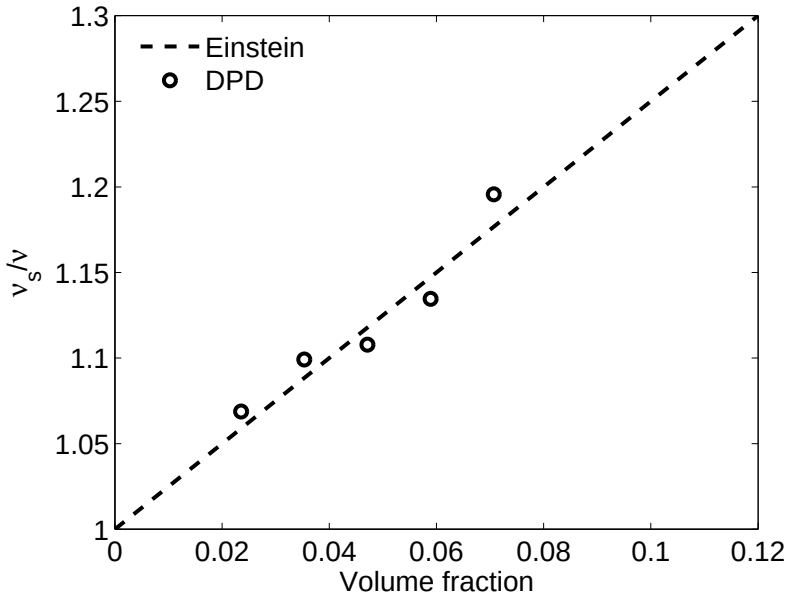

Figure 9.16: Viscosity of the dilute suspension of solid spheres, ν_s, normalized by the DPD fluid viscosity, ν, as a function of volume fraction φ.

size (L_x, L_y, L_z) is periodic in all direction. The force F_x,

$$F_x = \alpha_x m \sin(\frac{2\pi z}{L_z}) \tag{9.9}$$

is applied in the x direction to develop a steady flow profile. The flow profile is expected to be of the form

$$u_x = \frac{\alpha_x L^2}{4\pi^2 \nu} \sin(\frac{2\pi z}{L_z}). \tag{9.10}$$

The kinematic viscosity of the fluid can be found by fitting the calculated velocity profile using equation (9.10). The necessary conditions for the method to produce reliable results can be found in a recent paper [73].

We apply the Gosling method to a dilute suspension of spherical particles. The simulation domain dimensions are $L_x = 22.012848$, $L_y = 22.012848$ and $L_z = 132.077090$. The radius of spherical particles is chosen to be $A = 3.301817$. The number of spheres varies in the simulations from 10 to 30 to obtain different volume fractions. The spheres are modeled by freezing the regions of the initial fcc lattice. The positions of the spheres inside the domain are chosen randomly at the beginning

of the simulations. The DPD fluid density is equal to $\rho_f = 3$. The modified velocity Verlet scheme ($\lambda = 0.5$) is used [24]. The time step is equal to 0.02. The DPD force coefficients a, σ_R and γ are set to 25, 3 and 4.5, respectively. The DPD fluid viscosity was found to be $\nu = 0.284$. In figure 9.16 the calculated suspension viscosity ν_s for different solid volume fractions φ is compared to the Einstein prediction for a dilute suspensions,

$$\frac{\nu_s}{\nu} = 1 + \frac{5}{2}\varphi + O(\varphi^2). \tag{9.11}$$

The agreement is good.

9.8 Summary

In this chapter we have simulated the flows around solid spherical particles using DPD. Several problems were considered. The simulation results were compared with analytic predictions, experimental observations and other simulation results.

Chapter 10

Simulation of Platelet Aggregation using DPD

10.1 Introduction

The kinematic viscosity of the DPD fluid with typical simulation parameters is relatively low (about 1 in DPD units) and therefore simulations of platelet aggregation in flows with realistic Reynolds numbers require very long computational times. The purpose of this chapter is not to use the DPD as an instrument for simulation of platelet aggregation, but rather to test its ability to reproduce characteristic features of the process, previously obtained by means of FCM computations in chapter 3.

We consider the flows with Reynolds numbers higher than observed in vivo. Specifically, the particle Reynolds numbers based on the platelet diameter and mean flow velocity in the vessel, are of order 1. We note here, that the viscosity of the DPD fluid can be increased for example by using the Lowe thermostat [41] with large values of parameter Γ. Based on the values of the dynamic viscosity computed in chapter 7 the Reynolds number can be decreased by one or two orders of magnitude this way. Lowe method is a global thermostat and to the best of our knowledge no implementation suitable for large scale parallel computations exists. This limits the application of the Lowe thermostat for relatively small systems. It may also be possible to use different weight function w in a standard DPD formulation, see equation (4.5), to

affect the viscosity of the DPD fluid. It was shown in [11] that for specific choice of the weight function the realistic Schmidt numbers can be achieved in simulations; the dependence of fluid viscosity on w needs to be studied in the future.

10.2 Numerical Simulations and Results

The flow domain is a cylinder with radius $A_c = 20.8$ in DPD units. The axis of the cylinder is parallel to z coordinate axis and is passing through the origin of the coordinate system. The cylinder extends from $z = 0$ to $z = 104$. The system is periodic in z direction; the DPD particles leaving the computational domain at $z = 104$ are introduced back into the system at $z = 0$. The DPD fluid density is set to $\rho_f = 3$. The conservative force coefficient a is set to 25. The values of random and dissipative force coefficients are $\sigma_R = 3$ and $\gamma = 4.5$, respectively. The modified velocity Verlet scheme with parameter $\lambda = 0.5$ [24] and time step 0.02 is used to advance the system in time. The kinematic viscosity of the DPD fluid was found to be $\nu = 0.284$.

The no-slip conditions at the walls of the cylinder are modeled using the particle boundary conditions developed in chapter 5. The parabolic inflow velocity profile is generated by placing the inflow region inside the channel. The z component of the velocity of DPD particles inside the inflow region is set to the value equal to the fluid velocity at the location of the particle given by the Poiseuille flow solution. The inflow region covers part of the flow domain between $z = 97$ and $z = 98.5$. Due to the periodicity of the system in z direction parabolic velocity profile develops upstream of the platelet aggregate.

The aggregate is initiated by placing a small number of activated seed platelets attached to the wall. In simulations described below six seed platelets were placed close to the wall approximately at $z = 28$. The platelets are modeled as a rigid spheres of radius $A = 2.08$ by grouping the DPD particles. The particles are arranged in layers as described in section 9.2 to minimize the roughness of the surface. The density of the DPD particles inside each platelet is equal to the fluid density $\rho_f = 3$, while

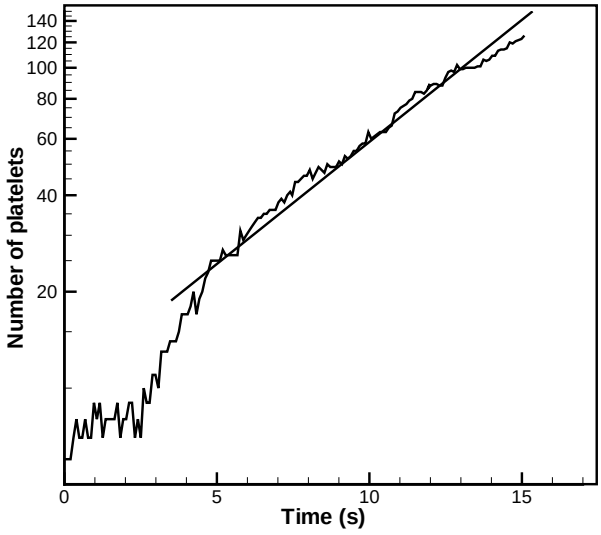

Figure 10.1: Accumulation of platelets in a thrombus with flow rate of $167\mu m/s$. Solid lines used to correlate exponential growth phase; slopes plotted on figure 10.2.

the conservative force coefficient a is set to 25. Except for the seed platelets the flow domain is initially free of platelets. We assume that platelets are distributed uniformly in flow upstream of the growing aggregate. During the computations platelets are introduced into the flow upstream of the aggregate in $z = 2.8$ plane. The probability of adding a new platelet at some specific location is proportional to the velocity at this location, which is assumed to have a parabolic profile. When the location is selected all fluid particles which fall inside the volume occupied by a platelet are replaced by the DPD particles forming the sphere. The freshly added platelet is allowed to follow the flow and interact with the walls and other platelets. Platelets reaching $z = 95$ plane are eliminated from the simulations. This is done by removing the constraints on the motion of the DPD particles inside the platelets.

The platelets interact with each other and the vessel walls following the rules described in chapter 3. Activated platelets are allowed to adhere anywhere they come sufficiently close to the wall. The values of R_R, R_L, R_M and R_B were set to 1, 1.5, 2.5 and 3.5, respectively. The extent of the activation-distance corona was defined by $R_A = 1.5$. Constants α_1, α_2, α_3 and α_4 defining the strength of the interaction

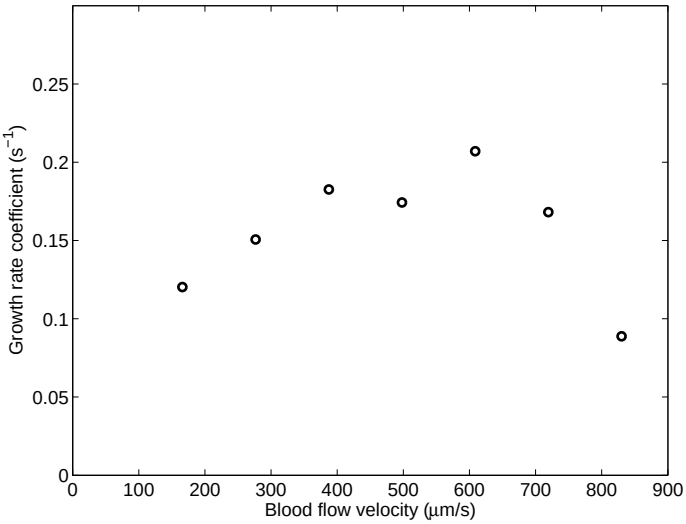

Figure 10.2: Exponential thrombus growth rate coefficients as a function of flow rate in small vessel $30\mu m$ diameter. The trend of the growth rate coefficients as a function of flow rate matching qualitatively the trend from FCM simulations in chapter 3.

forces between platelets and walls are equal to 2000, 2000, 1000 and 1000 in DPD units, respectively. The range of activation delay time was specified by $t_{a1} = 25$ and $t_{a2} = 100$. Six simulations are performed with the mean flow velocities in the channel between 0.15 and 0.75. To reduce the computational time the concentration of platelets in blood was chosen to be about 1000000 per cubic millimeter.

For a platelet following the blood stream in the vessel we can define time t_d, the time it takes the platelet to travel the distance equal to its diameter based on the mean flow velocity. The ratio of the mean activation delay time and t_d is a non-dimensional number. For an activation delay time of $0.1s$, platelet of radius $3\mu m$ in the vessel with mean blood flow velocity, this ratio is about 1.667. By assuming that in DPD simulations the platelet radius corresponds to $1.5\mu m$ and the mean activation delay time is $0.1s$, we define the unit of time and length. In these units the diameter of the vessel is equal to $30\mu m$ and simulated mean blood flow velocities are in the range between $167\mu m/s$ and $833\mu m/s$. The following results are expressed in these units.

The simulation results qualitatively match aspects of the formation of the platelet mural aggregates obtained in chapter 3. In figure 10.1 we show the number of adhered

to the aggregate platelets as a function of time for one of the simulation cases. In common with FCM studies, there is an exponential growth rate of aggregate volume with time. Thrombi initiated at other flow rates also have their major phase of growth exponential in time. The effect of blood flow rate on the exponential coefficient broadly matches the rise and fall with blood flow velocity (see figure 10.2).

10.3 Summary

In this chapter we simulated platelet aggregation using the DPD method. Although the Reynolds numbers were unrealistically high in computations, the simulation results reproduce the main features of platelet aggregation, such as exponential growth rate of aggregate volume and variation of growth rate coefficient with the blood flow velocity.

Chapter 11

Concluding Remarks

11.1 Summary

In this thesis we have achieved the following goals:

- We demonstrated that the concept of platelet activation delay time can be integrated into a computer model of mural thrombus formation, which incorporates a small number of physical parameters and functions to represent physicochemical factors such as cell adhesion molecule behaviour, fibrinogen, and so forth for the scale represented in the model.
- We presented the results of first simulation of thrombus formation in 3-D flows by accounting for the movements of all platelets individually involved.
- We proposed a process of choosing the DPD parameters and determining the DPD length and time scales for different levels of coarse-graining. Through this we established the link between the atomistic molecular dynamics and mesoscale DPD approach.
- We identified three factors that limit the application of the DPD method at high coarse-graining levels: inter-particle force magnitude, compressibility, and geometric confinement.

- We examined the ramifications of different implementations of no-slip boundary conditions in DPD and subsequently proposed a method, based on an equivalent force between wall- and DPD-particles, to impose boundary conditions.

- We developed an adaptive model for wall-particle interactions that allows to target the desired density profile close to the wall, while at the same time keeping the no-slip boundary condition in DPD.

11.2 Future Directions

In concluding this thesis, we will now suggest some areas of future research which follow from some of the work presented herein.

We believe that future emphasis in simulations of platelet aggregation will need to be focussed on the development of more sophisticated models, incorporating finer details of the process.

Platelets normally account for only about 1% of blood volume, with about 40% of it occupied by red blood cells (RBC). Therefore, platelets are in a "crowded" environment of red blood cells and there are frequent collisions between them. Thus, platelets motion, especially their microscopic motion and fluctuations around their mean trajectory, are primarily determined by the presence of RBCs. The presence of RBCs should be taken into account explicitly, even though this would result in very considerable complexity.

Some other issues to be addressed are the following:

- Incorporation of realistic platelet interaction forces obtained from experiments.

- Numerical simulation of diffusion of chemicals such as ADP, arachidonic acid and thromboxane A_2.

- Simulation of phospholipid bilayer membrane with embedded glycoproteins (GP) - the receptors for activation and interaction with other cells.

- Modeling of plasma adhesive proteins such as fibrinogen, vWf and fibronectin.

- Deformation of cells as it may play a key role in determining their aggregability [4].

Algorithms developed in this thesis can be applied in various applications. These applications include, but not limited to:

- Optimal design of artificial internal organs, such as prosthetic heart valves to minimize platelet aggregation.
- Simulation of blood flows in vessels with stents, optimization of stent geometry.
- Modeling and development of various aggregometers and hemostatometers.
- Assessing the impact of various platelet-active drugs in altering thrombus formation.
- Simulation of platelet aggregation in various physiological flow conditions such as in stenosed vessels or over atherosclerotic plaque caps.

Bibliography

[1] J. Acar, B. Iung, J. P. Boissel, M. M. Samama, P. L. Michel, J. P. Teppe, J. C. Pony, H. LeBreton, D. Thomas, R. Isnard, G. deGevigney, E. Viguier, A. Sfihi, G. Hanania, M. Ghannem, A. Mirode, C. Nemoz, N. Bossard, C. Rolland, L. Lion, C. Marsault, J. P. Ferroir, J. Conard, J. P. Laborde, Y. Logeais, J. P. Delahaye, F. Guerin, R. Lainee, and J. P. Lesbre. AREVA: Multicenter randomized comparison of low-dose versus standard-dose anticoagulation in patients with mechanical prosthetic heart valves. *Circulation*, 94(9):2107–2112, 1996.

[2] M. P. Allen and D. J. Tildesley. *Computer simulation of liquids*. Clarendon Press, Oxford, 1987.

[3] J. A. Backer, C. P. Lowe, H. C. J. Hoefsloot, and P. D. Iedema. Poiseuille flow to measure the viscosity of particle model fluids. *Journal of Chemical Physics*, 122(15):154503, 2005.

[4] P. Bagchi, P. C. Johnson, and A. S. Popel. Computational fluid dynamic simulation of aggregation of deformable cells in a shear flow. *Journal of Biomechanical Engineering-Transactions of the ASME*, 127(7):1070–1080, 2005.

[5] N. Begent and G. V. Born. Growth rate in vivo of platelet thrombi, produced by iontophoresis of ADP, as a function of mean blood flow velocity. *Nature*, 227(5261):926–30, 1970.

[6] K. Bodziak and P. D. Richardson. Turnover of adherent platelets - some effects of shear rate, ASA, and reduced anticoagulation. *Transactions American Society for Artificial Internal Organs*, 28:426–430, 1982.

[7] E. S. Boek, P. V. Coveney, and H. N. W. Lekkerkerker. Computer simulation of rheological phenomena in dense colloidal suspensions with dissipative particle dynamics. *Journal of Physics-Condensed Matter*, 8(47):9509–9512, 1996.

[8] E. S. Boek, P. V. Coveney, H. N. W. Lekkerkerker, and P. van der Schoot. Simulating the rheology of dense colloidal suspensions using dissipative particle dynamics. *Physical Review E*, 55(3):3124–3133, 1997.

[9] G. V. R. Born and P. D. Richardson. Activation time of blood-platelets. *Journal of Membrane Biology*, 57(2):87–90, 1980.

[10] S. J. Chang, J. S. Lin, and H. H. Chen. Alpha-tocopherol downregulates the expression of GPIIb promoter in HEL cells. *Free Radic Biol Med*, 28(2):202–207, 2000.

[11] S. Chen, N. Phan-Thien, B. C. Khoo, and X. J. Fan. Flow around spheres by dissipative particle dynamics. *Unpublished*.

[12] M. Cieplak, J. Koplik, and J. R. Banavar. Boundary conditions at a fluid-solid interface. *Physical Review Letters*, 86(5):803–806, 2001.

[13] S. L. Dance. *Particle Sedimentation in Viscous Fluids*. PhD thesis, Brown University, 2002.

[14] G. L. Dent. *Aspects of Particle Sedimentation in Dilute Flows at Finite Reynolds Numbers*. PhD thesis, Brown University, 1999.

[15] P. Espanol and P. Warren. Statistical-mechanics of dissipative particle dynamics. *Europhysics Letters*, 30(4):191–196, 1995.

[16] E. Evans. Probing the relation between force - lifetime - and chemistry in single molecular bonds. *Annual Review of Biophysics and Biomolecular Structure*, 30:105–128, 2001.

[17] S. Falati, P. Gross, G. Merrill-Skoloff, B. C. Furie, and B. Furie. Real-time in vivo imaging of platelets, tissue factor and fibrin during arterial thrombus formation in the mouse. *Nat Med*, 8(10):1175–81, 2002.

[18] S. Falati, Q. Liu, P. Gross, G. Merrill-Skoloff, J. Chou, E. Vandendries, A. Celi, K. Croce, B. C. Furie, and B. Furie. Accumulation of tissue factor into developing thrombi in vivo is dependent upon microparticle p-selectin glycoprotein ligand 1 and platelet p-selectin. *J Exp Med*, 197(11):1585–98, 2003.

[19] X. J. Fan, N. Phan-Thien, N. T. Yong, X. H. Wu, and D. Xu. Microchannel flow of a macromolecular suspension. *Physics of Fluids*, 15(1):11–21, 2003.

[20] B. M. Forrest and U. W. Suter. Accelerated equilibration of polymer melts by time-coarse-graining. *Journal of Chemical Physics*, 102(18):7256–7266, 1995.

[21] D. Frenkel and B. Smit. *Understanding molecular simulation : From algorithms to applications*. Academic Press, San Diego, 1996.

[22] E. M. Gosling, I. R. McDonald, and K. Singer. On the calculaton by molecular dynamics of the shear viscosity of a simple fluid. *Mol. Phys.*, 26:1475, 1973.

[23] R. D. Groot and K. L. Rabone. Mesoscopic simulation of cell membrane damage, morphology change and rupture by nonionic surfactants. *Biophysical Journal*, 81(2):725–736, 2001.

[24] R. D. Groot and P. B. Warren. Dissipative particle dynamics: Bridging the gap between atomistic and mesoscopic simulation. *Journal of Chemical Physics*, 107(11):4423–4435, 1997.

[25] R. D. Guy and A. L. Fogelson. Probabilistic modeling of platelet aggregation: Effects of activation time and receptor occupancy. *Journal of Theoretical Biology*, 219(1):33–53, 2002.

[26] A. C. Guyton. *Textbook of Medical Physiology*. W. B. Saunders Company, Philadelphia, seventh edition, 1986.

[27] J. M. Haile. *Molecular dynamics simulation : Elementary methods*. Wiley, New York, 1992.

[28] L. A. Harker, U. M. Marzec, A. B. Kelly, N. R. F. Chronos, I. B. Sundell, S. R. Hanson, and J. M. Herbert. Clopidogrel inhibition of stent, graft, and vascular thrombogenesis with antithrombotic enhancement by Aspirin in nonhuman primates. *Circulation*, 98(22):2461–2469, 1998.

[29] H. Hasimoto. On the periodic fundamental solutions of the stokes equations and their application to viscous flow past a cubic array of spheres. *Journal of Fluid Mechanics*, 5:317–328, 1959.

[30] J. Hirsh, R. Raschke, T. E. Warkentin, J. E. Dalen, D. Deykin, and L. Poller. Heparin - mechanism of action, pharmacokinetics, dosing considerations, monitoring, efficacy, and safety. *Chest*, 108(4):S258–S275, 1995.

[31] P. J. Hoogerbrugge and J. M. V. A. Koelman. Simulating microscopic hydrodynamic phenomena with dissipative particle dynamics. *Europhysics Letters*, 19(3):155–160, 1992.

[32] S. Izvekov and G. A. Voth. Multiscale coarse graining of liquid-state systems. *Journal of Chemical Physics*, 123(13):134105, 2005.

[33] S. P. Jackson, W. S. Nesbitt, and S. Kulkarni. Signaling events underlying thrombus formation. *J Thromb Haemost*, 1(7):1602–1612, 2003.

[34] A. F. Jakobsen, O. G. Mouritsen, and G. Besold. Artifacts in dynamical simulations of coarse-grained model lipid bilayers. *Journal of Chemical Physics*, 122(20):204901, 2005.

[35] G. E. Karniadakis and S. J. Sherwin. *Spectral/hp element methods for CFD*. Oxford University Press, Oxford, second edition, 2005.

[36] M. A. Katsoulakis, A. J. Majda, and D. G. Vlachos. Coarse-grained stochastic processes for microscopic lattice systems. *Proceedings of the National Academy of Sciences of the United States of America*, 100(3):782–787, 2003.

[37] J. M. Kim and R. J. Phillips. Dissipative particle dynamics simulation of flow around spheres and cylinders at finite reynolds numbers. *Chemical Engineering Science*, 59(20):4155–4168, 2004.

[38] A. W. Lees and S. F. Edwards. The computer study of transport process under extreme conditions. *J Phys C*, 5:1921, 1972.

[39] S. Lomholt. *Numerical investigations of macroscopic particle dynamics in microflows*. PhD thesis, Risoe National Laboratory, 2001.

[40] S. Lomholt and M. R. Maxey. Force-coupling method for particulate two-phase flow: Stokes flow. *Journal of Computational Physics*, 184(2):381–405, 2003.

[41] C. P. Lowe. An alternative approach to dissipative particle dynamics. *Europhysics Letters*, 47(2):145–151, 1999.

[42] N. S. Martys. Study of a dissipative particle dynamics based approach for modeling suspensions. *Journal of Rheology*, 49(2):401–424, 2005.

[43] J. P. Matas, J. F. Morris, and E. Guazzelli. Inertial migration of rigid spherical particles in poiseuille flow. *Journal of Fluid Mechanics*, 515:171–195, 2004.

[44] M. R. Maxey and B. K. Patel. Localized force representations for particles sedimenting in stokes flow. *International Journal of Multiphase Flow*, 27(9):1603–1626, 2001.

[45] K. Meier, A. Laesecke, and S. Kabelac. Transport coefficients of the lennard-jones model fluid. I. Viscosity. *Journal of Chemical Physics*, 121(8):3671–3687, 2004.

[46] F. N. Miller, D. E. Sims, D. A. Schuschke, and D. L. Abney. Differentiation of light-dye effects in the microcirculation. *Microvasc Res*, 44(2):166–84, 1992.

[47] N. Mordant and J. F. Pinton. Velocity measurement of a settling sphere. *European Physical Journal B*, 18(2):343–352, 2000.

[48] H. Ni, P. S. Yuen, J. M. Papalia, J. E. Trevithick, T. Sakai, R. Fassler, R. O. Hynes, and D. D. Wagner. Plasma fibronectin promotes thrombus growth and stability in injured arterioles. *Proc Natl Acad Sci U S A*, 100(5):2415–9, 2003.

[49] M. G. Noro, P. K. C. Paul, and P. B. Warren. Linking atomistic and mesoscale simulations of water-soluble polymers. *Journal of the American Chemical Society*, 125(24):7190–7191, 2003.

[50] M. G. Oude Egbrink, M. A. Van Gestel, M. A. Broeders, G. J. Tangelder, J. M. Heemskerk, R. S. Reneman, and D. W. Slaaf. Regulation of microvascular thromboembolism in vivo. *Microcirculation*, 12(3):287–300, 2005.

[51] R. L. Panton. *Incompressible Flow*. John Wiley & Sons, Inc., New York, 1996.

[52] N. N. Petrishchev and I. A. Mikhailova. Influence of some hydrodynamic factors of thrombus formation in microvessels. *Microvasc Res*, 49(1):12–6, 1995.

[53] R. Polanowska-Grabowska and A. R. Gear. High-speed platelet adhesion under conditions of rapid flow. *Proc Natl Acad Sci U S A*, 89(13):5754–8, 1992.

[54] J. C. Poole, A. G. Sanders, and H. W. Florey. The regeneration of aortic endothelium. *J Pathol Bacteriol*, 75(1):133–143, 1958.

[55] M. Revenga, I. Zuniga, and P. Espanol. Boundary conditions in dissipative particle dynamics. *Computer Physics Communications*, 122:309–311, 1999.

[56] M. Revenga, I. Zuniga, P. Espanol, and I. Pagonabarraga. Boundary models in DPD. *International Journal of Modern Physics C*, 9(8):1319–1328, 1998.

[57] P. D. Richardson. Effect of blood flow velocity on growth rate of platelet thrombi. *Nature*, 245(5420):103–104, 1973.

[58] P. G. Saffman. The lift on a small sphere in a slow shear flow. *Journal of Fluid Mechanics*, 22:385–400, 1965.

[59] J. H. Sanderson and C. E. Phillips. *An Atlas of Laboratory Animal Haematology*. Oxford University Press, New York, 1981.

[60] A. S. Sangani and A. Acrivos. Slow flow through a periodic array of spheres. *International Journal of Multiphase Flow*, 8(4):343–360, 1982.

[61] J. A. Schonberg and E. J. Hinch. Inertial migration of a sphere in poiseuille flow. *Journal of Fluid Mechanics*, 203:517–524, 1989.

[62] G. Segre and A. Silberberg. Behaviour of macroscopic rigid spheres in poiseuille flow. Part 1. Determination of local concentration by statistical analysis of particle passages through crossed light beams. *Journal of Fluid Mechanics*, 14:115–135, 1962.

[63] G. Segre and A. Silberberg. Behaviour of macroscopic rigid spheres in poiseuille flow. Part 2. Experimental results and interpretation. *Journal of Fluid Mechanics*, 14:135–157, 1962.

[64] J. R. Sheu, T. H. Fong, C. M. Liu, M. Y. Shen, T. L. Chen, Y. Chang, M. S. Lu, and G. Hsiao. Expression of matrix metalloproteinase-9 in human platelets: regulation of platelet activation in in vitro and in vivo studies. *British Journal of Pharmacology*, 143(1):193–201, 2004.

[65] M. Z. Smoluchowski. *Phys Chem*, 92:129–168, 1917.

[66] S. Sukavaneshvar, Y. Zheng, G. M. Rosa, S. F. Mohammad, and K. A. Solen. Thromboembolization associated with sudden increases in flow in a coronary stent ex vivo shunt model. *ASAIO J*, 46(3):301–4, 2000.

[67] C. Theodoropoulos, Y. H. Qian, and I. G. Kevrekidis. "Coarse" stability and bifurcation analysis using time-steppers: A reaction-diffusion example. *Proceedings of the National Academy of Sciences of the United States of America*, 97(18):9840–9843, 2000.

[68] A. Thill, S. Veerapaneni, B. Simon, M. Wiesner, J. Y. Bottero, and D. Snidaro. Determination of structure of aggregates by confocal scanning laser microscopy. *Journal of Colloid and Interface Science*, 204(2):357–362, 1998.

[69] P. A. Thompson and M. O. Robbins. Shear-flow near solids - epitaxial order and flow boundary-conditions. *Physical Review A*, 41(12):6830–6837, 1990.

[70] P. A. Thompson and S. M. Troian. A general boundary condition for liquid flow at solid surfaces. *Nature*, 389(6649):360–362, 1997.

[71] S. Y. Trofimov. *Thermodynamic consistency in dissipative particle dynamics*. PhD thesis, Eindhoven University of Technology, 2003.

[72] M. A. van Gestel, J. W. Heemskerk, D. W. Slaaf, V. V. Heijnen, S. O. Sage, R. S. Reneman, and M. G. Oude Egbrink. Real-time detection of activation patterns in individual platelets during thromboembolism in vivo: Differences between thrombus growth and embolus formation. *J Vasc Res*, 39(6):534–43, 2002.

[73] V. R. Vasquez, E. A. Macedo, and M. S. Zabaloy. Lennard-Jones viscosities in wide ranges of temperature and density: Fast calculations using a steady-state periodic perturbation method. *International Journal of Thermophysics*, 25(6):1799–1818, 2004.

[74] A. J. Wagner and I. Pagonabarraga. Lees-Edwards boundary conditions for lattice Boltzmann. *Journal of Statistical Physics*, 107(1-2):521–537, 2002.

[75] M. Whittle and E. Dickinson. On simulating colloids by dissipative particle dynamics: Issues and complications. *Journal of Colloid and Interface Science*, 242(1):106–109, 2001.

[76] S. M. Willemsen, H. C. J. Hoefsloot, and P. D. Iedema. No-slip boundary condition in dissipative particle dynamics. *International Journal of Modern Physics C*, 11(5):881–890, 2000.

[77] www.pointwise.com.

[78] M. B. Zucker. Platelet aggregation measured by the photometric method. *Methods Enzymol*, 169:117–133, 1989.